NASA Technical Memorandum

NASA TM-82570

THE AXAF TECHNOLOGY PROGRAM: THE OPTICAL FLATS TESTS

A. C. Williams, J. D. Harper, J. C. Reily,
M. C. Weisskopf, C. L. Wyman, and M. Zombeck

January 1984

National Aeronautics and
Space Administration

George C. Marshall Space Flight Center

MSFC - Form 3190 (Rev May 1983)

TECHNICAL REPORT STANDARD TITLE PAGE

1 REPORT NO.	2. GOVERNMENT ACCESSION NO.	3. RECIPIENT'S CATALOG NO.
NASA TM-82570		

4 TITLE AND SUBTITLE	5 REPORT DATE
The AXAF Technology Program: The Optical Flats Tests	January 1984
	6. PERFORMING ORGANIZATION CODE

7 AUTHOR(S)	8. PERFORMING ORGANIZATION REPORT #
A. C. Williams, J. D. Harper,* J. C. Reily,** M. C. Weisskopf, C. L. Wyman,*** and M. Zombeck+	

9 PERFORMING ORGANIZATION NAME AND ADDRESS	10. WORK UNIT NO.
George C. Marshall Space Flight Center Marshall Space Flight Center, Alabama 35812	11. CONTRACT OR GRANT NO.
	13. TYPE OF REPORT & PERIOD COVERED
12 SPONSORING AGENCY NAME AND ADDRESS	Technical Memorandum
National Aeronautics and Space Administration Washington, D.C. 20546	14 SPONSORING AGENCY CODE

15. SUPPLEMENTARY NOTES

Prepared by Space Science Laboratory, Science and Engineering.

16. ABSTRACT

The results of a technology program aimed at determining the limits of surface polishing for reflecting X-ray telescopes is presented in this work. This program is part of the major task of developing the Advanced X-Ray Astrophysical Facility (AXAF). By studying the optical properties of state-of-the-art polished flat surfaces, conclusions have been drawn as to the potential capability of AXAF. Surface microtopography of the flats as well as their figure is studied by X-ray, visual, and mechanical techniques. These techniques and their results are described in this volume.

*Information and Electronic Laboratory
**Test Laboratory
***Office of Associate Director for Engineering
+Smithsonian Astrophysical Observatory, Cambridge, MA.

17 KEY WORDS	18. DISTRIBUTION STATEMENT
X-Ray Telescope Surface Microtopography X-Ray Scattering	Unclassified — Unlimited

19 SECURITY CLASSIF. (of this report)	20. SECURITY CLASSIF. (of this page)	21 NO. OF PAGES	22 PRICE
Unclassified	Unclassified	97	NTIS

MSFC - Form 3292 (May 1969)

For sale by National Technical Information Service, Springfield, Virginia 22151

ACKNOWLEDGMENTS

A very large amount of work and time has gone into the mirror flats test phase of the AXAF Technology Program. This work has been shared by many at the Smithsonian Astrophysical Observatory (SAO), Marshall Space Flight Center (MSFC), National Bureau of Standards (NBS), Lawrence Livermore Laboratory (LLL), Naval Weapons Center of China Lake (NWC), ARRADCOM, and Max Planck Institute.

Instrumental in the polarization profilometer technique and measurements described in Subsection 7.3 was Dr. Gary Sommargren (see Ref. 11). The help of Dr. Greg Sanger of LLL for work in the profilometry measurements is also acknowledged.

Talystep measurements were done by Drs. Theodore Vorburger and E. Clayton Teague of NBS and by Dr. Jean Bennett of NWC. Dr. Bennett also did some total integrated scatter measurements on the flats.

Dr. Eugene Church's contribution in terms of theoretical analysis and models aided the program tremendously. The support and program direction by many personnel at SAO is also acknowledged. In particular, we wish to thank Dr. Leon Van Speybroeck for his many contributions.

Drs. Heinrich Braeuninger and J. Truemper are to be acknowledged for providing access to the Max Planck X-Ray Test Facility.

Many associated with MSFC were instrumental in this program. In particular, Charlie Hawkins was primarily responsible for the mirror assembly and alignments. Don Griner set up and directed the interferometer and scatterometer measurements. Aiding him in the actual data taking were Turner Rogers and Pete Marrers. Jimmy Carter was responsible for the profilometer measurements made at MSFC.

Special thanks goes to all the technicians at the X-Ray Test Facility at MSFC who were responsible for the smooth operation during the X-ray data measurements.

TABLE OF CONTENTS

LIST OF ILLUSTRATIONS

LIST OF ILLUSTRATIONS (Continued)

LIST OF ILLUSTRATIONS (Concluded)

LIST OF TABLES

LIST OF TABLES (Concluded)

FOREWORD

The Advanced X-Ray Astrophysics Facility (AXAF) (Ref. 7) will be a major orbiting astronomical observatory designed to study the universe in X-rays. The facility is currently planned for a 1990 launch with the design and construction of flight hardware to begin in 1986. The heart of the observatory will be a 1.2 m outer diameter, six-fold nested set of Wolter 1 grazing incidence X-ray telescopes. These optics will represent the state-of-the-art in surface finish to minimize image degradation due to X-ray scattering and in surface figuring to minimize distortion of the geometrical image.

In order to achieve these goals, a technology program is currently in progress. This program consists of three separate activities all aimed at elucidating the requirements of achieving the AXAF goals. The first part of the program involves the measurement of X-ray scattering from highly polished optical flats. The second part of the program involves characterizing the figure and surface roughness of the optical flats by a variety of visual and mechanical techniques. The final part of the program involves the design and construction of a small Wolter type 1 optics to demonstrate the state-of-the-art in X-ray imaging. The techniques and results of the first two activities are discussed in detail in this volume. The results of the last activity will be presented in an additional volume to this series.

I. INTRODUCTION

The X-ray scattering measurements were performed primarily in the Marshall Space Flight Center's (MSFC) X-Ray Calibration Facility, which is described in Section II. A brief description of the optical flats is given in Section III. Additional tests were also performed at the X-ray test facility of the Max Planck Institute at Garching, Germany. These tests and their results are presented in Section VI. The tests at MSFC made use of two X-ray detectors; a high-resolution imager (HRI) and a linear proportional counter (LPC). A detailed description of each of these instruments and the results of the tests are given in Sections IV and V, respectively.

The characterization of the figure and surface roughness by various visual and mechanical techniques was performed at MSFC, Lawrence Livermore Laboratory, the National Bureau of Standards, and NWC in China Lake, California. These techniques include differential scatterometry, polarization profilometry, Nomarski photography, total integrated scatter, contact profilometry, and various interferometric measurements. These techniques and results are described in Section VII.

II. X-RAY FACILITY DESCRIPTION

2.1 Introduction

The vacuum envelope of the X-Ray Calibration Facility at MSFC consists of a source chamber and an instrument chamber separated by approximately 312 m and joined by a 36 in. diameter tube (the guide tube) as shown schematically in Figure 1. The system is capable of maintaining the tube pressure in the 10^{-6} to 10^{-7} torr range. Thus, the X-rays suffer negligible absorption in traversing the 312 m distance between source and detector.

An X-ray generator is housed in the source chamber building and connects to the source chamber through a 6 in. vacuum gate valve. The X-ray generator has an integral pumping system to maintain the X-ray tube at high vacuum. A monitor proportional counter is mounted in the guide tube near the west optical baffle (Fig. 1). The electronics and data system for the monitor counter are housed in the source chamber building. The gas supply and thermal control systems are installed in a small elevated building enclosing the west optical baffle access port.

A mechanical assembly holding the X-ray flats to be tested (the test mirror assembly) and a translatable proportional counter are mounted in the guide tube just east of the east optical baffle. A small elevated building houses test electronics and the proportional counter electronics.

Finally, two X-ray detectors, a two-dimensional, high-resolution imager detector (HRI) and a one-dimensional imaging proportional counter (IPC) are located within the instrument chamber mounted on the east end of an optical bench.

X-rays generated by the source and transmitted eastward through the mirror test assembly, where they either pass directly through a thin arrow collimating slit or, after leaving the slit, are double reflected from two optical flats in a periscope geometry to the detectors mounted on the optical bench. The X-ray beam intensity is measured by the monitor proportional counter. The translatable proportional counter located east of the mirror test assembly is used to perform total reflectivity measurements.

2.2 X-Ray Generator

Facility X-ray flux is produced by a modified industrial X-ray generator (Spectro Equipment Multifocus X-Ray Radiation Generator Model 682-700B). The instrument was modified such that the X-ray tube, cold trap, and diffusion pump are attached to the facility source chamber and the X-ray tube is aligned with the guide tube center axis. Electronics and mechanical systems are mounted in a cabinet under the X-ray tube and supported by the source chamber building floor structure. Vacuum roughing, cooling oil, and electrical systems are connected to the X-ray tube through flexible couplings to minimize vibration. Schematic diagrams of the X-ray system are presented in Figures 2 and 3.

The X-ray generator is of the multifocus type which allows an accelerated electron beam to be focused to a small spot on a target anode. X-rays produced as a result of the electron-target interaction are projected directly down the guide tube to the experiment. The impact area of the electron beam is less than 1 mm with

projected dimensions of less than 1 mm in any direction. The X-ray source size is limited by the dimensions of the electron impact area rather than by an aperture and subtends less than 0.7 sec of arc with respect to the optical bench pivot. The output of the X-ray tube may be controlled over a range of photon energy and flux. Output is principally characteristic K and L emission from the anode target material. These characteristic emission lines are superimposed on a bremsstrahlung continuum. Photon energy may therefore be controlled by proper selection of target material and electron gun energy. Bremsstrahlung continuum and low energy photons may be suppressed by using filters of appropriate material and thickness. Generally, filters were constructed of the same material as the target since the characteristic emission energy of an element is slightly below the absorption edge energy. A pure element is therefore "transparent" to its own emission lines. Filter thicknesses were generally chosen to attenuate the X-ray beam by a factor of 2 to 5 at the wavelength of interest. Actual filter materials and thicknesses are given in Table 1. Filter materials were supported by stainless steel rings which were in turn attached to stainless mounting plates. A filter holder was designed and constructed to permit rapid exchange of the mounting plates with pre-attached filters. The filter holder was installed 4.5 in. east of the X-ray tube as shown in Figure 2.

In general, the X-ray generator is capable of producing discrete X-ray emission lines from Boron-K (0.1 keV) to the limit of the electron gun energy (approximately 20 keV). Flux level at the instrument chamber can be controlled over a range of 4 orders of magnitude (0.1 to 2000 photons/sec/cm^2 measured at the site of the optical bench). For the experiments described here the flux was typically 1000 photons/sec/cm^2.

2.3 The X-Ray Monitor Detectors

Both the X-ray monitor detector and the translatable detector for the reflectivity measurements are Diano Mod. SPG-9A gas flow proportional counters. Each detector is fitted with a Diano Mod. A4952FG ultra-thin (1.8 micron) polypropylene front window with a several hundred angstrom aluminized coating. Gas is supplied to each detector using the gas control system shown in Figure 4. Both gas pressure and counter temperature are closely measured and controlled to maintain a constant known gas density within the assembly. This is critical for converting the monitor counter measurements into an absolute flux measurement.

Two types of gases are available for use. For X-ray energies at or below the Al-K line (0.49 keV), a pure methane is used at a pressure of 5.0 PS/A. For X-ray energies at or above the Al-K line, P-10 (10 percent Methane and 90 percent Argon) is used.

2.4 The X-Ray Mirror Test Assembly

Test mirror flats were mounted in a fixture in the relative positions shown in Figure 1. The fixture was held in the guide tube by a servo motor-controlled assembly which could be rotated very precisely through small angles about the vertical axis. The X-ray beam was limited by an optical baffle to illuminate only the slit end of the mirror fixture. X-rays passing through the 0.012 in. x 1.0 in. slit either travelled through the 0.031 in. gap between the mirrors or underwent a double reflection off the mirror surfaces as shown in Figure 1. The grazing angle between

the X-ray beam and the mirror surface was varied with the servo-controlled mirror test assembly. Two pairs of mirror flats were held in the mirror fixture. Each pair was aligned with a vertical slit and positioned one pair above the other. The appropriate projected slit image was observed in the instrument chamber by moving the experiment detectors (HRI and LPC) horizontally or vertically with the facility optical bench.

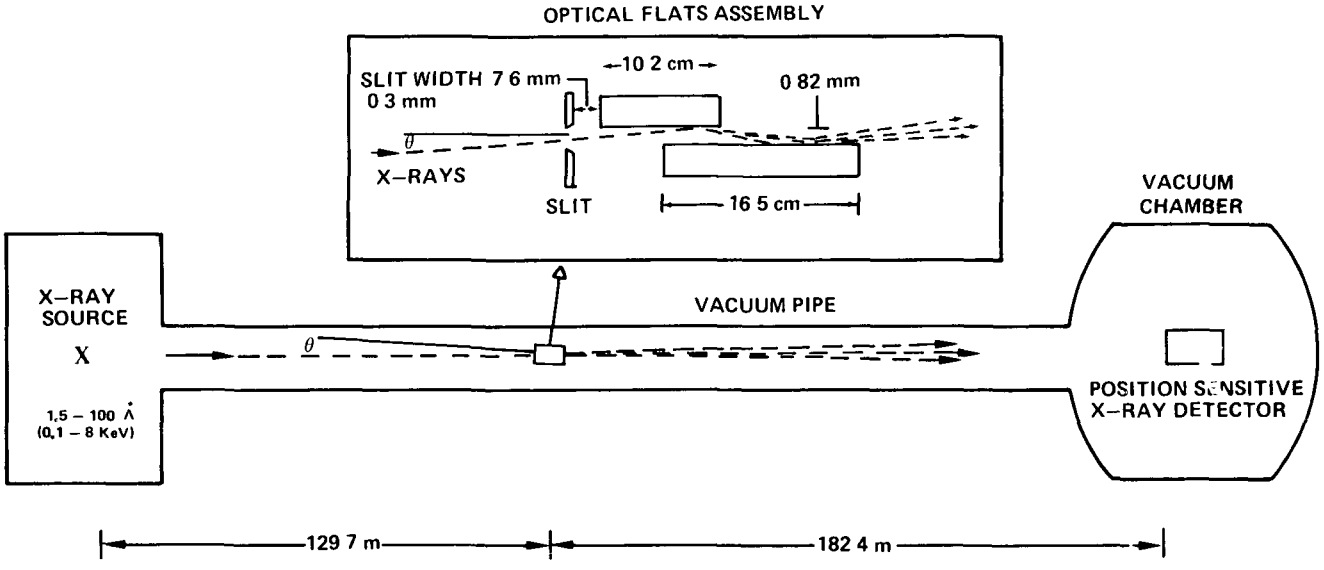

Figure 1. Schematic of the MSFC X-Ray Test Facility.

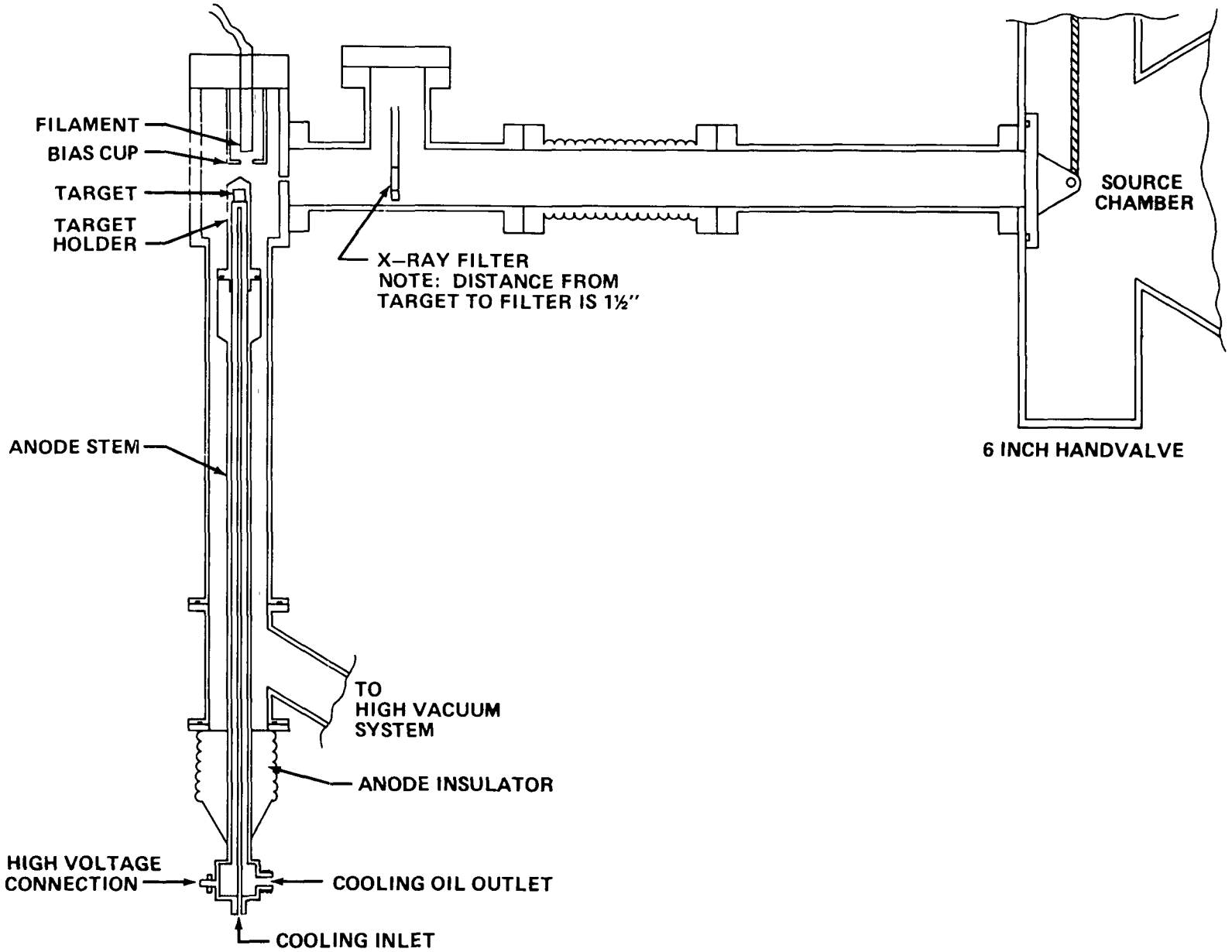

Figure 2. Schematic diagram of the X-ray generator.

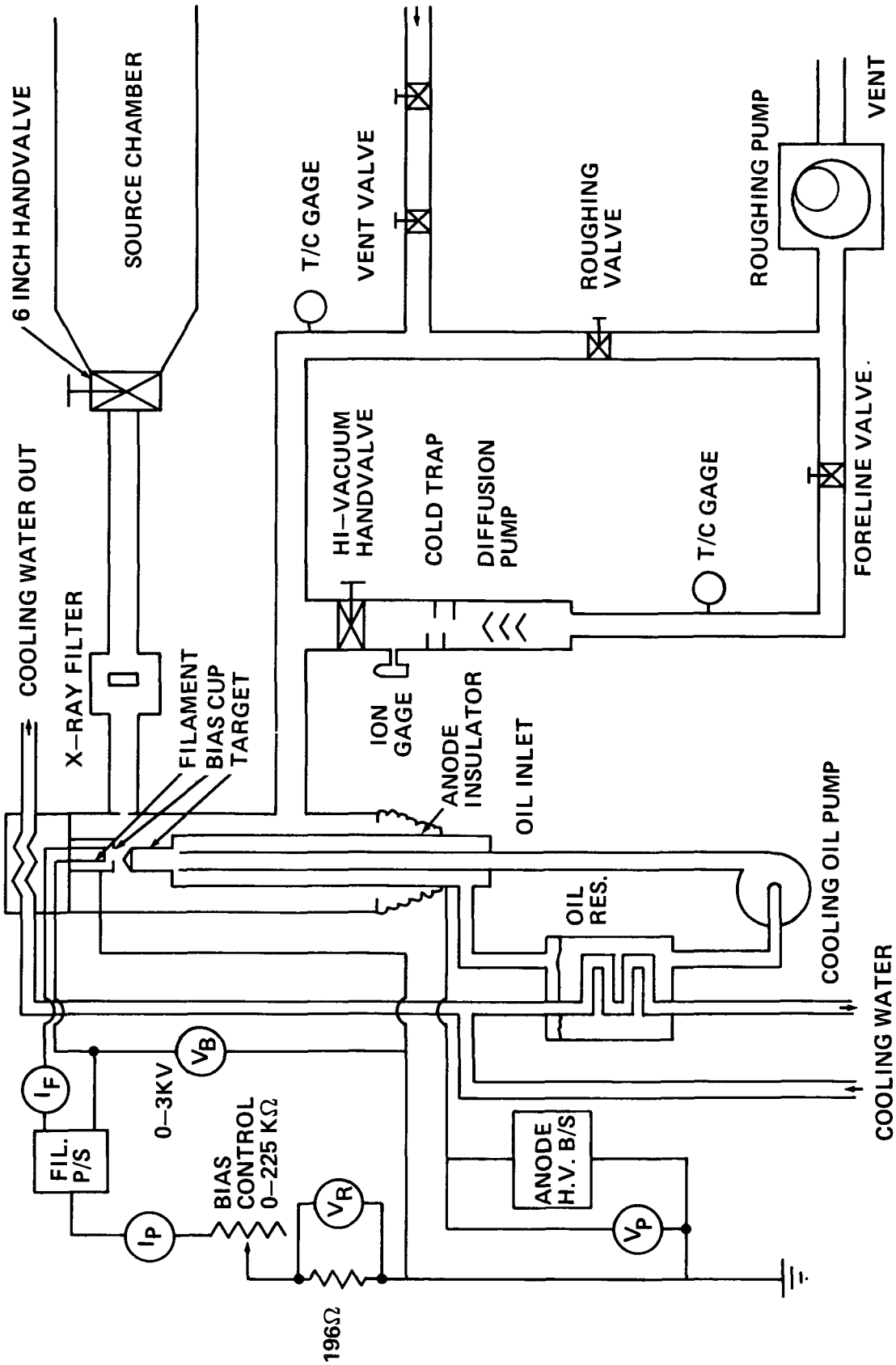

Figure 3. Schematic diagram of the X-Ray Tube Assembly.

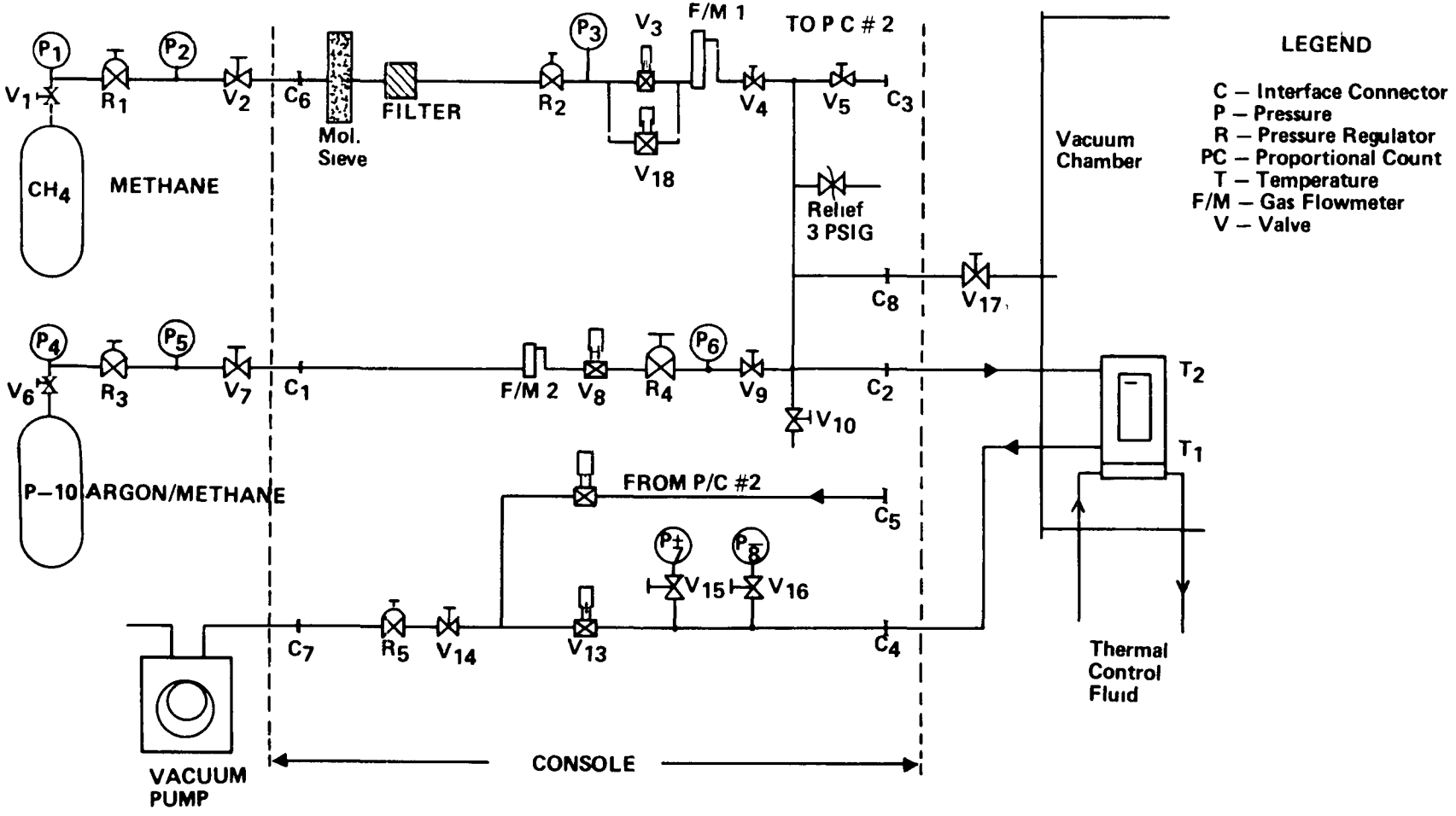

Figure 4. Schematic diagram of the Proportional Counter Gas Control System.

TABLE 1. X-RAY GENERATOR STANDARD CONFIGURATIONS

Target	X-Ray Line	Wavelength	Energy	Filter Material	Filter Thickness	P/C Window Transmission
-	-	Å	KeV	-	Microns	Percent
Be	Continuum		-	B/Poly	B 3.5 Poly 1.5	-
B	K	67	0.185	B/Poly	B 3.5 Poly 1.5	15.4 ± 0.6 (2)
C	K	44.6	0.277	C/Poly	C 2.0 Poly 1.5	27.8 ± 0.7
Ti	L	27.4	0.452	-	-	-
V	L	24.3	0.511	-	-	-
O (1)	K	23.7	0.520	Cr	0.60	8.6 (3)
Cr	L	21.7	0.572	Cr	0.60	11.1 ± 0.1 (2)
Fe	L	17.6	0.705	Ni	0.64	17.4 ± 0.3
Cu	L	13.3	0.933	Cu	0.50	29.9 ± 0.3
Al	K	8.34	1.49	Al	10.0	40.4 ± 0.2
Si (1)	K	7.13	1.74	-	-	41.7 (3)
Zr	L	6.07	2.04	Zr	2.1	42.2 ± 0.6
Ag	L	4.15	2.99	Ag	2.0	43.4 ± 0.5 (2)
Sn	L	3.60	3.44	Sn	3.0	43.7 ± 0.4 (2)
Ti	K	2.75	4.51	Ti	12.5	44.2 ± 0.3
V	K	2.51	4.95	V	25.0	45.0 ± 0.1
Cr	K	2.29	5.42	Fe	12.5	-
Fe	K	1.94	6.40	Fe	12.5	44.5 ± 0.4
Cu	K	1.54	8.06	-	-	-
Zr	K	0.787	15.77	-	-	-
Ag	K	0.561	22.12	-	-	-

(1) Silicone and oxygen available as SiO_2 doublet.

(2) Inferred from data taken with window of very similar characteristics.

(3) Interpolated from transmission data - not directly measured.

N.R. - No Requirement.

III. THE OPTICAL FLATS

Thirty-five pairs of optical flats were either purchased or donated to the program. These flats were made by Eastman Kodak, Perkin Elmer, Itek, and Carl Zeiss. The flats, their substrate, their surface coating and surface roughness as measured by MSFC's BRDF scatterometer in the visible are listed in Table 2. Other characterizations of their surface roughness are discussed in Section VI. The polishing technique for the test flats are presented in Table 20.

TABLE 2. DESCRIPTION OF THE OPTICAL TEST FLATS

Pair No.	I.D.	Substrate	Coating	RMS* Surface Height (Å)
1	EK-I-1	FS	Ni	6.1
2	EK-I-2	FS	Pt	6.6
3	EK-I-3	FS	Au	6.0
4	EK-II-1	ULE	Au	3.6
5	EK-II-2	ULE	Pt	
6	EK-II-3	ULE	Ni	13.4
7	EK-III-1	ZER	Ni	2.1
8	EK-III-2	ZER	Pt	15.8
9	EK-IV-1	CER	Ni	3.1
10	EK-IV-2	CER	Pt	5.9
11	EK-V-1	FQ	Ni	3.4
12	EK-V-2	FQ	Pt	6.9
13	EK-V-3	FS	Ni	7.1
14	EK-RCII-1	ULE	Au	8.0
15	EK-RCII-2	ULE	Au	3.1
16	MP-1-R1	ZER	Ni	11.2
17	MP-2-R2	ZER	Pt	14.5
18	MP-3-R1	ZER	Au	26.2
19	MP-RC2-R2	ZER	Au	5.5
20	PE-1-001	FS	Pt	15.3
21	PE-1-002	FS	Ni	2.0
22	PE-1-003	FS	Au	9.6
23	PE-2-001	ULE	Au	16.4
24	PE-2-003	ULE	Ni	2.3
25	PE-2-004	ULE	Pt	4.7
26	PE-3-001	ZER	Pt	6.3
27	PE-3-003	ZER	Au	6.2
28	PE-3-004	ZER	Ni	6.1
29	PE-IR&D-1	NiBe	Ni	3.6
30	PE-IR&D-2	NiBe	Pt	3.1
31	PE-SAO-1	NiBe	Ni	2.6
32	PE-SAO-2	NiBe	Pt	2.1
33	ITEK-1	FS	Ni	4.3
34	ITEK-2	FS	Pt	3.4
35	ITEK-3	ZER	Ni	4.2

* Measured with the MSFC BRDF scatterometer. The values given represent the average of the long and the short mirrors of each pair.

IV. X-RAY TESTS WITH THE LINEAR PROPORTIONAL COUNTER

4.1 The Detector

The detector used for these experiments is a one-dimensional position sensitive proportional counter manufactured by the Technology for Energy Corporation (Model 210). The Model 210 is a sealed xenon gas detector using a stainless steel anode for resistance-capacitance position encoding. The detector has a beryllium window covering an active area of 10 cm by 0.8 cm with the position sensitive axis in the longer dimension. With a 0.5 cm depth the detector is most sensitive in the energy bandwidth from about 2 to 12 keV. The position resolution depends on the applied high voltage and on the energy of the incident X-rays. For the majority of the tests, the high voltage was adjusted so that a resolution of 0.17 arc-sec (corresponding to a spatial resolution of 0.75 mm) was achieved. The detector subtends 1.9 arc-min and, by means of the optical bench, could be moved to cover ±5 arc-min of the scattered radiation.

4.2 General Testing Procedure

In general, testing with the one-dimensional detector proceeded as follows. Once the mirrors were placed in the mirror test assembly and vacuum in the test facility was achieved, one searched for the direct beam through the collimating slit. Then by fine adjustment of the angular motion of the test assembly, the angle of incidence was adjusted until the X-ray beam could pass freely through the aperture between the mirrors. This was accomplished by varying the angle of incidence until blocking of the beam by the top of the short mirror took place. Then, the assembly was rotated in the opposite direction until blocking of the beam by the back of the long mirror took place. Noting these two positions together with the known geometry of the mirror assembly allows one to determine the zero of the angle of incidence. Subsequently the direct slit image was measured. Finally the test assembly was rotated to angles of incidence of 25, 39, and 51 min of arc which covers the range of the AXAF telescope angles of incidence. Typical results for one set of flats at different angles of incidence are shown in Figures 5 through 10. A compendium of results obtained over a 2-year period is given in Tables 3a through 3i where we have listed the observed full width half maximum (FWHM), the 50 percent power point (i.e., 50 percent of the observed flux), the 90 percent power point, the reflectivity measured by the translatable proportional counter, R_{TOTAL}, and finally the theoretical reflectivity. It should be noted that the translatable counter was only recently added to the system and thus it has been used on only a subset of experiments.

4.3 Analysis of Some Specific Tests

4.3.1 Introduction

In the following paragraphs we discuss the results of a series of detailed tests performed on seven of the pairs of flats. These are listed in Table 4. It should be noted that the first five of these sets were also tested at the X-ray test facility of the Max Planck Institute of Extraterrestrial Physics, Garching, West Germany. The results of those tests are presented in Section V.

4.3.2 Effects of Fresnel Diffraction Due to Slit Geometry

In the geometry of this particular experiment, Fresnel diffraction formalism applies. In some respects, the resolution of the scattered image is a function of the width of the image due to diffraction of the slit alone. The slit image is further affected by the fact that the source is not exactly a point source. The slit image for the energies used, however, was very narrow. They typically had a full width half maximum (FWHM) of about 1.0 arc-sec with 90 percent of their flux within 0.6 arc-sec. Figure 5 shows a measured direct slit image for the X-ray wavelength of 4.15 Å (2.99 keV).

Because the direct slit image was measured experimentally before each scattering image, the actual resolution of the experiment is enhanced so that it is better than the 0.5 arc-sec resolution inherent in the direct slit image. That is, because the direct slit image was measured, it can be removed from the measured scattered image by a deconvolution. Hence the effective resolution of the experiment is determined by the resolution of the detector which is 0.17 arc-sec.

4.3.3 Effects Due to Local Figure Error of the Optical Flats

Ideally, the optical flats that were used should have been perfectly flat. Practically, however, this is impossible. To further complicate the picture, the scattered image depends upon the specific optical properties of the particular illuminated region of the flats. This illuminated region, in turn, depends upon the angle of incidence and on the specific alignment of the flats with respect to each other and with respect to the slit. Because the alignment of the mirrors is not known precisely, the exact illuminated area is also uncertain. Hence, one has to resort to using an average figure error of the surface such as that which can be obtained from a Twyman-Green interferometry measurement. By comparing the lengths of the illuminated regions to the total lengths of the surface, however, one will see that average properties of the surface may very well not be applicable. The illumination lengths corresponding to angles of incidence of 25, 39, and 51 arc-min are 1.65, 1.06, and 0.81 in., respectively.

Furthermore, although the illuminated lengths are small, they are still large enough so that variations in the figure within these lengths are still possible. To see what effect a variation in the figure can have on the reflected image, one can use the theoretical expression for the point spread function (PSF) of the slit and mirror flat system in the Fresnel formalism [1]

$$\mathrm{PSF}(\theta) = \left| \frac{1}{2W} \int_{-W}^{W} dy \, \exp\left[ik(\theta y + \beta y^2)\right] \right|^2 , \qquad (1)$$

where 2W is the slit width, θ is the angle measured from the specularly reflected direction, k is the wave number of the incident radiation, and

$$\beta = \frac{1}{2}\left(\frac{1}{D_1} + \frac{1}{D_2}\right) - \frac{2}{r \sin \theta_i} .$$

Here D_1 is the distance from the source to the slit; D_2 is the distance from the slit to the detector; r is the radius of curvature of the reflecting surface; and θ_i is the grazing angle of incidence.

Figures 11a and 11b compare the PSF for the two radii of curvatures of +10.0 km and -10.0 km both with 4.15 Å radiation at 25.0 arc-min. It is apparent from these figures that there is a significant difference between the two images with the +10.0 km images being more narrowly peaked. The effect of having variations in the radius of curvature within the illumination length would be manifested by asymmetrical images being formed. Figure 12 is an example of such an image which was obtained for the Itek Zerodur/Ni mirror with X-rays of 4.15 Å at 25 arc-min grazing incidence angle.

For the foregoing reasons, one can get a qualitative feeling for the local figure error of the mirror flats by looking at the shape of the reflected images. If the images are symmetric, then one can assume that the figures are good, and if the images are asymmetric, one can assume that the figures are poor. On this basis, of the seven mirror flats reported on in this section, the two fused silica substrate mirrors manufactured by Perkin Elmer and the Ni-Be substrate mirror manufactured by Perkin Elmer had good figure (but see below), and the other four had poor figure.

Even though the figure of the majority of the flats can be termed as poor, the effect that this has on the contrast or encircled energy of the images is not great. This is borne out experimentally by the fact that 50 percent of the flux is typically within ±0.6 arc-sec and 90 percent of it is within the range of ±2.5 arc-sec. The values of the 50 percent and 90 percent ranges of all seven flats are included in Table 3. As can be seen by the 50 percent and 90 percent ranges of the Ni-Be mirror, scattering due to surface roughness could possibly be a significant factor. Effects due to this will now be discussed.

4.3.4 Effects Due to Surface Roughness of the Optical Flats

The scattering of X-rays by surface roughness is known to be the main factor which determines the contrast of the image in X-ray optical systems. For this reason, it is important to be able to characterize as accurately as possible the effects of this scattering of the various test flats. Hence, it is desired to present the results of the scattering measurements in a way which brings out the effects of surface roughness.

In this regard, Silk [2] has demonstrated that the PSF, the line spread function (LSF), the modulation transfer function (MTF), and the edge function (ESF) do not all emphasize the same optical effect equally. It was shown that the PSF and LSF described the performance of the system equally in terms of optical figuring and scattering. On the other hand, the MTF and ESF are primarily determined by scattering. Hence, one can use either the MTF or ESF to characterize the data in order to analyze the effects of surface roughness. We will use the MTF in this paper.

The relationship between what is directly measured and the MTF is as follows. Let $R(\theta)$ represent the flux of reflected X-rays detected by the detector in the region between θ and $\theta + d\theta$, and let $I(\theta)$ represent the same quantity for the direct slit image. Then the LSF of the system is defined by the following convolution:

$$R(\theta) = LSF\ (\theta) * I(\theta) \quad . \tag{3}$$

Here it is seen that the LSF would be a delta function if there are no effects due to the figure or scatter. The MTF can be obtained from the LSF by a Fourier transformation:

$$MTF\ (f) = \int LSF\ (\theta)\ e^{-i2\pi f\theta}\ d\theta \quad . \tag{4}$$

Here it is seen that if LSF (θ) is the delta function, $\delta(\theta)$, signifying no figure error or scattering effects, then MTF (f) = 1 for all frequencies f. Physically, the modulation transfer function represents the ability of the system to preserve the contrast present in the object. It is the ratio of the modulation in the image to that in the object.

Table 5 gives the value of the MTF as a function of frequency for the seven pairs of mirrors for X-rays of energy 8.06 keV incident at 25 min grazing angle. Here it can be seen that the Itek FS/Pt and the Perkin Elmer FS/Au mirrors have very similar MTFs which indicate that their scattering properties are similar for this energy. Similarly, the Perkin Elmer FS/Pt, Perkin Elmer Ni-Be/Pt, and Eastman Kodak ULE/Ni can be seen to have similar scattering properties at this energy. The Perkin Elmer Zerodur/Ni mirror was not similar to any of the others at this energy and it exhibits the least rapidly changing MTF. Since the absence of scattering would give a MTF which remains close to unity, this indicates that this mirror has the least scattering for this energy. By the same token, the Itek FS/Pt and Perkin Elmer FS/Au have the most scattering.

Table 6 gives the MTF at 2.99 keV at 25 min grazing angle of incidence. From this table it can be seen that the mirrors Itek Zerodur/Ni, Perkin Elmer Zerodur/Ni, Perkin Elmer FS/Au, and Perkin Elmer Ni-Be/Pt have similar scattering properties. Also, the Itek FS/Pt and the Eastman Kodak ULE/Ni mirrors show similar scattering properties. These two have the most scattering at this energy as is evident by their rapidly decreasing MTF. The Perkin Elmer FS/Pt is in a class by itself at this energy and has the least scattering.

Table 7 gives the MTF at 6.14 keV and 25 min grazing angle of incidence. Although there are no clear-cut similarities of any two of the MTF at this energy, it can be seen that all of the mirrors except the Itek Zer/Ni and the Itek FS/Pt have moderately, slowly decreasing MTF. This indicates that scattering is not very significant for all except these two at this energy. As in the case of 8.06 keV, the Perkin Elmer FS/Pt apparently has the least scattering.

The fact that the scattering properties of a surface are bandwidth dependent is certainly demonstrated by a comparison of the values in Tables 5, 6, and 7 which correspond to different X-ray energies. For example, the Perkin Elmer FS/Au mirror shows much more scattering at 8.06 keV than at 2.99 keV as is seen by the fact that at f = 0.364 arc-sec^{-1}, the MTF has fallen to 0.09 for 8.06 keV, whereas it is equal to 0.32 for 2.99 keV.

Another possible effect of surface roughness would come to the fore if the surface contains very small wavelength components with moderate amplitudes. In this case, there could be significant large angle scattering of X-rays which would not be detected by our detector because of its limited range of ±5 arc-min. The total flux that reflects from the flats, however, was experimentally obtained by placing a second detector at a position just behind the mirror flats assembly. This detector was remotely controlled so that it could be brought in and out of the beam path when desired.

In this way, large angle scattering would be indicated by comparing the actual reflectivity of the mirrors as calculated by the flux from the second detector (total reflectivity) and the apparent reflectivity obtained by the flux in the limited range detector. If the apparent reflectivity is significantly lower, then this would indicate large angle scattering. These reflectivities along with a calculated theoretical reflectivity are tabulated in Table 8 for each of the seven mirror pairs. The differences listed correspond to the difference between the reflectivity and the measured (apparent) reflectivity. The discrepancy between the theoretical reflectivities and the measured values for 6.4 keV (at 39 min and 51 min) and for 8.1 keV is due to the fact that the theoretical reflectivities for these energies with the appropriate coating material is a very sensitive function of the angle of incidence. Hence, a small deviation from the assumed angle of incidence will give a large change in the reflectivity.

The reflectivities in Table 8 indicate that all seven mirrors have some significant large angle scattering at 2.99 keV. This is especially so at the larger incidence angles of 39 and 51 arc-min where as much as 17 percent of the flux is apparently scattered at large angles. At higher energies, this effect is not significant.

4.3.5 Theoretical Description of Scattering from Surface Roughness

In the smooth surface approximation, Church [1] has obtained an expression for the flux, R (θ), which should be obtained as a function of the angle from the specular direction:

$$R(\theta) = k\, c_1 \left[(1 - (2\, k \sin \theta_i)^2 \sum_{-}^{+} \langle a_n^2 \rangle)\ PSF\ (\theta) + (2\, k \sin \theta_i)^2 \sum_{-}^{+} \langle a_n^2 \rangle\ PSF\ (\theta + n\lambda/2W) \right] \quad . \tag{5}$$

In this equation, k is the wave number of the X-rays of wavelength λ; θ_i is the grazing angle of incidence; c_1 is a normalization constant; and PSF(θ) is the system point spread function which takes into account diffraction due to the slit and figure error due to an overall radius of curvature of the illuminated region. PSF (θ) is given in equation (1). The $\langle a_n^2 \rangle$'s are mean square Fourier amplitude components of the surface roughness. That is, if the mean surface (XY plane) is illuminated over the region from x = -L to x = +L it is assumed that the surface height Z(x) can be expanded in a Fourier series:

$$Z(x) = \sum_{-\infty}^{+\infty} a_n \cos\left(\frac{n\pi x}{L} + \phi_n\right) \quad , \tag{6}$$

with $a_o = 0$ for a Z = 0 mean surface. Hence, the amplitude a_n corresponds to a surface wavelength of d = 2L/n.

The physical interpretation of equation (5) is that each term of the form PSF $(\theta + n\lambda/2W)$ is the contribution to the flux due to the nth Fourier surface height component and it is in the shape of the system PSF but displaced from the specular direction by an angle $n\lambda/2W$. As was discussed in section 4.3.3, all of the measured flux essentially fell in a very small region near the central core. This indicates that only the first few Fourier amplitudes could be significant.

An effort to fit the measured flux to equation (5) by the least squares method, indicated that a reasonable fit could be obtained for all the mirrors except the Ni-Be substrate only if the n = 1 component was the sole contributor to the scattering. When this is coupled with the experimental result that for small X-ray energies there was significant amount of flux at some large undetermined angle(s), the nature of the Fourier amplitudes can be ascertained. These results indicate that $|a_1|$ is very much larger than $|a_n|$ for n = 2, 3, ... N-1, where N is defined so that the large angle scattering occurs predominantly near the angle $N\lambda/2W$. The terms near n = N would then have moderate size amplitudes relative to a_1 in order to account for the flux at large angles.

This shows that any theoretical model which predicts the Fourier amplitudes of the surface roughness (i.e., the surface power spectral density) must predict amplitudes which drop very rapidly with n and then have a secondary maximum at a sufficiently large n. This rules out, for example, the Brownian or scale-invariant model for the power spectral density [1]:

$$W(p) = C/p^2 \tag{7}$$

which predicts Fourier coefficients given by

$$\langle a_n^2 \rangle = \frac{6}{5\pi} \frac{CL}{n^2} \left[1 - \frac{5}{\pi^2} \frac{1}{n^2}\right] \tag{8}$$

This is ruled out because these coefficients drop off monotonically with increasing n.

The shot model description of the surface roughness, however, can explain this behavior. In this model, the surface roughness is viewed as a distribution of defects such as grooves and ridges, pits and bosses. If $Z_o(X)$ is the shape function for a particular defect, then the scattering intensity due to the defect is proportional to the form factor defined by:

$$F(P) = \frac{1}{2L} \left| \int_{-L}^{L} e^{iPX} Z_o(X)\, dX \right|^2 \quad . \tag{9}$$

One can see that the amplitude a_n defined in equation (6) is proportional to F(P). In fact, the relationship between P and n is that each n corresponds to a particular discrete value of P:

$$P = n\pi/L \quad . \tag{10}$$

In the limit of large spatial wavenumber P, the form factor assumes the asymptotic behavior [3]:

$$F(P) \xrightarrow[aP \to \infty]{} \frac{2}{\pi} \left[Z_o^{(r)}(a) \frac{\sin (aP - r\pi/2)}{P^{r+1}} \right]^2 \quad , \tag{11}$$

where a is the size of the defect and r is the order of the lowest order nonvanishing derivative of Z_o at its edges.

For a rectangular defect, this limiting expression for the form factor reduces to the familiar $(\text{Sin } (aP)/aP)^2$ pattern. Hence, assuming that the flux scattered at the "large angles" occurs near the second maximum of this diffraction pattern, then the value of P which accounts for this scattering is $P = \pi/2a$. One can use this information, coupled with the fact that this maximum occurs at an angle larger than any in which measurements were taken (±5 arc-min), to put an upper limit on a.

From equation (10), the value of n corresponding to the second maximum is given by

$$N = L/2a \quad . \tag{12}$$

For the rectangular slit geometry used in the experiment, the illumination length 2L of the surface is related to the slit width 2W and the grazing angle of incidence via:

$$2L = 2W/\sin \theta_i \quad . \tag{13}$$

Hence,

$$N = W/(2a \sin \theta_i) \quad . \tag{14}$$

Recalling that each term, n, corresponds to a contribution to the scattered flux in the form of the system's PSF but centered at the scattering angle of $n\lambda/2W$, the value N corresponds to flux concentrated at the angle

$$\theta_N = \lambda/4a \sin \theta_i \quad . \tag{15}$$

Using $\theta_N > 5$ arc-min gives the desired limit on the size of the defect:

$$a \leq \frac{540\ \lambda}{\pi \sin \theta_i} \quad . \tag{16}$$

For the wavelength 4.15 Å (2.99 keV) at which this effect apparently exists in the experimental results, this gives the maxima 9.81, 6.29, and 4.81 μm for the angles of incidence 25 min, 39 min, and 51 min, respectively. For the higher energy X-rays (e.g., λ = 1.94 Å) the corresponding maxima are 4.59, 2.94, and 2.24 μm. From the absence of a noticeable effect due to large angle scattering at 1.94 Å, one is led to the conclusion that the surface tested in these experiments had an appreciable number of defects with sizes in the range between 4.59 and 9.81 μm. This information could presumably be used to ascertain the origin of these defects.

4.3.6 Summary and Conclusions

Based on the experimental results, one can draw several significant conclusions which have an impact on AXAF or any grazing incidence angle reflecting X-ray telescope. On one hand it has been demonstrated that scattering phenomena could be kept to a level so that most of the encircled energy does lie within a few arc seconds for the range of energies used in this experiment (2.99 to 8.06 keV). On the other hand, it has been shown that a theoretical description of the scattering is not an easy task. For one thing, the scattering is bandwidth dependent in terms of both the energy band and the illumination length of the reflecting surface. A further feature was seen to be the scattering of radiation at large angles due to a significant amount of small wavelength surface defects.

For all the glass substrate mirrors, the scattering appeared to be all concentrated near the central core or it appeared in two "groups": one near the central core and one at some large angle (> 5 arc-min). But the Ni-Be substrate mirror gave a completely different image. It gave a significant distribution of flux for a wide range of scattering angles. However, a comparison of the MTF of the Ni-Be one was similar to some of the glass ones which indicates that the spread of its image is due mainly to figure error.

Two types of experiments are needed to entertain theoretical models for describing surface roughness. One is an experiment in which mirrors are used which are not so smooth so that more than one surface amplitude will contribute to the flux near the core. Another type of experiment would be a high resolution experiment as has been described in this section but including larger scattering angles so that large angle scattering could be measured and analyzed in terms of surface defects. The first type of experiment is already planned to be done at MSFC and the results will be presented in a scientific journal.

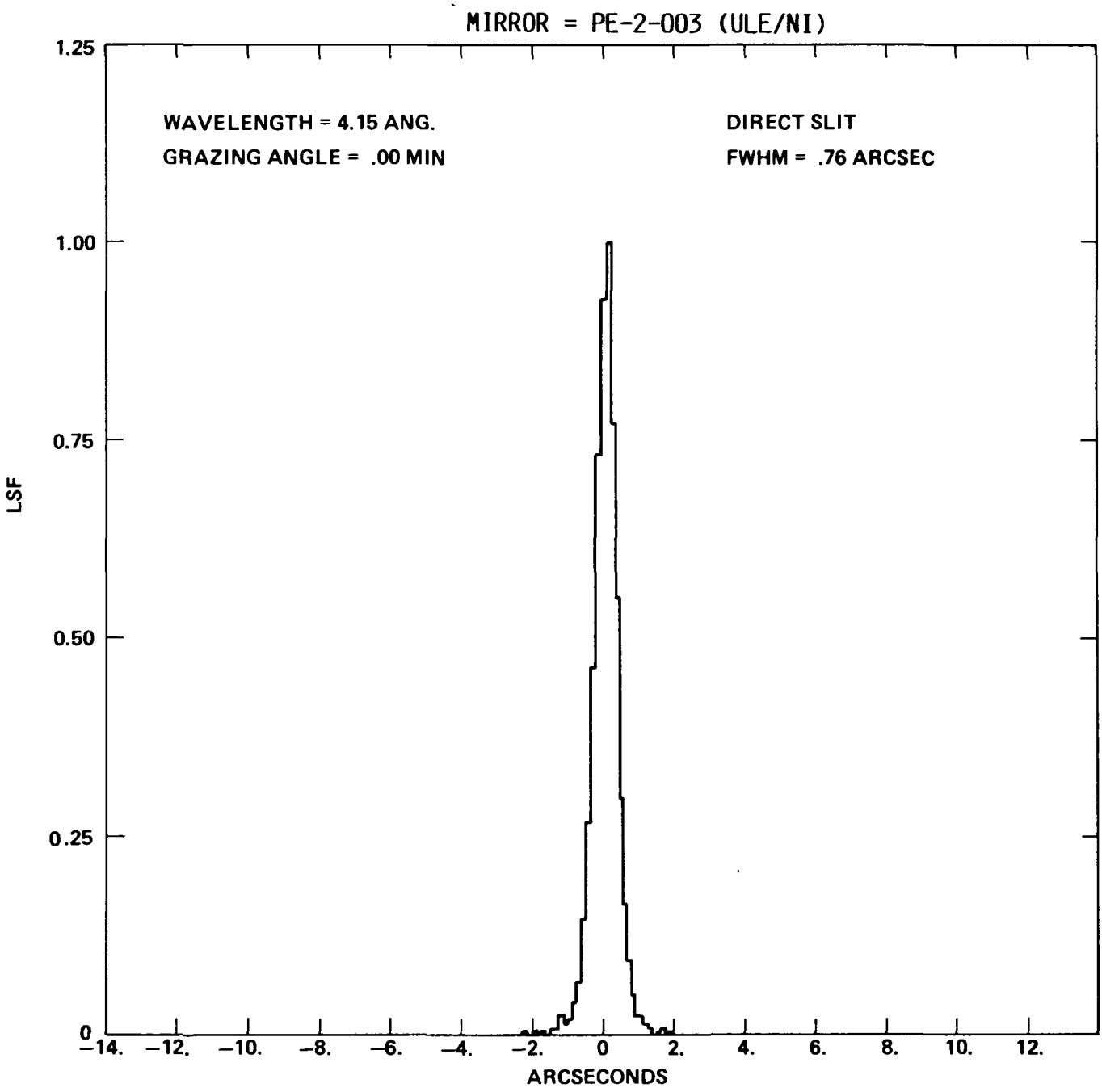

Figure 5. The direct slit image measured with the one-dimensional proportional counter, λ = 4.15 Å.

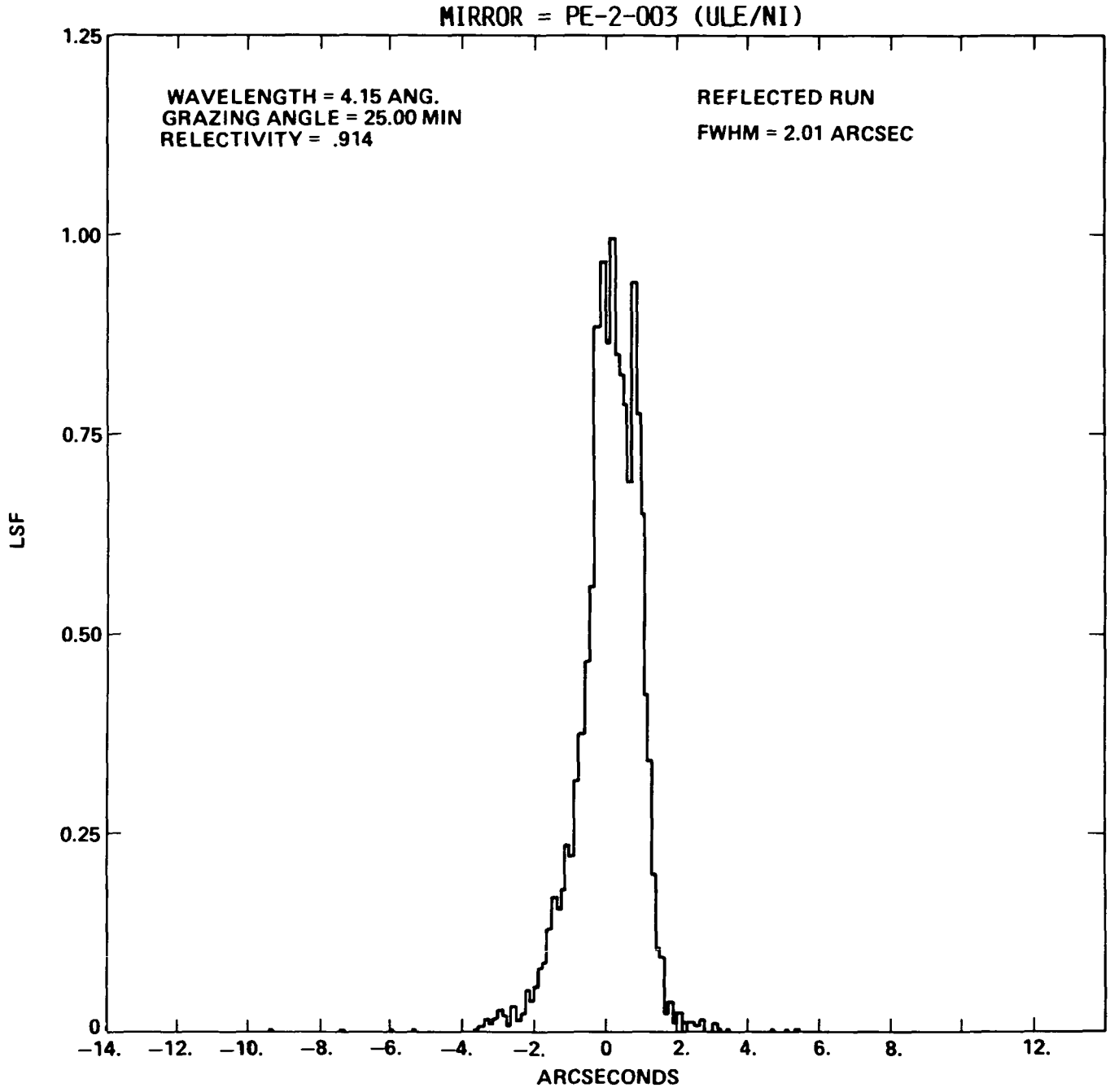

Figure 6. The 25 min incidence angle image at λ = 4.15 Å with the PE-2-003 (ULE/Ni) mirror pair.

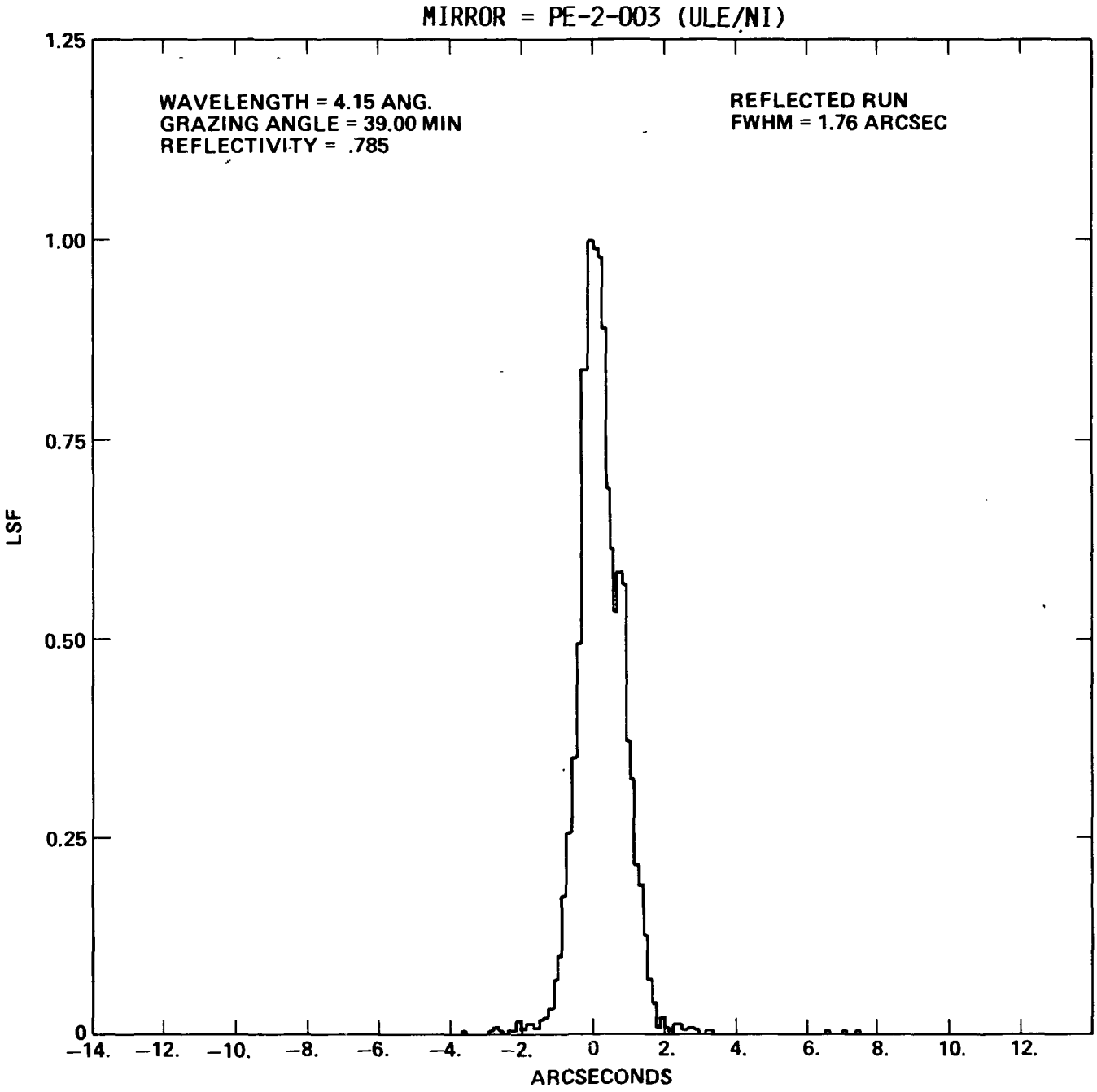

Figure 7. Same as Figure 6 except θ = 39 min.

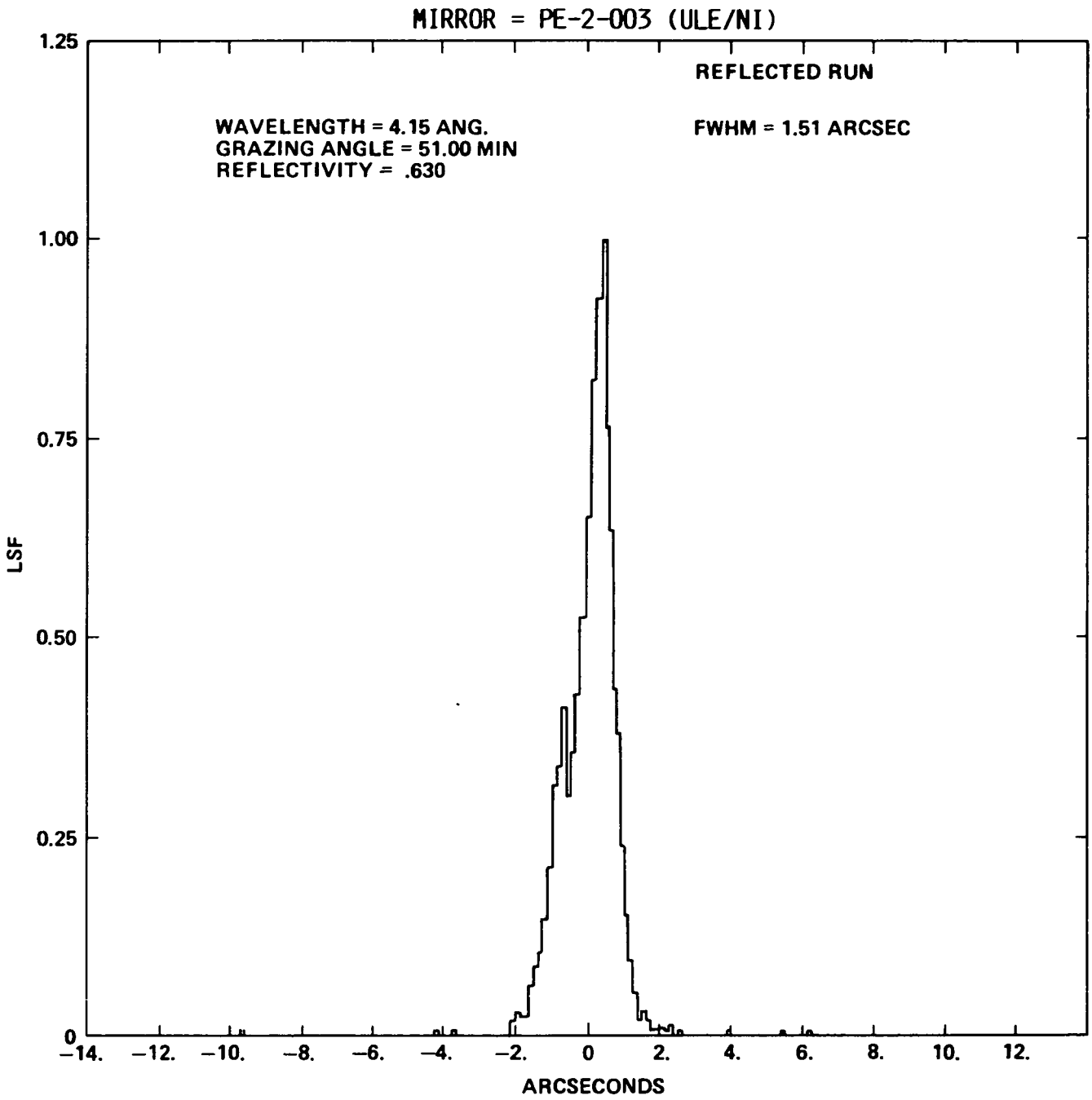

Figure 8. Same as Figure 6 except θ = 51 min.

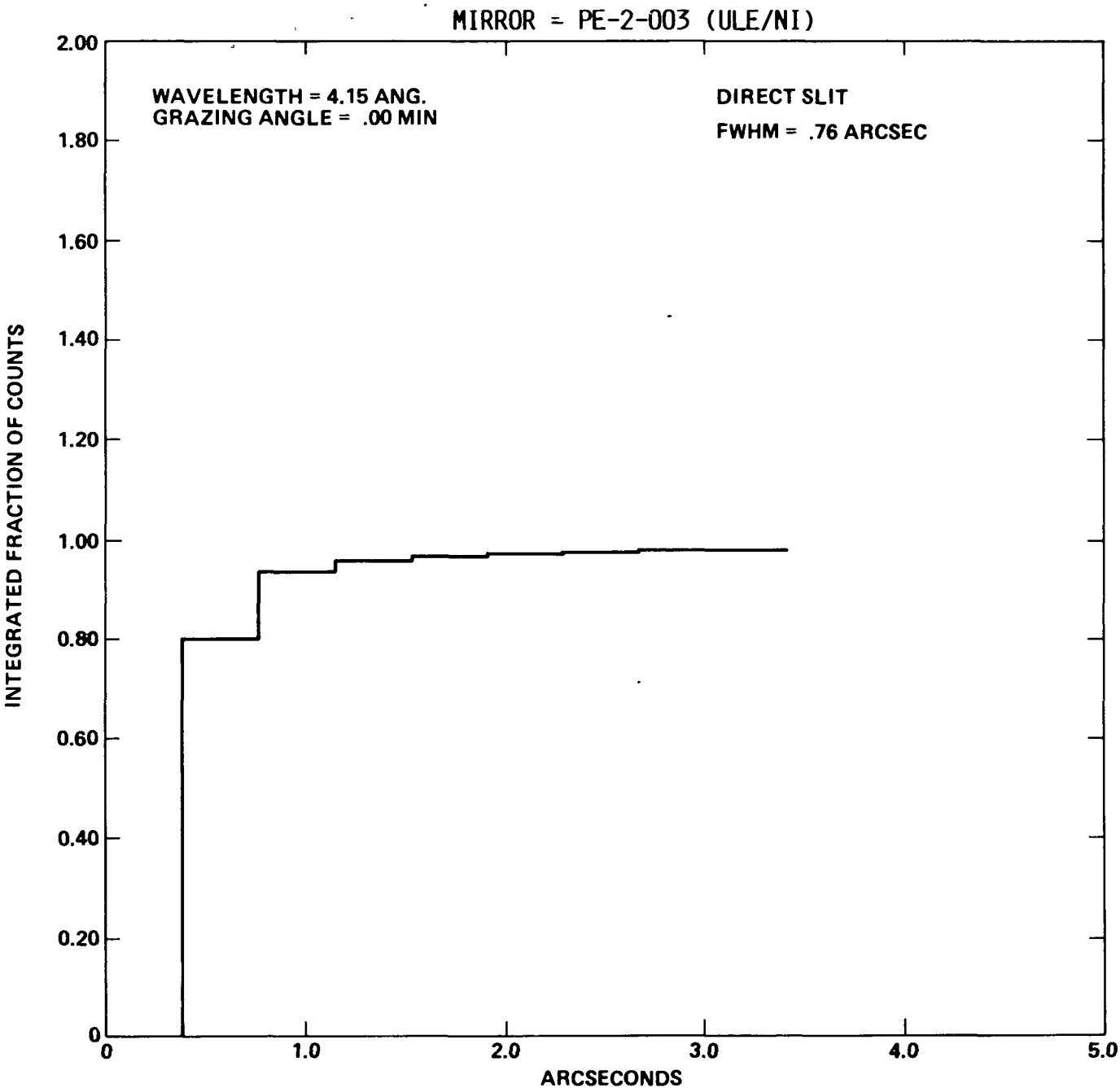

Figure 9. The integrated fraction of counts within the scattering angle of $\pm\phi$ as a function of ϕ for the direct slit image of Figure 5.

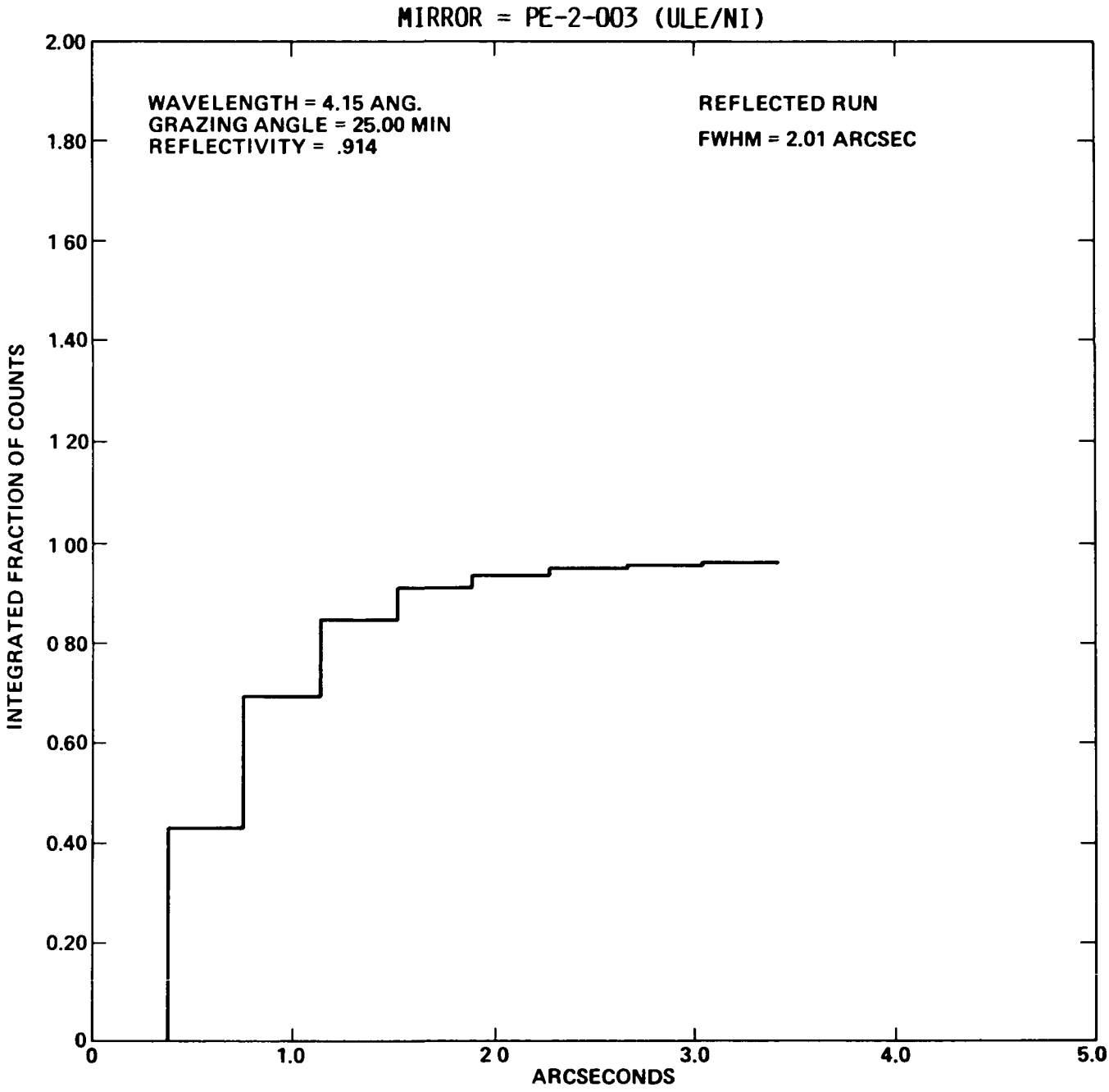

Figure 10. Same as Figure 9 except this is for the 25 min image.

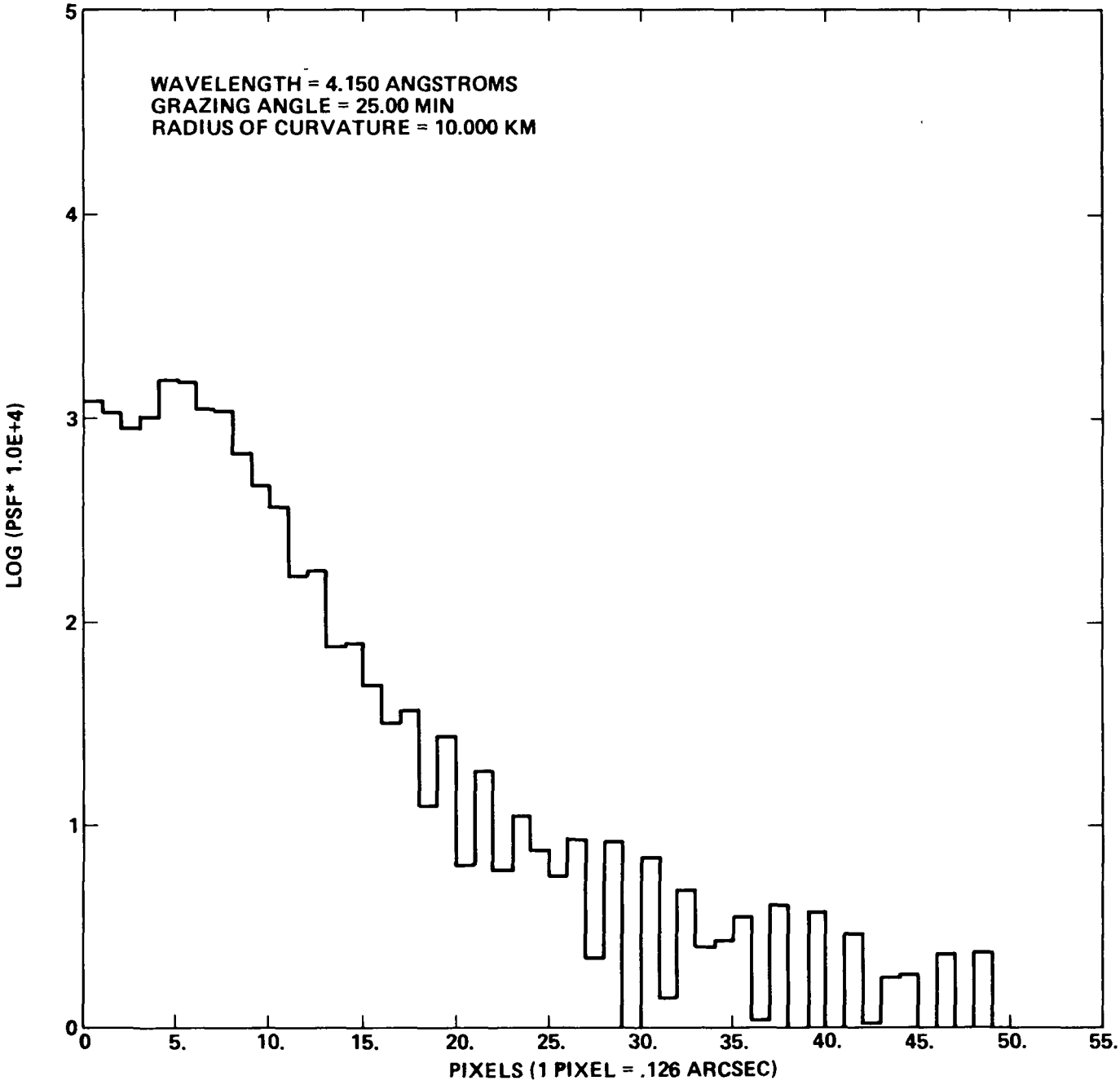

Figure 11a. The theoretical point spread function using a radius of curvature of +10.0 km, angle of incidence of 25 min, and X-ray wavelength of 4.15 Å.

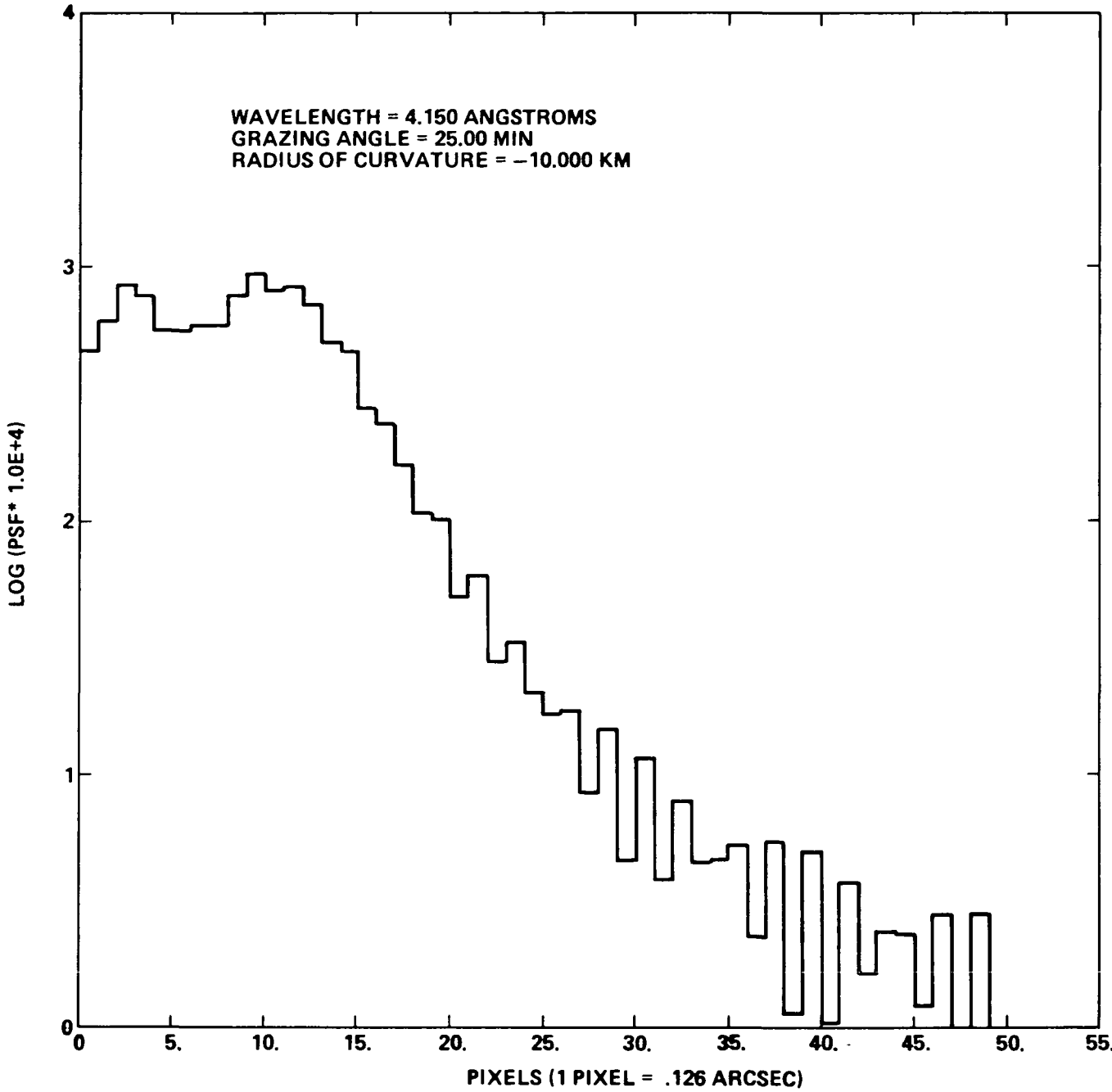

Figure 11b. Same as Figure 11a except the radius of curvature is -10.0 km.

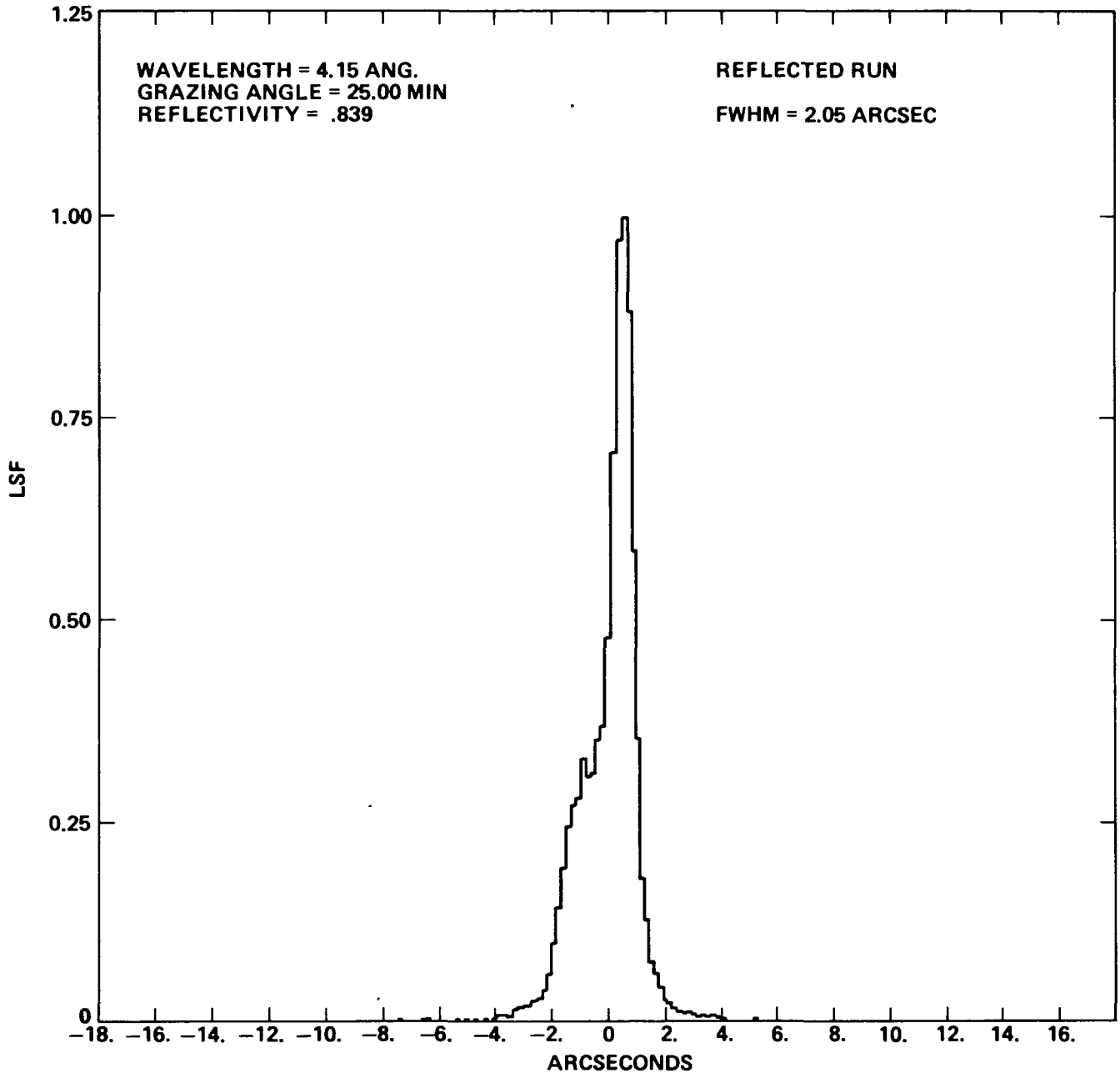

Figure 12. The 25 min image at 4.15 Å for the Itek Zerodur/Ni mirror pair illustrating the asymmetry in the image.

TABLE 3a. SUMMARY OF X-RAY SCATTERING RESULTS WITH THE PROPORTIONAL COUNTER (E = 8.01 keV, θ_i = 25 min)

Manufacturer	Substrate	Coating	FWHM	50% Power Point	90% Power Point	R_{Total}	R_{LPC}	R_{Theory}
Eastman Kodak	FS	Au	1.51	0.5	6.2		0.67	0.76
Eastman Kodak	ULE	Ni	0.68	0.6	3.7	0.32	0.28	0.08
Max Planck	Zer	Au	6.2	1.4	3.0		0.69	0.76
Perkin Elmer	FS	Pt	2.39	0.5	1.7	0.75	0.72	0.76
Perkin Elmer	FS	Au	2.39	0.6	2.2	0.79	0.80	0.76
Perkin Elmer	ULE	Ni	2.27	0.5	1.6		0.38	0.08
Perkın Elmer	Zer	Pt	1.26	0.3	0.9		0.75	0.76
Perkin Elmer	Zer	Au	2.32	0.5	1.3		0.66	0.76
Perkin Elmer	Zer	Ni	1.02	0.4	2.0	0.33	0.29	0.08
Perkın Elmer	Ni-Be	Pt	1.71	0.8	90.0	0.73	0.72	0.76
Itek	FS	Pt	3.41	0.7	3.4	0.70	0.68	0.76

TABLE 3b. SUMMARY OF X-RAY SCATTERING RESULTS WITH THE PROPORTIONAL COUNTER (E = 8.01 keV, θ_i = 39 min)

Manufacturer	Substrate	Coatıng	FWHM	50% Power Point	90% Power Point	R_{Total}	R_{LPC}	R_{Theory}
Eastman Kodak	FS	Au	1.01	0.3	5.0		0.26	0.07
Eastman Kodak	ULE	Au	1.51	0.5	13.0		0.13	0.07
Max Planck	Zer	Au	1.29	0.4	1.1		0.26	0.07
Perkin Elmer	FS	Pt	0.68	0.7	40.0	0.13	0.12	0.07
Perkin Elmer	FS	Au	1.37	0.4	1.6	0.20	0.18	0.07
Perkin Elmer	ULE	Ni	1.51	0.5	1.3		0.22	0.007
Perkin Elmer	ULE	Pt	0.76	0.3	1.0		0.38	0.07
Perkin Elmer	Zer	Au	1.55	0.4	1.3		0.24	0.07
Perkin Elmer	Zer	Ni	1.02	1.5	50.0	0.10	0.061	0.007
Perkin Elmer	Nı-Be	Pt	1.02	2.0	52.0	0.15	0.11	0.07
Itek	FS	Pt	0.34	1.3	46.0	0.14	0.11	0.07

TABLE 3c. SUMMARY OF X-RAY SCATTERING RESULTS WITH THE PROPORTIONAL COUNTER (E = 8.01 keV, θ_i = 51 min)

Manufacturer	Substrate	Coating	FWHM	50% Power Point	90% Power Point	R_{Total}	R_{LPC}	R_{Theory}
Max Planck	Zer	Au	0.76	0.3	8.0		0.12	0.015
Perkin Elmer	FS	Pt	0.34	22.0	60.0	0.03	0.038	0.015
Perkin Elmer	FS	Au	0.34	2.1	64.0	0.065	0.051	0.015
Perkin Elmer	ULE	Ni	2.01	0.5	8.0		0.14	
Perkin Elmer	Zer	Au	1.29	0.3	1.2		0.13	0.015
Perkin Elmer	Ni-Be	Pt	0.34	0.7	3.0	0.039	0.024	0.015
Itek	FS	Pt	0.34	40.0	70.0	0.017	0.026	0.015

TABLE 3d. SUMMARY OF X-RAY SCATTERING RESULTS WITH THE PROPORTIONAL COUNTER (E = 6.4 keV, θ_i = 25 min)

Manufacturer	Substrate	Coating	FWHM	50% Power Point	90% Power Point	R_{Total}	R_{LPC}	R_{Theory}
Eastman Kodak	FS	Au	1.51	0.4	2.3		0.73	0.80
Eastman Kodak	ULE	Ni	1.37	0.7	3.2	0.89	0.84	0.92
Eastman Kodak	Zer	Pt	1.47	0.5	5.0		0.69	0.80
Max Planck	Zer	Au	4.91	1.3	8.0		0.69	0.80
Perkin Elmer	FS	Pt	1.71	0.5	1.2	0.78	0.75	0.80
Perkin Elmer	FS	Au	2.05	0.4	1.6	0.83	0.80	0.80
Perkin Elmer	ULE	Pt	2.01	0.4	1.5		0.73	0.80
Perkin Elmer	Zer	Au	3.10	0.8	1.2		0.73	0.80
Perkin Elmer	Zer	Ni	1.37	0.4	1.7	0.90	0.85	0.92
Perkin Elmer	Ni-Be	Pt	2.05	0.7	76.0	0.76	0.75	0.80
Itek	FS	Pt	3.07	0.7	3.5	0.77	0.74	0.80
Itek	Zer	Ni	6.14	1.2	2.8	0.90	0.86	0.92

TABLE 3e. SUMMARY OF X-RAY SCATTERING RESULTS WITH THE PROPORTIONAL COUNTER (E = 6.4 keV, θ_i = 39 min)

Manufacturer	Substrate	Coating	FWHM	50% Power Point	90% Power Point	R_{Total}	R_{LPC}	R_{Theory}
Eastman Kodak	FS	Au	0.76	0.3	3.0		0.32	0.53
Eastman Kodak	ULE	Ni	0.34	1.8	30.0	0.15	0.098	0.07
Eastman Kodak	Zer	Pt	0.30	30.0	78.0		0.061	0.53
Max Planck	Zer	Au	1.03	0.4	150.0		0.42	0.53
Perkin Elmer	FS	Pt	1.02	0.7	2.2	0.43	0.41	0.53
Perkin Elmer	FS	Au	1.71	0.4	1.4	0.53	0.50	0.53
Perkin Elmer	ULE	Ni	0.50	10.0	70.0		0.04	0.07
Perkin Elmer	Zer	Au	0.77	0.3	1.1		0.26	0.53
Perkin Elmer	Zer	Ni	2.05	0.52	22.0	0.14	0.099	0.07
Perkin Elmer	Ni-Be	Pt	1.37	3.0	127.0	0.37	0.038	0.53
Itek	FS	Pt	3.41	0.7	5.1	0.32	0.32	0.53
Itek	Zer	Ni	3.07	1.7	24.0	0.15	0.095	0.07

TABLE 3f. SUMMARY OF X-RAY SCATTERING RESULTS WITH THE PROPORTIONAL COUNTER (E = 6.4 keV, θ_i = 51 min)

Manufacturer	Substrate	Coating	FWHM	50% Power Point	90% Power Point	R_{Total}	R_{LPC}	R_{Theory}
Eastman Kodak	ULE	Ni	0.34	47.0	67.0		0.047	0.014
Max Planck	Zer	Au	0.26	10.0	28.0		0.028	0.09
Perkin Elmer	FS	Pt	1.02	1.2	52.0	0.088	0.066	0.09
Perkin Elmer	FS	Au	1.02	0.4	29.0	0.11	0.090	0.09
Perkin Elmer	Ni-Be	Pt	1.02	12.0	60.0	0.08	0.051	0.09
Itek	FS	Pt	1.37	3.2	56.0	0.073	0.056	0.09

TABLE 3g. SUMMARY OF X-RAY SCATTERING RESULTS WITH THE PROPORTIONAL COUNTER (E = 2.99 keV, θ_i - 25 min)

Manufacturer	Substrate	Coating	FWHM	50% Power Point	90% Power Point	R_{Total}	R_{LPC}	R_{Theory}
Eastman Kodak	FS	Pt	1.26	0.4	2.4		0.68	0.73
Eastman Kodak	FS	Au	2.01	0.5	1.5		0.73	0.73
Eastman Kodak	ULE	Ni	1.02	0.6	3.7	0.91	0.81	0.92
Eastman Kodak	Zer	Ni	0.76	0.3	8.0		0.86	0.92
Eastman Kodak	Zer	Pt	1.51	0.6	53.0		0.60	0.73
Eastman Kodak	ULE	Au	1.26	0.3	10.0		0.52	0.73
Max Planck	Zer	Ni	0.76	0.3	17.0		0.79	0.92
Max Planck	Zer	Au	4.65	1.3	3.7		0.67	0.73
Perkin Elmer	FS	Pt	1.02	0.4	1.7	0.75	0.72	0.73
Perkin Elmer	FS	Au	2.05	0.4	2.0	0.80	0.79	0.73
Perkin Elmer	ULE	Ni	2.01	0.5	1.5		0.91	0.92
Perkin Elmer	ULE	Pt	2.01	0.5	1.4		0.71	0.73
Perkin Elmer	Zer	Pt	1.51	0.3	0.9		0.79	0.73
Perkin Elmer	Zer	Au	2.07	0.6	1.7		0.69	0.73
Perkin Elmer	Zer	Ni	0.68	0.4	1.7	0.92	0.83	0.92
Perkin Elmer	Ni-Be	Pt	1.37	0.5	26.0	0.74	0.72	0.73
Itek	FS	Ni	6.14	1.2	2.7	0.92	0.85	0.92
Itek	FS	Pt	2.39	0.7	3.6	0.75	0.72	0.73
Itek	Zer	Ni	2.05	0.4	1.8	0.93	0.84	0.92

TABLE 3h. SUMMARY OF X-RAY SCATTERING RESULTS WITH THE PROPORTIONAL COUNTER (E = 2.99 keV, θ_i = 39 min)

Manufacturer	Substrate	Coating	FWHM	50% Power Point	90% Power Point	R_{Total}	T_{LPC}	R_{Theory}
Eastman Kodak	FS	Pt	2.77	0.6	8.8		0.53	0.58
Eastman Kodak	FS	Au	0.76	0.3	1.1		0.55	0.58
Eastman Kodak	ULE	Ni	5.8	1.7	7.5	0.84	0.67	0.86
Eastman Kodak	Zer	Ni	1.01	0.3	3.0		0.79	0.86
Eastman Kodak	ULE	Au	1.26	0.4	16.0		0.33	0.58
Max Planck	Zer	Ni	0.76	0.4	27.0		0.71	0.86
Max Planck	Zer	Au	1.29	0.4	1.3		0.46	0.58
Perkin Elmer	FS	Pt	1.02	0.6	3.2	0.61	0.51	0.58
Perkin Elmer	FS	Au	1.02	0.4	1.6	0.68	0.60	0.58
Perkin Elmer	ULE	Ni	1.76	0.4	1.2		0.79	0.86
Perkin Elmer	ULE	Pt	0.76	0.3	0.8		0.54	0.58
Perkin Elmer	Zer	Pt	2.01	0.4	1.1		0.59	0.58
Perkin Elmer	Zer	Au	1.55	0.5	1.7		0.49	0.58
Perkin Elmer	Zer	Ni	2.39	0.6	2.0	0.85	0.68	0.86
Perkin Elmer	Ni-Be	Pt	0.68	0.4	67.0	0.59	0.52	0.58
Itek	FS	Ni	3.75	0.8	2.2	0.85	0.73	0.86
Itek	FS	Pt	2.73	0.7	2.7	0.61	0.53	0.58
Itek	Zer	Ni	7.17	2.1	3.7	0.87	0.70	0.86

TABLE 3i. SUMMARY OF X-RAY SCATTERING RESULTS WITH THE PROPORTIONAL COUNTER (E = 2.99 keV, θ_i = 51 min)

Manufacturer	Substrate	Coating	FWHM	50% Power Point	90% Power Point	R_{Total}	R_{LPC}	R_{Theory}
Eastman Kodak	FS	Au	0.76	0.3	1.5		0.41	0.46
Eastman Kodak	ULE	Ni	1.26	0.3	2.6	0.71	0.60	0.78
Eastman Kodak	Zer	Ni	0.76	0.3	16.4		0.69	0.78
Eastman Kodak	ULE	Au	2.01	0.7	32.0		0.22	0.46
Max Planck	Zer	Ni	1.26	0.6	57.0		0.50	0.78
Max Planck	Zer	Au	1.29	0.4	26.0		0.31	0.46
Perkin Elmer	FS	Pt	3.41	0.7	2.8	0.48	0.38	0.46
Perkin Elmer	FS	Au	0.68	0.6	2.1	0.54	0.48	0.46
Perkin Elmer	ULE	Ni	1.51	0.4	1.5		0.63	0.78
Perkin Elmer	ULE	Pt	1.26	0.3	1.6		0.40	0.46
Perkin Elmer	Zer	Pt	0.76	0.3	0.6		0.44	0.46
Perkin Elmer	Zer	Au	1.29	0.4	1.7		0.39	0.46
Perkin Elmer	Zer	Ni	4.78	1.2	1.7	0.72	0.59	0.78
Perkin Elmer	Ni-Be	Pt	1.71	0.7	95.0	0.46	0.39	0.46
Itek	FS	Ni	4.78	1.2	2.7	0.74	0.64	0.78
Itek	FS	Pt	6.48	1.7	3.7	0.48	0.42	0.46
Itek	Zer	Ni	1.02	0.6	2.7	0.78	0.61	0.78

TABLE 4. DESCRIPTION OF OPTICAL FLATS ON WHICH A DETAILED ANALYSIS IS DONE OF THE X-RAY SCATTERING RESULTS

Manufacturer	Substrate	Coating	RMS (Å) Surface Roughness* Long	Short
Perkin Elmer	Fused Silica	Pt	21.6 ± 12.6	9.0 ± 1.65
Perkin Elmer	Fused Silica	Au	7.5 ± 1.87	11.7 ± 2.05
Perkin Elmer	Zerodur	Ni	6.3 ± 1.85	5.8 ± 0.57
Itek	Fused Silica	Pt	2.8 ± 0.31	4.0 ± 0.64
Itek	Zerodur	Ni	4.2 ± 0.64	4.1 ± 0.40
Perkin Elmer	Ni-Be	Pt	2.6 ± 0.45	3.5 ± 0.93
Eastman Kodak	ULE	Ni	23.2 ± 12.98	3.6 ± 1.17

*Measured with the MSFC BRDF Scatterometer.

TABLE 5. THE MODULATION TRANSFER FUNCTION FOR THE MIRRORS IN TABLE 4 FOR X-RAYS INCIDENT AT 25 arc-min AND 8.06 keV

Frequency (arc-sec^{-1})	Itek Zer/Ni	PE FS/Pt	Itek FS/Pt	PE Zer/Ni	PE FS/Au	PE Ni-Be/Pt	EK ULE/Ni
0		1.0	1.0	1.0	1.0	1.0	1.0
0.05						0.87	
0.09			0.70		0.80	0.77	
0.14						0.69	
0.18		0.67	0.35	0.69	0.48	0.60	0.58
0.23						0.51	
0.27			0.22		0.25	0.42	
0.32						0.33	
0.36		0.26	0.079	0.39	0.090	0.25	0.27
0.41						0.18	
0.46					0.047	0.083	
0.50						0.034	
0.55		0.059		0.20		0.018	0.096
0.59						0.024	
0.64							
0.68							
0.73							

TABLE 6. THE MODULATION TRANSFER FUNCTION FOR THE MIRRORS IN TABLE 4 FOR X-RAYS INCIDENT AT 25 arc-min AND 2.99 keV

Frequency ($arc\text{-}sec^{-1}$)	Itek Zer/Ni	PE FS/Pt	Itek FS/Pt	PE Zer/Ni	PE FS/Au	PE Ni-Be/Pt	EK ULE/Ni
0	1.0	1.0	1.0	1.0	1.0	1.0	1.0
0.05							
0.09			0.70	0.89	0.85	0.89	0.78
0.14							
0.18	0.66	0.77	0.34	0.71	0.63	0.75	0.45
0.23							
0.27			0.18	0.55	0.45	0.61	0.23
0.32							
0.36	0.29	0.53	0.006	0.44	0.32	0.46	0.02
0.41							
0.46				0.37	0.22	0.33	
0.50							
0.55	0.21	0.43		0.27	0.19	0.25	
0.59							
0.64				0.12		0.21	
0.68							
0.73	0.034	0.35		0.078			

TABLE 7. THE MODULATION TRANSFER FUNCTION FOR THE MIRRORS IN TABLE 4 FOR X-RAYS INCIDCENT AT 25 arc-min AND 6.1 keV

Frequency (arc-sec^{-1})	Itek Zer/Ni	PE FS/Pt	Itek FS/Pt	PE Zer/Ni	PE FS/Au	PE Ni-Be/Pt	EK ULE/Ni
0	1.0	1.0	1.0	1.0	1.0	1.0	1.0
0.05			0.87			0.85	0.91
0.09	0.61	0.89	0.65	0.87	0.88	0.77	0.78
0.14			0.44			0.69	0.63
0.18	0.016	0.71	0.28	0.63	0.68	0.60	0.50
0.23			0.19			0.51	0.42
0.27		0.54	0.13	0.43	0.49	0.44	0.36
0.32			0.061			0.36	0.30
0.36		0.40	0.042	0.33	0.32	0.30	0.22
0.41						0.26	0.11
0.46		0.29		0.29	0.16	0.21	0.014
0.50						0.20	
0.55		0.21		0.21	0.036		
0.59							
0.64		0.015		0.035			
0.68							
0.73							

TABLE 8. THE MEASURED AND THEORETICAL REFLECTIVITIES FOR THE MIRRORS LISTED IN TABLE 4

Mirror	Energy (keV)	Angle of Incidence (arc-min)	R_{Theory}	R_{Total}	R_{LPC}	Difference
Itek FS/Pt	8.01	25	0.76	0.70	0.68	0.02
		39	0.07	0.14	0.11	0.03
	6.4	25	0.80	0.77	0.74	0.03
		39	0.53	0.32	0.32	0
		51	0.09	0.073	0.056	0.017
	2.99	25	0.73	0.75	0.72	0.03
		39	0.58	0.61	0.53	0.08
		51	0.46	0.48	0.42	0.06
PE FS/Au	8.01	25	0.76	0.79	0.80	-0.01
		39	0.07	0.20	0.18	0.02
		51	0.015	0.065	0.051	0.014
	6.4	25	0.80	0.83	0.80	0.03
		39	0.53	0.53	0.50	0.03
		51	0.09	0.11	0.09	0.02
	2.99	25	0.73	0.80	0.79	0.01
		39	0.58	0.68	0.60	0.08
		51	0.46	0.54	0.48	0.06
PE FS/Pt	8.01	25	0.76	0.75	0.72	0.03
		39	0.07	0.13	0.12	0.01
		51	0.015	0.03	0.038	0.008
	6.4	25	0.80	0.78	0.75	0.03
		39	0.53	0.43	0.41	0.02
		51	0.09	0.088	0.066	0.022
	2.99	25	0.73	0.75	0.72	0.03
		39	0.58	0.61	0.51	0.10
		51	0.46	0.48	0.38	0.10
PE Ni-Be/Pt	8.01	25	0.76	0.73	0.72	0.01
		39	0.07	0.15	0.11	0.04
		51	0.015	0.039	0.024	0.015
	6.4	25	0.80	0.76	0.75	0.01
		39	0.53	0.37	0.38	-0.01
		51	0.09	0.08	0.051	0.029
	2.99	25	0.73	0.74	0.72	0.02
		39	0.58	0.59	0.52	0.07
		51	0.46	0.46	0.39	0.07

TABLE 8. (Concluded)

Mirror	Energy (keV)	Angle of Incidence (arc-min)	R_{Theory}	R_{Total}	R_{LPC}	Difference
PE Zer/Ni	8.01	25	0.08	0.33	0.29	0.04
		39	0.007	0.10	0.061	0.039
	6.4	25	0.92	0.90	0.85	0.05
		39	0.07	0.14	0.099	0.041
	2.99	25	0.92	0.92	0.83	0.09
		39	0.86	0.85	0.68	0.17
		51	0.78	0.72	0.59	0.13
Itek Zer/Ni	8.01	25	0.08	0.32	0.28	0.04
		39	0.007	0.079	0.055	0.024
	6.4	25	0.92	0.90	0.86	0.04
		39	0.07	0.15	0.095	0.055
	2.99	25	0.92	0.93	0.84	0.07
		39	0.86	0.87	0.70	0.17
		51	0.78	0.78	0.61	0.17
EK ULE/Ni	8.01	25	0.08	0.32	0.28	0.04
		39	0.007	0.086	0.062	0.024
	6.4	25	0.92	0.89	0.84	0.05
		39	0.07	0.15	0.098	0.052
		51	0.014	0.04	0.047	0.007
	2.99	25	0.92	0.91	0.81	0.10
		39	0.86	0.84	0.67	0.17
		51	0.78	0.71	0.60	0.11

V. X-RAY TESTS WITH THE HIGH-RESOLUTION IMAGER

5.1 The HRI Detector

High resolution imaging experiments were performed with the breadboard of the HRI flown on the HEAO-2 (Einstein) Observatory. The HRI consists of two 25-mm diameter microchannel plates (MCPs) operating in cascade followed by a crossed-grid charge detector as shown in Figure 13. An X-ray incident on the first MCP produces a photoelectron. The subsequent amplification by the second MCP results in a charge cloud of approximately 10^8 electrons. This charge cloud is collected by the cross-grid and subsequently the signal is amplified. The X-Y coordinates of the centroid of the charge cloud are determined to an accuracy of 15 μm primarily determined by the diameter of each microchannel plate element.

The digital X-Y coordinates of each X-ray event are transmitted to a minicomputer for image display and storage. It is possible to view the buildup of the image in real time photon by photon. The 15 μm resolution of the detector corresponds to an angle of 0.02 arc-sec at the mirror test assembly. The quantum efficiency of the detector is about 10 percent at 1.5 keV (8 Å) and falls to below 5 percent at energies greater than 3 keV. This efficiency is also dependent on the angle of incidence as shown in Figure 14.

5.2 Diffraction Effects

Even though the incident radiation is of relatively short wavelength, diffraction does play a role in the measurements. λ/w, where w is the slit width, is between 0.1 and 3 arc-sec for X-ray wavelengths between 1.5 Å (CuKα) and 44.7 Å (CKα). Figure 15 is a composite of calculated diffraction patterns over the wavelength ranges used in these experiments. Figure 16 is a comparison of an experimentally measured slit profile with the calculated profile. The agreement is excellent.

5.3 Data Analysis Theory

First-order vector perturbation theory [4] provides the link between X-ray measurements and the topography of the optical flats. The angular distribution of the radiation diffusely reflected (or scattered) by a rough surface (but with $[(2\pi/\lambda)\ \sigma \sin \theta_i]^2 << 1$, where σ is the rms surface height and θ_i is the grazing angle of incidence) is given by

$$\frac{1}{I_i}\left(\frac{dI}{d\Omega}\right)_s = \frac{16\pi^4}{\lambda^4} \sin \theta_i \sin^2 \theta_s\ Q\ W(p,q)$$

where I_i is the incident intensity, θ_s is the direction of the scattered radiation, Q is a quantity analogous to the Fresnel reflection coefficient of the surface (in the limit of small scattering angles it becomes the Fresnel intensity reflection coefficient of a perfectly smooth interface of the surface material), and W(p,q) is the power spectral density of the surface (PSD).

The physical interpretation of the theory is as follows: scattering into a given direction is the result of diffraction by a single spatial wavelength component (surface wavelength) of the surface. The full angular distribution of the scattering is then directly related to the amplitude distribution of surface wavelengths which is the PSD of the surface.

In one dimension, the relationship between surface wavelength d, angle of incidence θ_i, angle of scattering $\theta = (\theta_s - \theta_i)$, and incident wavelength λ is given by the grating equation:

$$\lambda = d\,|\cos\,\theta_s - \cos\,\theta_i\,|$$

which for small angles is

$$\lambda = d\;\theta_i\,|\theta_s - \theta_i\,| = d\;\theta_i\;|\theta| \quad .$$

Figure 17a illustrates this relationship for a range of incident and scattering angles. The region within the trapezoid is the restricted range of parameters for the X-ray wavelength using the HRI.

The range of surface wavelengths probed by the measurements reported here is between about 0.4 mm and 60 mm which is commonly in the range of "figure" errors rather than as surface microroughness. The position sensitive proportional counter with its greater angular coverage and higher energy response is capable of probing surface wavelengths down to the few micron range.

By means of Fourier theorems it is possible to relate the rms surface height to the integral of the distribution of the diffusely reflected radiation

$$\sigma^2 = \left(\frac{\lambda}{4\pi\theta_i}\right)^2 \int \frac{I}{I_R}\left(\frac{dI}{d\Omega}\right)_s d\Omega$$

where I_R is the specularly reflected intensity. $\int 1/I_R\,(dI/d\Omega)_s\,d\Omega$ is referred to as total integrated scatter (TIS). Figure 17b shows the variation of TIS with wavelength for rms surface heights of 10 and 20 Å and for grazing angles of 0.5 and 1.0 deg. This figure is useful for estimating the total radiation diffusely reflected by a rough surface but must be used with caution in interpreting bandwidth limited measurements, i.e., measurements that are restricted in surface wavelength range.

5.4 Results

Figure 17c is an example of a typical two-dimensional image of the slit obtained after initial processing. The faint elliptical image in the upper right-hand corner is a local "hot spot" in the HRI and is treated as background in further processing. Figures 17d and 17e are examples of one-dimensional projections of the reflected slit images. The horizontal scale is the pixel number (HRI images consist of 4096 x 4096 arrays). Figure 17f is the integral of a one-dimensional projection plotted as a function of the

angle from the centroid. The integral has been normalized by dividing it by the integral of the unreflected slit image.

As has been discussed in the previous section, the HRI measurements, because of their restricted angular range of 14 arc-sec, probe surface wavelengths on the 0.4 to 60 mm range and are not sensitive to microroughness. Thus, they are more suitable for determining figure errors, whether produced in the manufacturing process or due to distortions caused by holding fixtures. These measurements have been instrumental in revealing large, out of tolerance, slope errors in a number of test flats that were not revealed by the vendors' test procedures or by the initial examination of Twyman-Green interferograms made at MSFC, but are not able to measure high spatial frequency surface roughness which leads to wide angle X-ray scattering. Further results of the HRI measurements can be found in Reference 15.

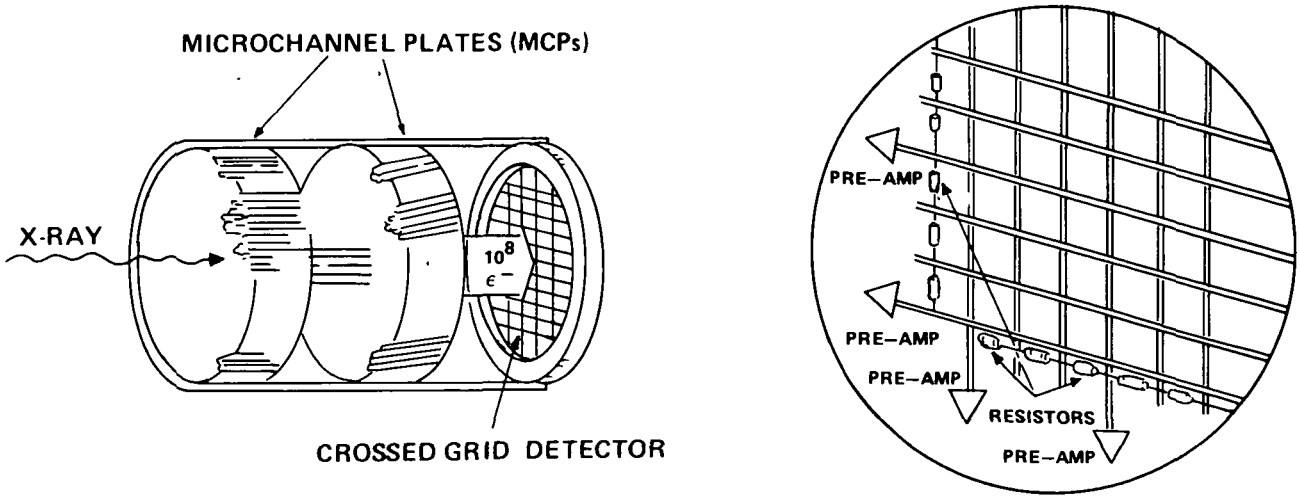

Figure 13. Schematic diagram of the High-Resolution Imager (HRI).

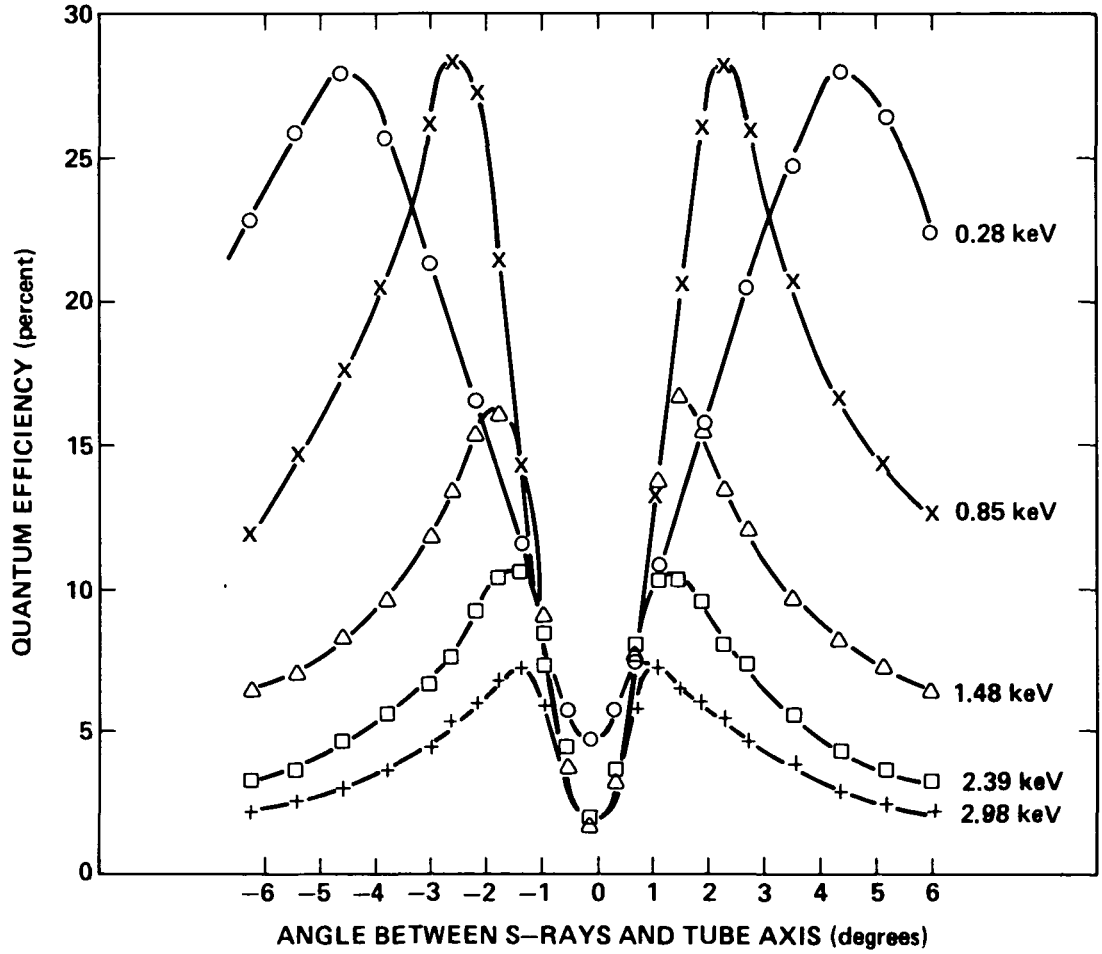

Figure 14. Quantum efficiency (counts per photon) of MgF_2-coated MCPs as a function of angle and X-ray energy.

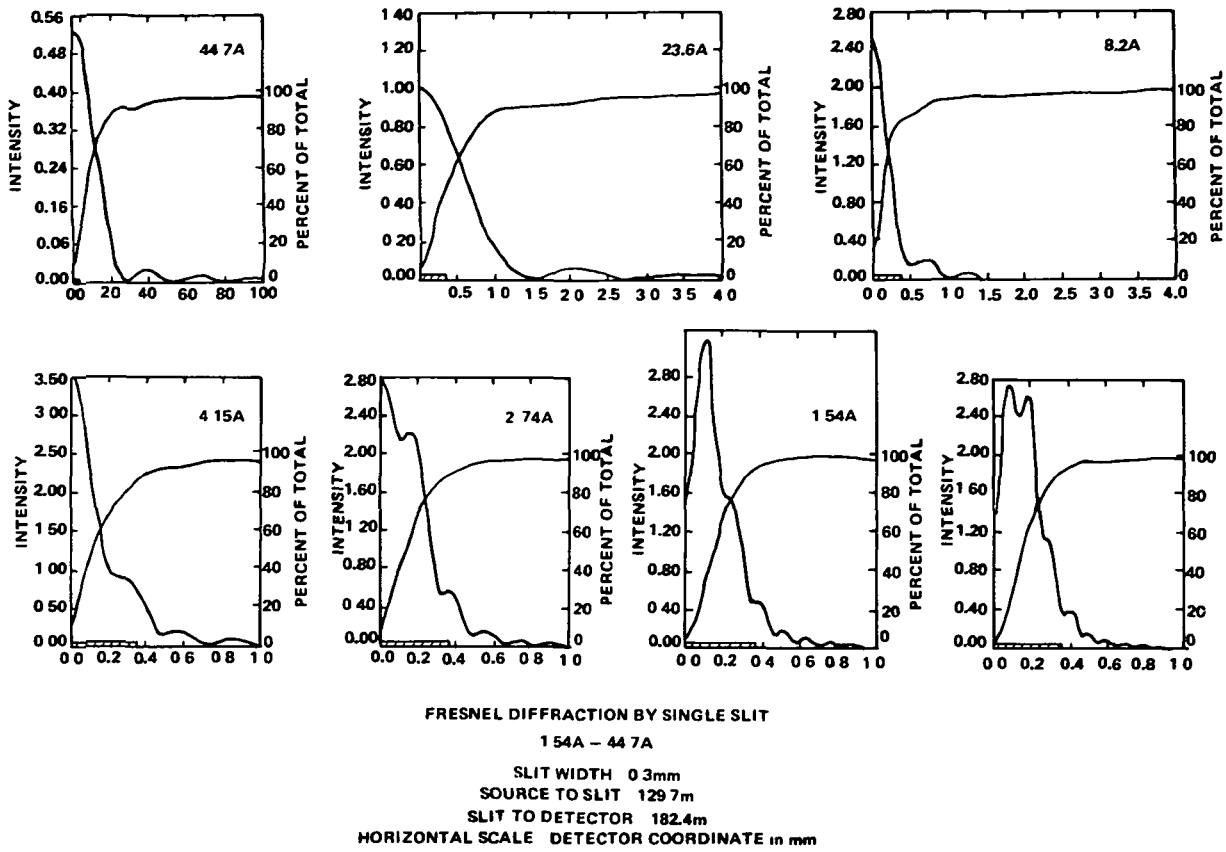

Figure 15. Calculated single slit diffraction patterns for the experimental geometry at MSFC and for wavelengths between 44.7 Å and 1.54 Å. The geometrical boundary of the slit is at 0.36 mm and is shown cross-hatched. 1 mm in the plane of the detector subtends an angle of 1.1 arc-sec at the flats fixture.

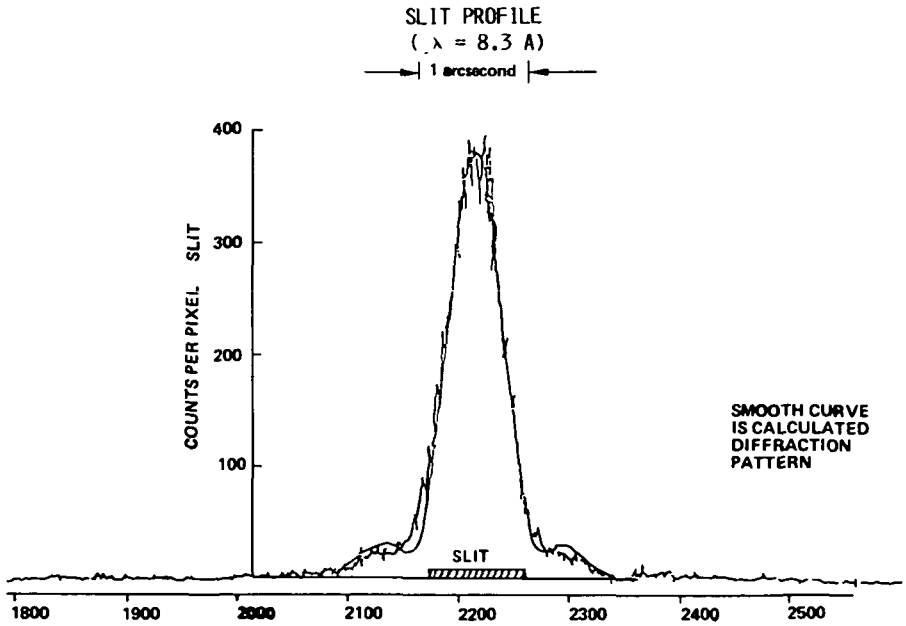

Figure 16. Profile of the direct beam for 8.3 Å X-rays at the MSFC facility. The smooth curve is the calculated Fresnel diffraction pattern. The horizontal scale is in detector pixels. One pixel is 0.01 arc-sec wide and contains all the counts along the length of the slit at the pixel location.

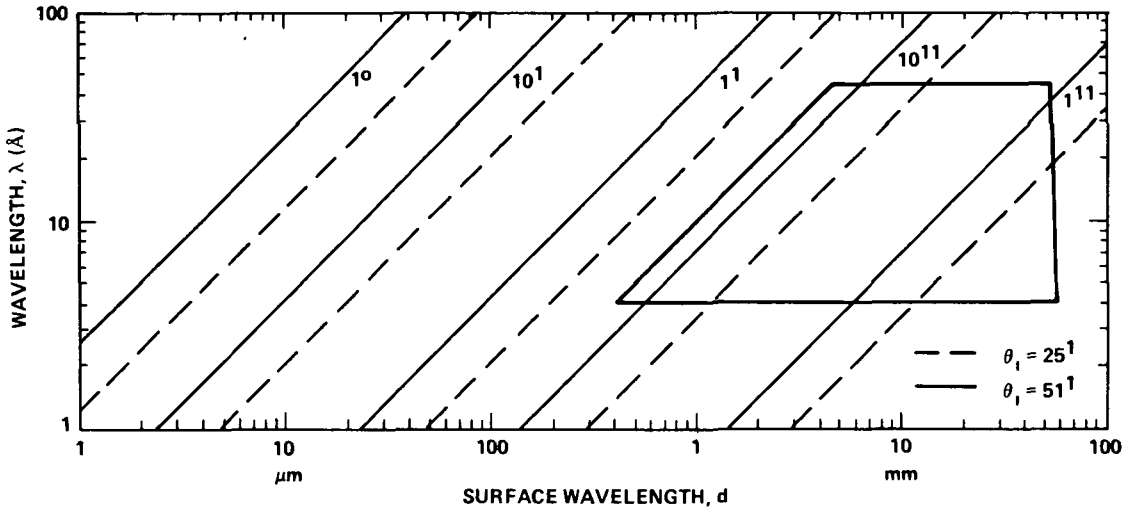

Figure 17a. The surface wavelengths relevant to X-ray small-angle scattering.

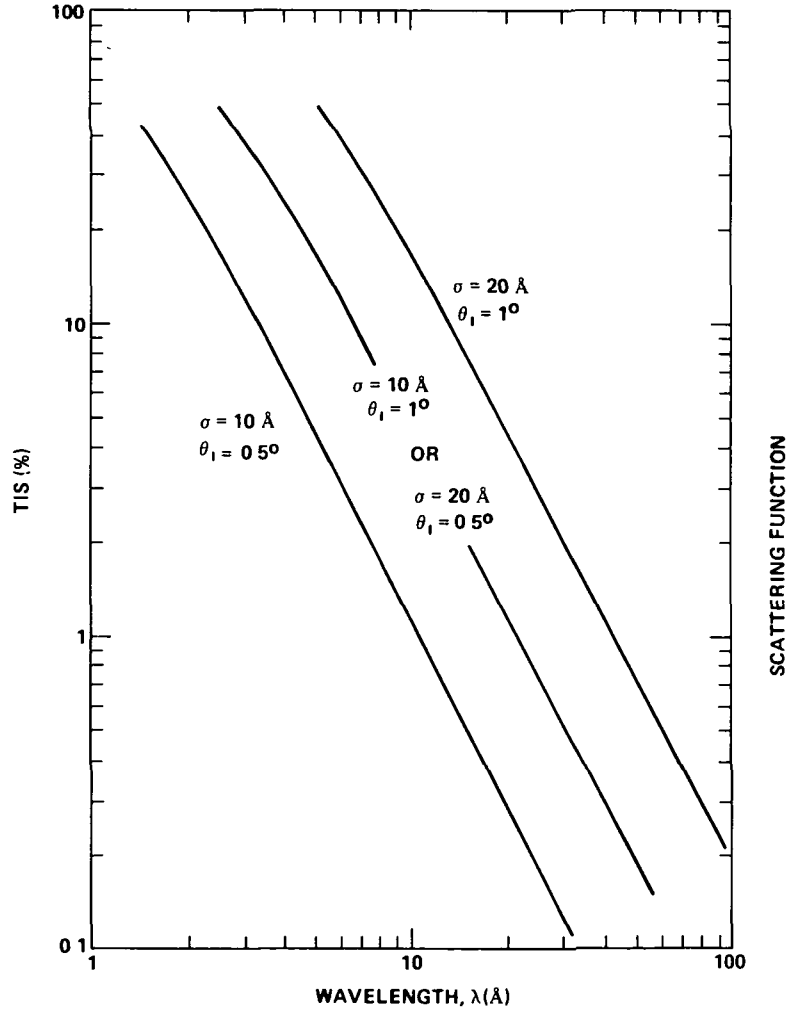

Figure 17b. The wavelength dependence of X-ray scattering.

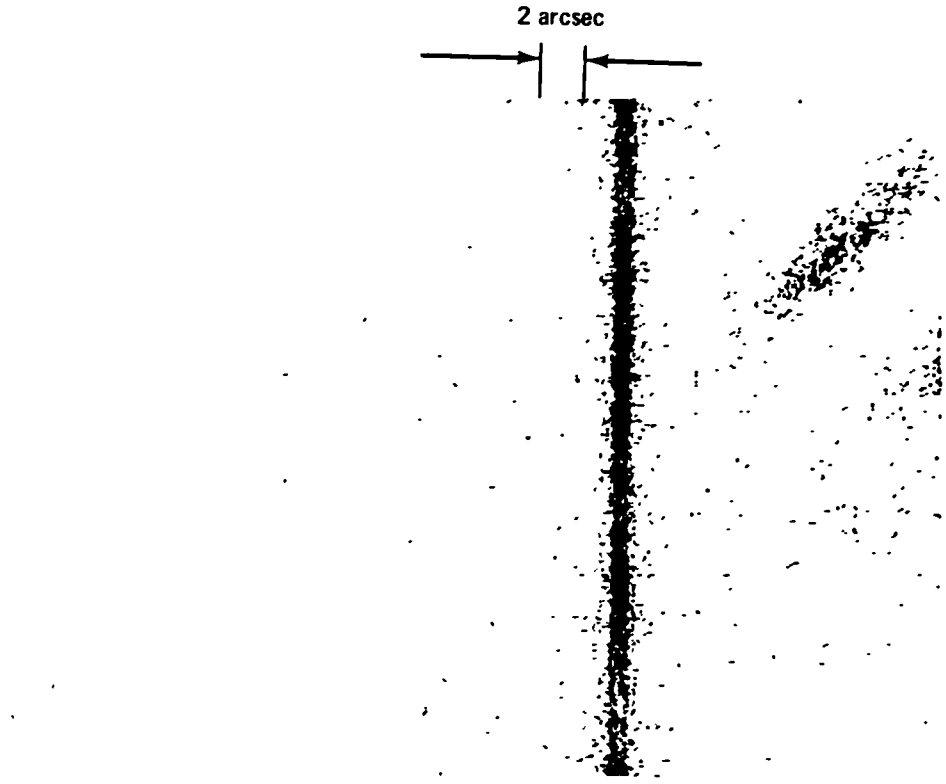

Figure 17c. A two-dimensional image (at 8.3 Å) of the slit using the HRI. The elliptically shaped feature in the upper right-hand corner is a local "hot spot" in the detector caused by contamination on the MCP surface.

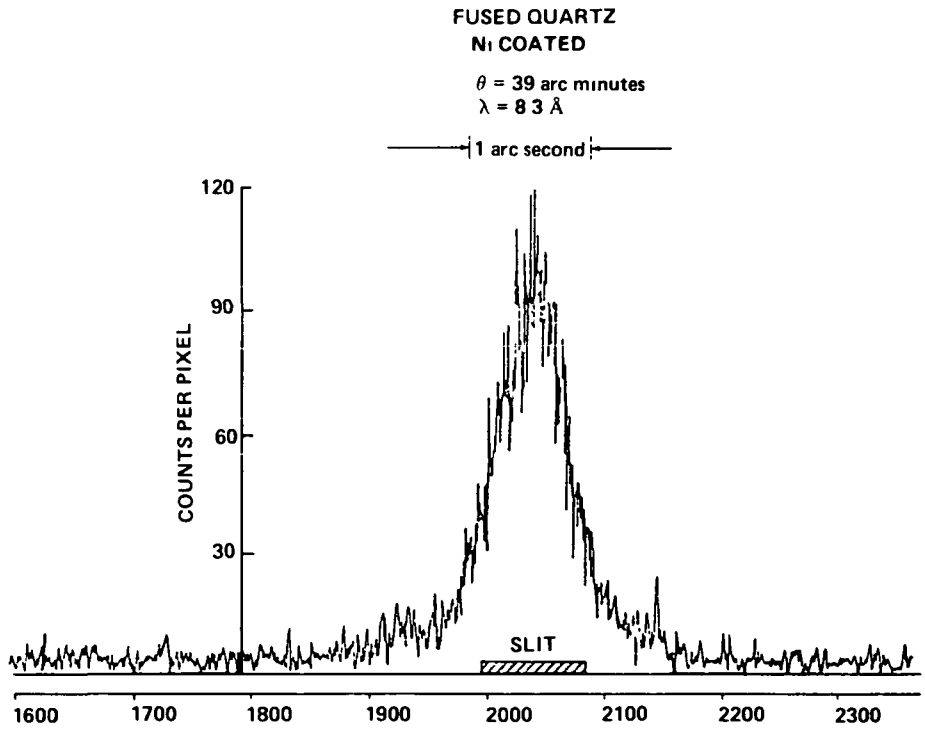

Figure 17d. Scattering distribution for 8.3 Å X-rays reflected by a pair of nickel-coated fused-quartz flats.

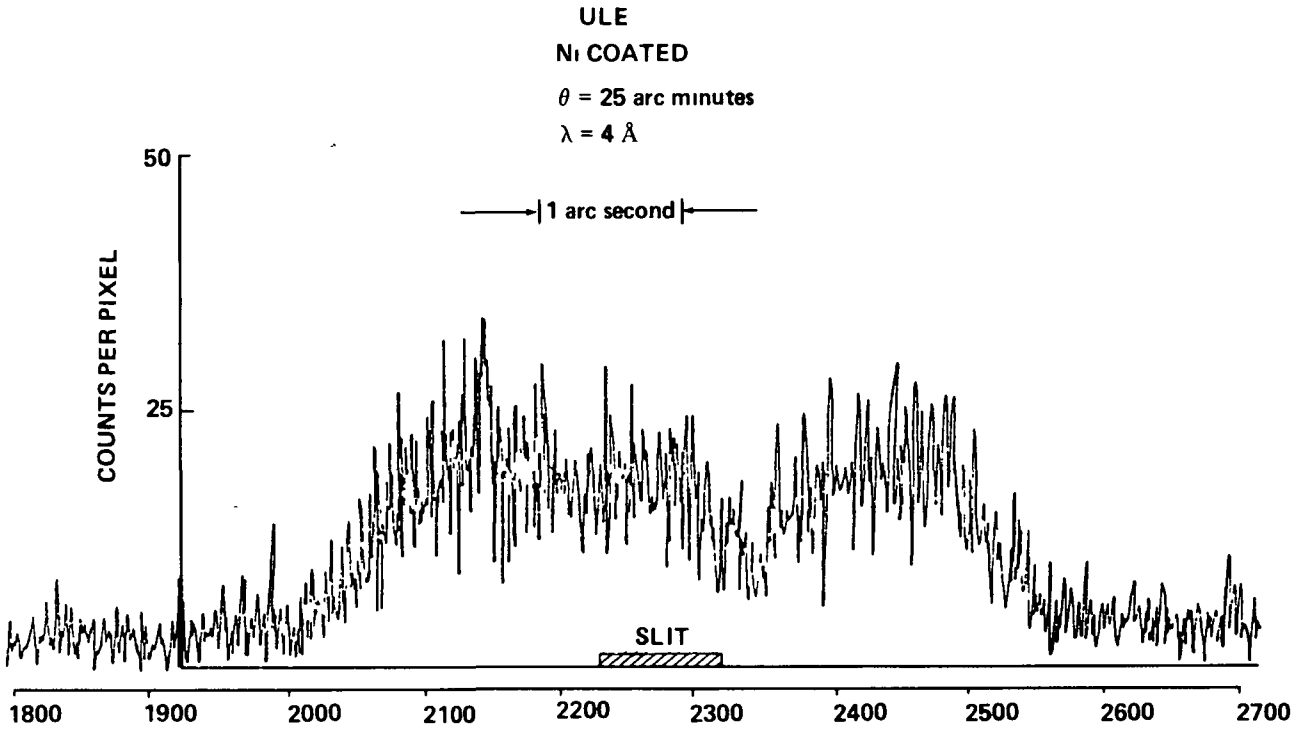

Figure 17e. Scattering distribution for 4 Å X-rays reflected by a pair of nickel-coated ULE flats.

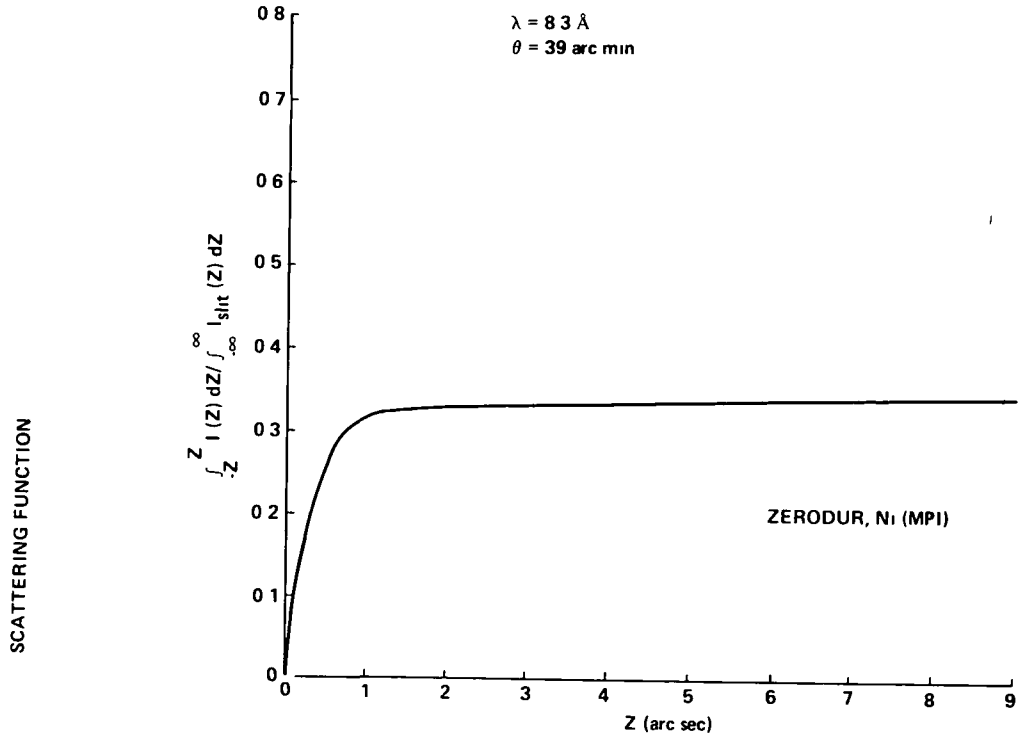

Figure 17f. Integrated scattering distribution for λ = 8.3 Å and a grazing angle of 39 arc-min; nickel-coated Zerodur.

VI. X-RAY TESTS AT MAX PLANCK INSTITUTE

6.1 X-Ray Test Facility

We have achieved arc-second X-ray scattering measurements by employing mechanical collimation to reduce the divergence angle of the X-ray beam and a high resolution photon counting detector to detect the scattered X-rays.

The X-ray test facility at the Max Planck Institute for Extraterrestrial Physics, designed and built to test and calibrate telescopes for X-ray astronomy, was used for the measurements reported here. This facility (Fig. 18) consists of a 130 m vacuum pipe, microfocus X-ray generator, instrument chamber, and control room. Equipment particular to the scattering measurements consists of a mirror fixture, slit assembly, and a one-dimensional position sensitive detector.

The X-ray generator produces a focused beam of electrons on a target anode. The emitted X-rays consist of the K and L radiation characteristic of the anode material and a bremsstrahlung continuum, which is suppressed by filters. The generator is capable of producing line emission over the range 0.1 keV (Be Kα) to 8 keV (Cu Kα) with flux density levels at the instrument chamber of up to 10^4 photons $cm^{-2}s^{-1}$.

The flat mirrors under test were held in a fixture located 105 m from the X-ray source and 25 m from the detector. A periscope geometry was chosen because a single reflection geometry would produce reflected beam excursions too large to be accommodated by the pipe. However, at a grazing angle of incidence of 23 arc-min it was possible to test the forward mirror(s) alone. By means of remote manipulators it was possible to align and verify alignment using optical autocollimation techniques and the X-ray beam itself. With these techniques it was possible to set the mirrors parallel to each other to within 10 arc-sec; the grazing angle could be set to better than 0.05 arc-min, the first mirror(s) and the slit could be set better than 10 arc-sec and 1 arc-min, respectively, to the horizontal plane, and the detector axis could be set parallel to the horizontal plane to within 1 arc-min.

The one-dimensional position sensitive detector is a commercial gas flow detector manufactured by M. Braun, Inc. (Garching, West Germany). The gas fill is P10 (Argon-Methane) at a pressure of 8 atmospheres. The effective length of the detector is 48 mm which subtends an angle of 6.5 arc-min at the mirror fixture. The effective width is 4 mm which means that a 5 mm wide strip on the mirrors was illuminated by X-rays. Position sensing is achieved by the pulse rise time method of Borkowski and Kopp. The detector resolution is about 100 μm (1 arc-sec FWHM) and the linearity is better than 0.1 percent. The non-uniformity of response of the detector over the central 40 mm of the detector was less than 5 percent. The position spectrum of incident photons were collected in 1024 channels (47 μm/channel: 0.4 arc-sec/channel) of a pulse height analyzer.

The slit width was 150 μm. The geometrical projection of this slit at the detector is 190 μm (1.6 arc-sec). Fresnel diffraction, discussed in a later section, broadens the slit image slightly.

A gas proportional counter was used to monitor the X-ray beam during an experimental run.

6.2 Description of the Optical Flats Used

Six pairs of optical flats were tested. (A total of 35 pairs was fabricated for this program and the majority are being tested at the Marshall Space Flight Center Facility.) The manufacturing specifications for the flats are shown in Table 9 and Table 10 describes the flats that were tested. The surface topography of the flats have been characterized using optical and mechanical methods.

6.3 Experimental Procedure

The flats were tested at the following grazing angles: 23, 39, and 51 arc-min which are similar to the grazing angles of the AXAF mirrors and at 1.5 keV (Al Kα) and 6.4 (Fe Kα) with one pair measured at 4.5 keV (Ti Kα) and 8.1 keV (Cu Kα), also. At each energy a position spectrum was determined for the direct beam (flats removed from the X-ray path) in order to determine the overall system resolution, and at the three grazing angles (single and double reflection for 23 arc-min) with the flats intercepting the beam. A typical run accumulated about 100,000 counts in the position spectrum and took between 15 min and 1 hr, depending upon the surface coating, incident angle, and energy. The background count rate never exceeded 5×10^{-5} cts channel^{-1}s^{-1} and was therefore negligible.

6.4 Experimental Results

Figure 19 shows the position spectrum for the direct beam for an energy of 1.5 keV (8.3 Å). The position spectrum is displayed on a logarithmic count scale and the integral of the spectrum normalized to the total counts accumulated (within ±3.2 arc-min of the specular beam) is displayed on a linear scale. At 30 arc-sec from the specular direction the counts per channel drop over a factor of 1,000 from that at the peak and the integral rises to 0.90 and 0.99 at 2 and 15 arc-sec, respectively. Figures 20 and 21 show the same data displayed at higher resolution. The FWHM of the direct beam is seen to be 2.6 arc-sec. Fresnel diffraction calculations (Fig. 22) show that the FWHM of the image of the slit illuminated by a point source for the geometry of the experiment should be 1.0 arc-sec. Since the detector contributes about 0.8 arc-sec to the width, this implies that the source contributes about 2.3 arc-sec. If the source spot size were about 1.5 mm in diameter, it would contribute this amount. Discoloration of the source anode is consistent with the source of this size. Reduction of the source size in future experiments would improve the resolution by a factor of 2.

Figures 23 through 25 show scattering data for 1.5 keV X-rays incident upon a pair of platinum coated fused silica flats at 39 arc-min grazing angle. A slight enhancement in the counts outside the central core of the reflected beam profile shown in Figure 23 can be seen. From Figure 25 we see that about 10 percent of the total counts are outside 3.5 arc-sec. The FWHM of the beam profile is equal to the direct beam within experimental uncertainty implying that the figure tolerances were met for the flats.

Figures 26 through 30 show similar data for another pair of platinum coated fused silica flats. The FWHM is 11.6 arc-sec. One or both of the flats has a large figure error. When we examine Figure 29 which is the beam profile for X-rays reflected by the front mirror only, we see that the FWHM is about 4 arc-sec. Hence, the second mirror possesses the large figure error.

Reference 16 contains a complete set of the experimental results along with a more extensive discussion of the analysis.

6.5 Discussion of the Results

All the six pairs of mirrors tested have shown a rapid rise in the integrated profiles to a plateau, implying that very few photons are scattered outside the ±3.2 arc-min range of the detector and that the integrals can be considered as normalized to the total number of photons reflected, not just to those within the angular range of the detector. As a comparison, Figure 21 shows the position spectrum for a pair of laboratory mirrors which were figured very well but not highly polished. The scattering is obvious and the integral is still rising as we reach the extreme angular range of the detector.

That we are collecting most of the photons reflected is further supported by comparing the number detected by that predicted from the calculated reflectivity.

We define the measured reflectivity by:

$$R_{meas} = (I_\theta M_o / I_o M_\theta)^{\frac{1}{2}} \tag{17}$$

where

I_θ = total number of counts in the position spectrum (within ±3.2 arc-min) for grazing angle θ

I_o = total number of counts in the position spectrum (within ±3.2 arc-min) for the beam passing through the slit but not reflected

M_θ, M_o = the monitor counts for the reflected and direct beam runs.

Table 11 shows that within the experimental uncertainties R_{meas} equals that calculated from the published optical constants (Fig. 31).

Table 11 also gives a summary of the results of all the measurements. The FWHM and the angular distances from the specular beam which contain 50 percent and 90 percent of the reflected photons are given. Where available, the determination of the rms surface height from optical or mechanical methods is also given for each flat. With three notable exceptions (the two long Itek flats, and the one long Eastman Kodak flat) the flats appear to be figured close to the specified tolerances. Scattering at all energies appears to be at the few percent level which is consistent with the measured rms surface heights. For example, at a grazing angle of 23 arc-min and an incident energy of 6.4 keV, a surface with σ = 5 Å has a total integrated scatter TIS = 0.05.

In order to obtain a quantitative measure of the scattering and to separate the effect of long period slope error from high frequency surface height deviations, we have related the fraction of photons scattered outside an angle θ to a band-limited rms surface height. Through the grating equation we can associate an upper bound d_{max} for the spatial wavelengths contributing to the scattering of these photons:

$$d_{max} = \lambda / \theta_i \theta$$

Then

$$\sigma = f^{\frac{1}{2}} \lambda/4\pi \sin \theta_i \quad ,$$

for $d < d_{max}$, where f is given by $f = N(>\theta)/N$, $N(>\theta)$ is the number of photons detected in the angular range θ to 3.2 arc-min, and N is the total number of photons detected over the angular range 0 to 3.2 arc-min.

We have assumed in the above, that a negligible number of photons are scattered at angles beyond the maximum angular range of the experiment. This assumption is consistent with the data, as we have shown.

Table 12 shows the results of these calculations for the single reflection (θ_i = 23 arc-min) experimental runs. The angle θ was chosen for d_{max}'s of 200 and 500 μm in order to be able to relate the σ's to those obtained by non-X-ray methods. From the table we see that the scattering is at the 1 percent level or less for all the flats for minimum scattering angles corresponding to spatial wavelengths less than 500 μm. The calculated σ's are at the few Angstrom level which is consistent with the non-X-ray data. Curiously, significantly higher σ's are found for the 8.3 Å data for d_{max} = 500 μm. This may mean that for this spatial wavelength range non-random figure errors contribute the most to the value of f and σ has no statistical meaning.

6.6 Conclusions

From these results and work at the Marshall Space Flight Center it appears that all the glassy substrates, Zerodur, fused quartz, fused silica, ULE, and Cervit, can be polished to levels well beyond the original goals of the AXAF. It remains to be seen whether or not the figure requirements can be met while simultaneously keeping the surface super smooth.

In order to develop models for predicting scattering and to correlate scattering with surface characterization methods we need to obtain a graded set of flats. The flats so far tested have been too smooth for these purposes. Under the AXAF program a number of flats will be fabricated which will have a range of roughnesses. Since we will not have the luxury of testing the imaging capabilities of the flight mirrors before final assembly, the ability to predict the X-ray scattering from non-X-ray measurement techniques will be very important.

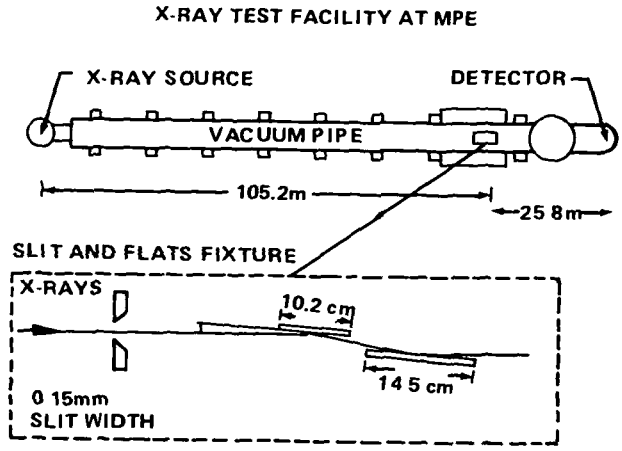

Figure 18. Schematic of the X-ray test facility of the Max Planck Institute for Extraterrestrial Physics.

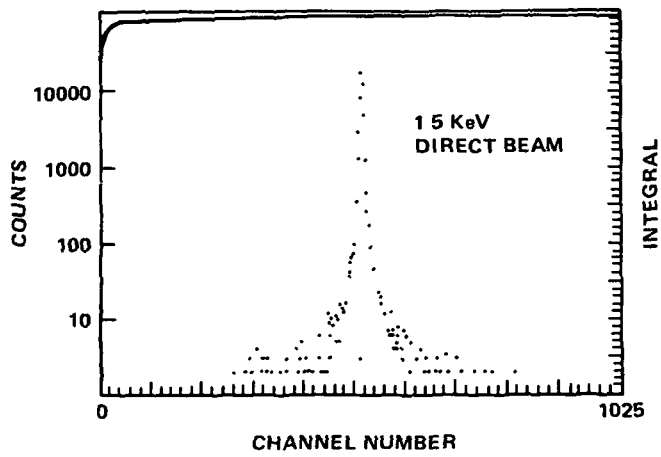

Figure 19. The spectrum of the direct beam for 1.5 keV X-rays at the Max Planck facility. The integral of the position spectrum folded about the specular direction is also shown. Each channel (0 to 1023) is equivalent to 47 μm (0.38 arc-sec).

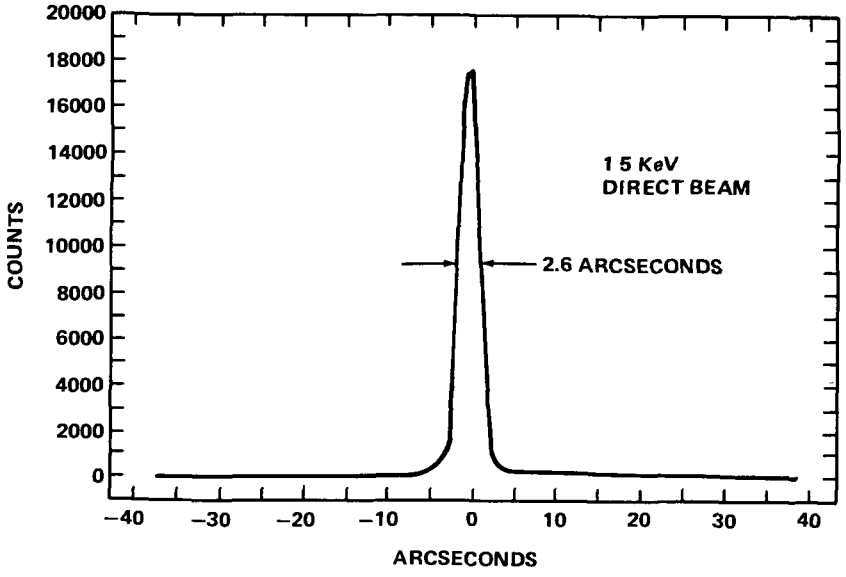

Figure 20. The position spectrum of Figure 19 displayed with higher resolution and on a linear scale.

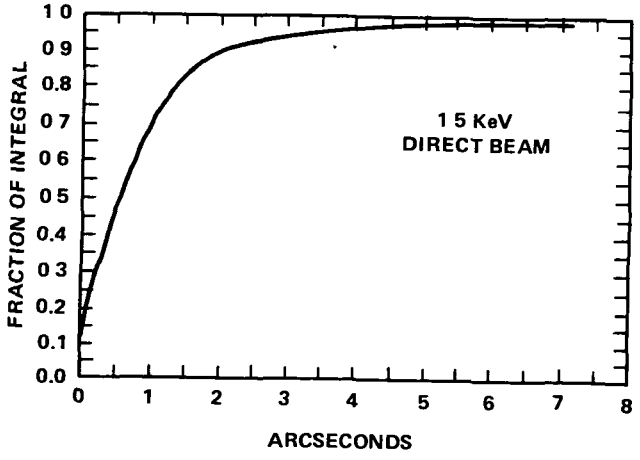

Figure 21. The integral of Figure 19 displayed with higher resolution.

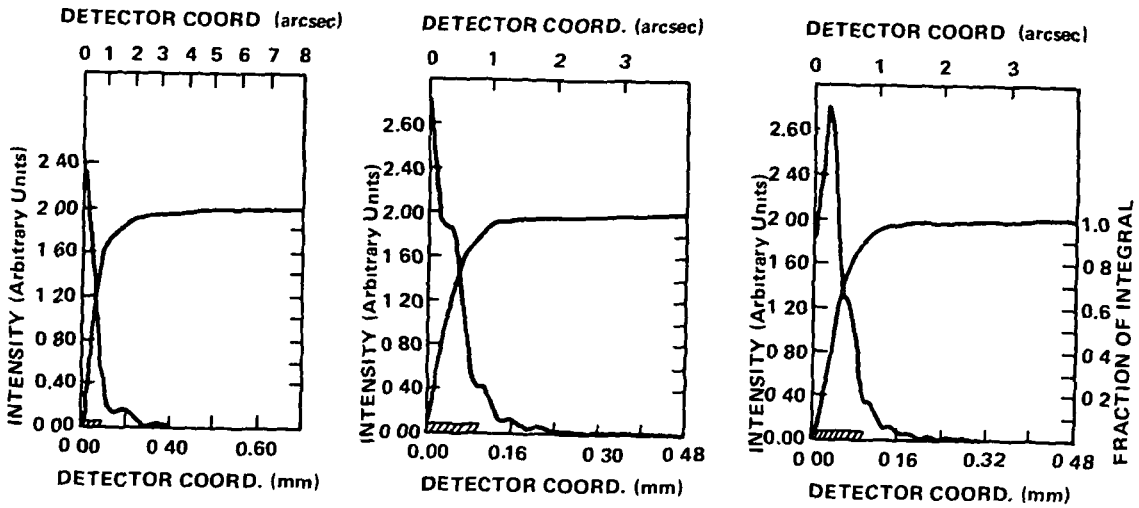

Figure 22. Calculated single slit diffraction patterns for the experimental geometry at Max Planck and for the incident energies: 1.39, 4.5, and 6.4 keV. The geometric projection of the slit is shown at the cross-hatched rectangle and its boundary is at 0.09 mm (0.75 arc-sec).

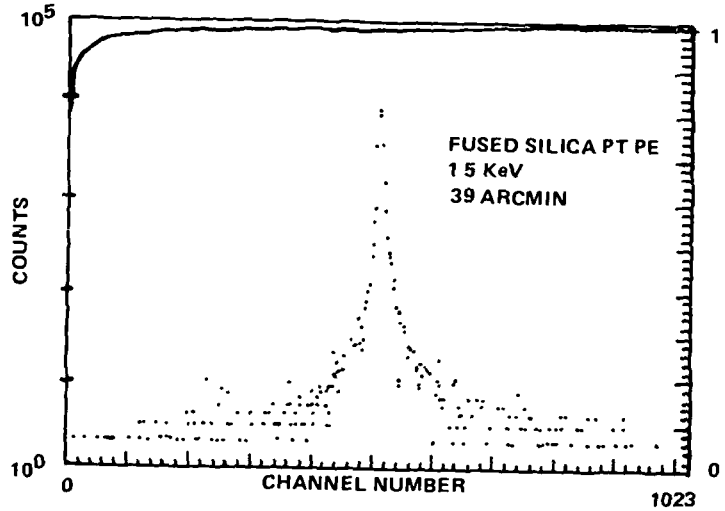

Figure 23. The position spectrum for 1.5 keV X-rays reflected by the platinum coated fused silica mirrors at Max Planck. The grazing angle of incidence is 39 arc-min. The integral is also shown. The scale is the same as in Figure 19.

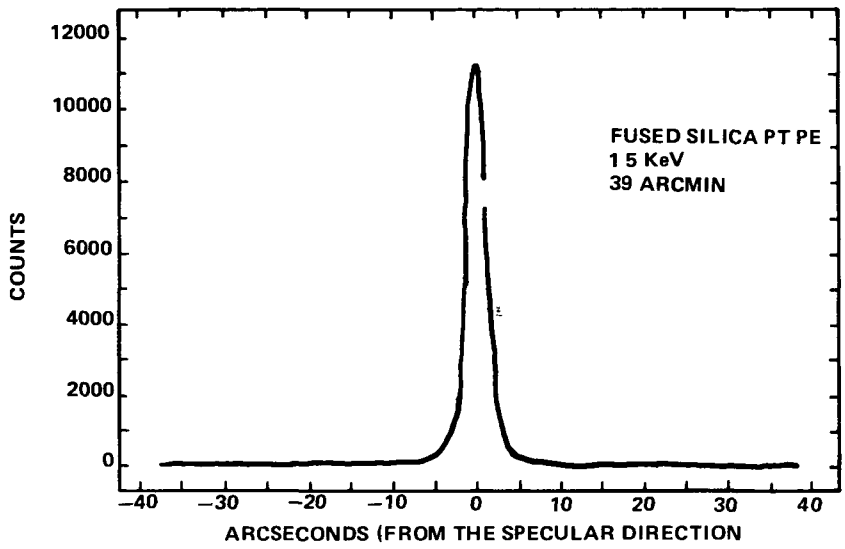

Figure 24. The position spectrum of Figure 23 displayed with higher resolution.

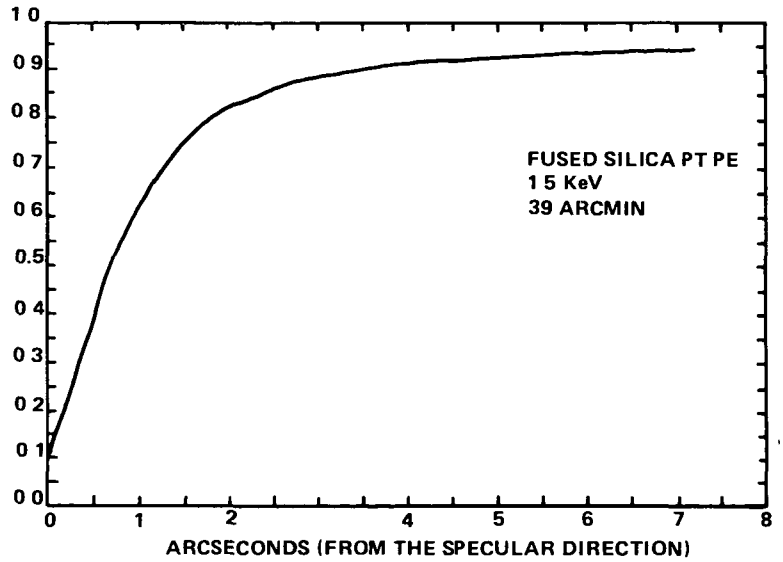

Figure 25. The integral of Figure 23 displayed with higher resolution.

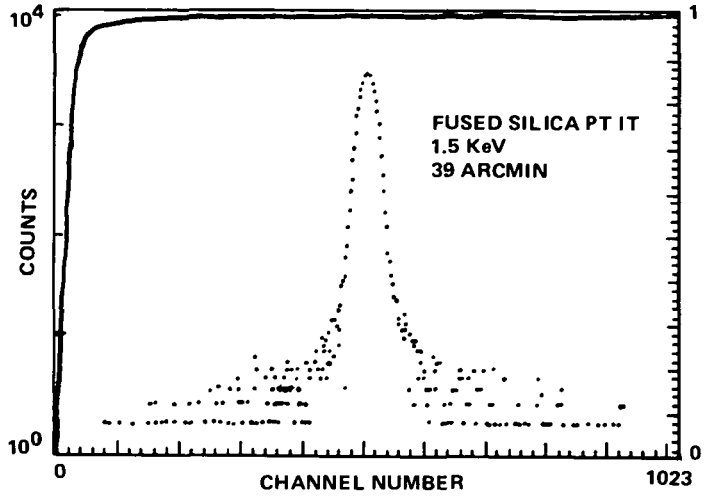

Figure 26. The position spectrum for 1.5 keV X-rays reflected by a pair of platinum coated fused silica mirrors at Max Planck. The grazing angle of incidence is 39 arc-min. The integral is also shown.

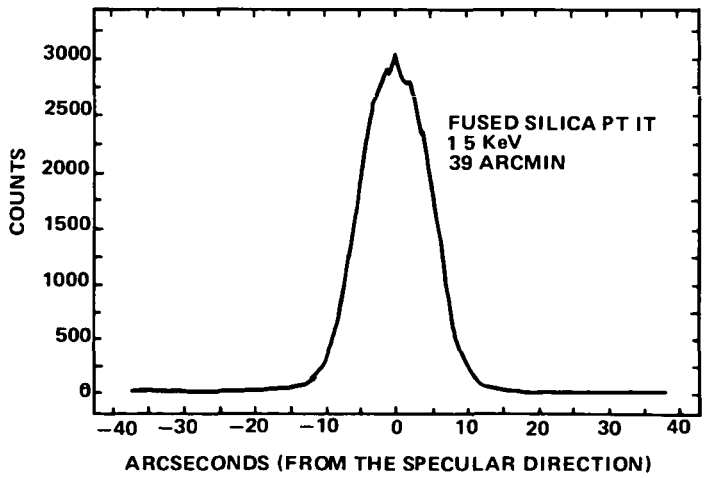

Figure 27. The position spectrum of Figure 26 displayed with higher resolution.

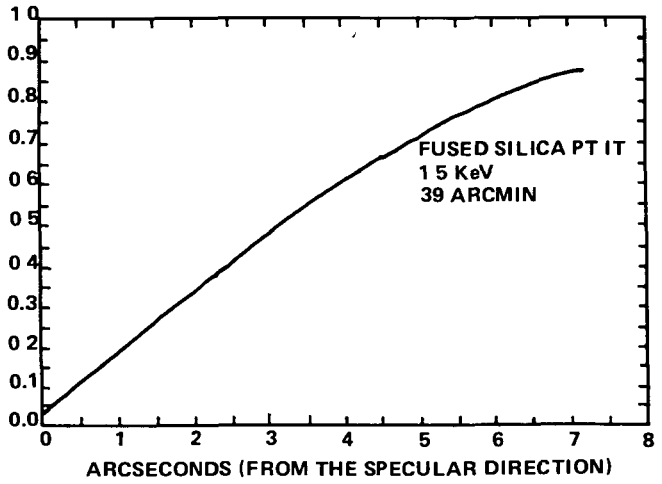

Figure 28. The integral of Figure 26 displayed with higher resolution.

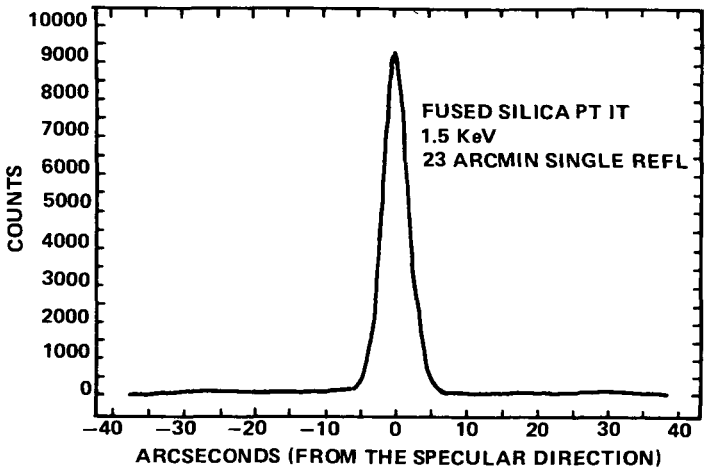

Figure 29. The position spectrum for 1.5 keV X-rays reflected by a single platinum coated fused silica mirror at Max Planck. The grazing angle of incidence is 23 arc-min.

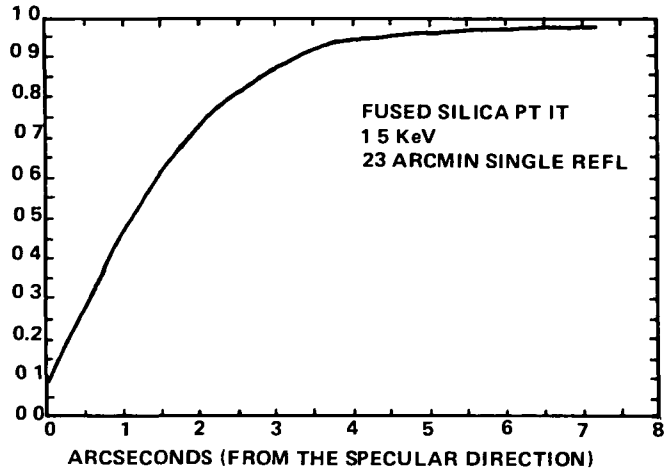

Figure 30. The integral of the position spectrum of Figure 29.

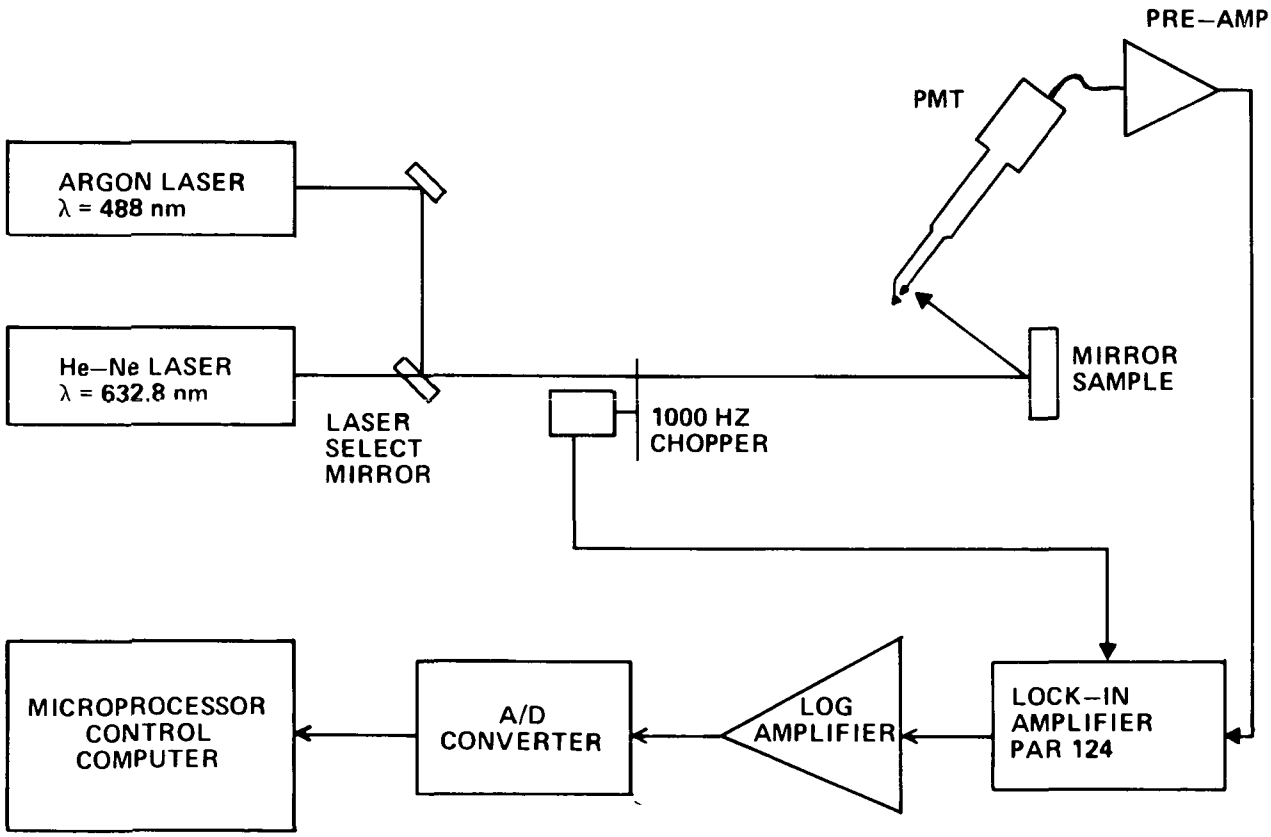

Figure 31. A system block diagram of the MSFC BRDF scatterometer.

TABLE 9. MANUFACTURING SPECIFICATIONS FOR THE FLATS

Length: 4 and 6.5 in.
Width: 1.25 in.
Thickness: 1.0 in.
Flatness: $\lambda/20$ rms at λ = 6328 Å
Local Slope: 0.5 microradian (mm to cm spatial wavelength range)
Surface Roughness: <25 Å rms with a goal of 10 Å rms.
Figure and Surface Tolerances: To within 2.0 mm of each edge.

TABLE 10. LIST OF FLATS TESTED AT MAX PLANCK INSTITUTE

Substrate	Polishing Method	Coating	Vendor	Test Parameters	
				Grazing Angle (arc-min)	Energy (keV)
Fused Silica	Bowl feed	Platinum	Perkin Elmer	23, 39, 51	6.4, 8.1
Fused Silica	Bowl feed	Platinum	Itek	23, 39, 51, 90	1.5
Zerodur	Bowl feed	Nickel	Itek	23, 39, 51	1.5, 6.4
Fused Quartz	Plano Polisher	Platinum	Eastman Kodak	23, 39, 51	1.5, 6.4
Fused Silica	Bowl feed	Gold	Perkin Elmer	23, 39, 51	1.5, 6.4

TABLE 11. SUMMARY OF MAX PLANCK SCATTERING RESULTS

Flat Description	E (keV)	θ (arc-min)	FWHM*** (arc-sec)	50% (arc-sec)	90% (arc-sec)	$R^{*}_{meas.}$	R_{theo}	TIS (S) (L)	Talystep (S) (L)
Fused Silica Pt PE	1.5	0	2 6	±0 6	±2 1			5 8,3.9	---, 3 7
		23s *	2 6	0 6	2.6	0.87	0.90		
		23	2.8	0 8	4.4	0.89	0.90		
		39	2 7	0.7	3.5	0.86	0 84		
		51	2.9	0 8	3.5	0 81	0.79		
	4.5	0	2 5	0 6	1.8				
		23s	2 8	0 7	2.4	0.83	0.81		
		23	2.5	0.7	3.0	0.83	0 81		
		39	2.6	0.7	2.8	0 64	0.64		
		51	2.8	0 8	2.9	0 48	0.43		
	6 4	0	2 0	0.5	1.9				
		23s.	1.9	0.5	2.5	0.82	0 82		
		23	2 2	0 6	3.0	0.81	0.82		
	8.1	0	3.6	0.9	3.0				
		23s.	4 7	1 2	3.9	----	0.82		
Fused Silica Pt Itek	1.5	0	3 1	±0.8	±2.5			2.2	1.7
		23s.	4.2	1.1	3.4	0.94	0.90		
		23	19 9	5.5	13.5	0.90	0.90		
		39	11.6	3.2	8.0	0.85	0.84		
		51	9.1	2.5	6 7	0.80	0.79		
		90	6 4	1.8	5.3	0.62	0.62		
Zerodur Ni Itek	1.5	0	2.8	±0.7	±2.4			3 3	3 9
		23s.	2 7	0.7	2.6	0.88	0.89		
		23	16.5	4 6	10.1	0.90	0 89		
		39	5 8	2 3	7.2	0.82	0 81		
		51	6 7	2.2	6.8	0.76	0.75		
	6 4	0	3.0	---	---				
		23s.	3.2	---	---	0.88	0.93		
Zerodur Ni PE	1.5	0	3.0	±0.8	±2.4			5.9,3 9	---, 3.6
		23s.	2.9	0.7	2.6	0.91	0.89		
		23	3.5	1 0	4.1	0.89	0.89		
		39	3.4	0.9	3 6	0.82	0.81		
		51	3.5	0.9	3.2	0 77	0.75		
	6 4	0	3 4	0.9	2.6				
		23s.	4.1	1.1	3.2	0.90	0.93		
		23	3.9	1.1	3.9	0.91	0 93		
Fused Quartz Pt EK	1 5	0	4.3	±1.2	±3.4				
		23s.	5.1	1.4	4.0	0.90	0.90		
		23	7.4	2 1	5.7	0.91	0.90		
		39	6 4	1.8	4.9	0.86	0.84		
		51	5.6	1.6	4 7	0.82	0.79		
	6 4	0	3.2	0.8	2.4				
		23s.	4.8	1.3	3.7	0.81	0.82		
		23	6.6	1.7	4 8	0.78	0.82		
Fused Silica Au PE	1.5	0	3.0	±0.7	±2.4			9.7,7 7	---,3.7
		23s.	2.8	0.7	2.6	0 89	0 90		
		23	2 8	0.8	3.6	0.90	0.90		
		39	3.0	0.8	3.2	0.86	0.84		
		51	3.2	0.9	3 1	0.82	0 79		
	6.4	0	3.5	0.9	2.6				
		23s.	3 2	0.9	2.9	0.80			
		23	3.9	1.1	3 5	0.82	0.82		
		39	4.0	1.1	3.4	0.45	0.53		
Fresnel diffraction by the slit	1.5		1.0	±0.2	±1.3				
	4 5		1.0	0.3	0 9				
	6.4		0.9	0.4	0.8				

*Single reflection, short flat
**Uncertainty 1 to 3 percent
***Det. resolution element 0 4 arc-sec.

TABLE 12. CALCULATED rms SURFACE HEIGHTS FROM THE MAX PLANCK SCATTERING DATA

Flat Description	λ (Å)	d_{max} (μm)	θ_{min} (arc-sec)	$f(\theta_{min})$ (%)	σ (Å)	d_{max} (μm)	θ_{min} (arc-sec)	$f(\theta_{min})$ (%)	σ (Å)	TIS (visible)	σ(Å) Talystep
Fused Silica Pt PE	8.3	500	50	0.7	8.3	200	130	0.1	3.1	5.8	---
Fused Silica Pt PE	2.7		16	0.7	2.8		42	0.3	1.8		
Fused Silica Pt PE	1.9		12	0.4	1.5		30	0.2	1.0		
Fused Silica Pt PE	1.5		9	1.1	1.9		23	0.7	1.5		
Fused Silica Pt IT	8.3		50	0.2	4.4		130	0.05	2.2	2.2	1.7
Fused Quartz Pt EK	8.3		50	0.2	4.4		130	0.04	2.0		
Fused Quartz Pt EK	1.9		12	1.4	2.7		30	0.8	2.0		
Fused Silica Au PE	8.3		50	0.8	8.9		130	0.2	4.4	9.7	
Fused Silica Au PE	1.9		12	0.3	1.2		30	0.2	1.0		
Zerodur Ni IT	8.3		50	0.2	4.4		130	0.05	2.2	3.3	3.9
Zerodur Ni PE	1.9		12	0.8	2.0		30	0.5	1.6		

VII. NON-X-RAY TECHNIQUES USED TO MEASURE SURFACE FIGURE AND IRREGULARITIES

7.1 The MSFC BRDF Scatterometer

7.1.1 Measurement system

A computer-controlled scanner was built to measure the bidirectional reflectance distribution function (BRDF) of the AXAF mirror samples. The scanner has the capacity to cover the full hemisphere above a sample for any angle of incident light. A block diagram of the system is shown in Figure 31. The scanner is controlled in three axes. The inner axis moves a detector in an arc above the sample surface, the mid axis changes the azimuth of the arc scan, and the outer axis moves to change the angle of incidence of the light beam on the sample surface. The detector is a photomultiplier (PMT) mounted close to the axis of scan. The PMT looks up through a tube to a small diagonal mirror which directs the field-of-view down to the surface of the sample. The tube baffles the ambient light from the PMT and restricts the field-of-view around the sample surface. The three axes of the scanner are driven by stepper motors under microprocessor control. The position is recorded by counting the steps.

The sample can be illuminated by either a Spectra Physics Model 133 He-Ne laser with a wavelength of 632.8 nm or a Spectra Physics Model 162 Argon laser set to a wavelength of 488.0 nm. Both lasers have polarized beams. The laser beam striking the surface is chopped at 1000 Hz with a mechanical chopper wheel. The size of the beam on the surface is about 3 mm in diameter. The system does not contain any optical apparatus to converge the laser beam and focus the light at the detector, a theoretical requirement for obtaining a true Fourier transform. However, the discrepancy between measurements made with and without a converging lens was so slight that the optics were deleted in favor of maximum laser power.

The small diagonal mirror that directs the field-of-view of the PMT to the sample is located 30.5 cm from the sample surface. At that point there is a 3 mm diameter aperture. The resulting field-of-view of the PMT is about 5 deg at the half power points. The signal from the PMT is processed through a preamplifier on the scanner to a Princeton Applied Research Model 124 lock-in amplifier. The signal from the lock-in amplifier is converted to a log scale with an Analog Device 755P log-amplifier and then converted to BCD with a 4.5 digit panel meter. The microprocessor control computer stores the data during a scan. After the scan, the data is sent to a Sigma V computer which stores the data for later processing. A program on the Sigma V computer converts the scan data to a BRDF format and provides both graphic and digital output of the computed results.

7.1.2 Experimental Procedure

The AXAF mirrors are supplied in sets. One mirror of the set is 4 in. long; the other is 6.5 in. long. Four measurements are made on the short samples and six measurements are made on the longer samples, at 1 in. intervals along the surface. At each point on the surface of the mirror two scans are made. The scanner first moves the outer axis to position the sample surface normal to the light beam. It then moves the mid axis until the scan arc is perpendicular to the direction of polarization of the beam. The inner axis is then driven starting at 85 deg and ending at 1 deg from the normal to the surface, with data taken in 1-deg increments. After the first

scan, the mid axis is incremented by 1 deg and the inner axis scan is repeated. The two scans are averaged and used to compute the rms surface roughness. The two scans are made to average laser speckle effects.

Each day prior to taking a series of measurements the scanning system is calibrated by using a 3-M white paint sample. The 3-M white has a very good Lambertian scatter surface at normal incident. The BRDF plot gives a straight line with a position of 0.318 relative intensity per steradian. Figure 32 is a plot of the 3-M white data in the BRDF format. Both axes are log scales. BETA-BETAO, plotted on the X axis, is the sine of the detector scan angle minus the sine of the angle of incident light. All of the AXAF mirrors were measured with the light incident normal to the surface. Therefore, for the cases here, BETA-BETAO is actually the sine of the detector angle. The Y axis, labeled SCATTERING FUNCTION, is the radiant intensity measured at each detector position normalized to the incident flux and the surface specular reflection divided by the cosine of the detector angle.

7.1.3 Calculation of RMS Surface Roughness

The signal from the scanner is the radiant intensity measured at various angles above the sample surface. The total diffuse scatter is calculated by assuming that the scatter is radially symmetrical about the normal to the surface. Therefore, for the numerical integration, each reading has to be scaled to the fraction of solid angle subtended around the normal to the surface. The formula used is given in equation (18).

$$\text{SOLID ANGLE} = 2*PI*SIN(THETA)*(DELTA\ THETA) \tag{18}$$

where THETA is the detector angle from the surface normal and DELTA THETA is the increment between readings. The solid angle times the detector reading in mw per steradian give the radiant flux within that solid angle. The total diffuse scatter is then obtained by adding up values represented by each reading. The total flux is divided by the incident power and the specular reflection to normalize the results. The formula to convert the total diffuse to the rms surface roughness is given in equation (19).

$$RMS = (LAMBDA/(4*PI))* \ln(1/(1-B)) \quad , \tag{19}$$

where LAMBDA is the wavelength in Angstroms, B is the total integrated scatter, and the maximum value of B is one. When the total integrated scatter is much less than one, equation (19) reduces to the more familiar equation (20).

$$RMS = (LAMBDA/(4*PSI))* B \quad . \tag{20}$$

Since the total diffuse scatter is calculated by adding up readings from 85 to 1 deg, the spatial frequency range covered by the rms value is from 0.6 to 36 μ.

7.1.4 Results

The results of the rms surface roughness values as measured with this technique are given in Tables 13 through 16. Table 13 gives the most information since it gives the rms values measured at different positions on each surface. Tables 14, 15, and 16 all give identical information. But, Table 14 sorts the flats by the manufacturer; Table 15 sorts them by the substrate; and Table 16 sorts them by the coating. In these last three tables the rms values from Table 13 are averaged for each surface to give one rms value for the entire surface.

7.2 Twyman-Green Interferometer Measurements

Twyman-Green interferometer measurements are made at MSFC on the AXAF mirror samples to quantify the low spatial frequency flatness of the surfaces. Spatial frequencies in the range of 1 cm up to the size of the sample are measured. The exact range varies with the number of fringes. The number of fringes used on the AXAF samples varies from 20 to over 40 across the surface.

The optical layout used is shown in Figure 33. It is the layout of a commercial Twyman-Green interferometer Model 723 made by Perkin Elmer Corporation. The actual optical configuration will vary depending on the type optical component being tested. The AXAF samples were too large to be completely illuminated by the 10 cm (4 in.) collimated beam generated by the instrument so the samples were tested at an angle. The angle was set at 60 deg to retain the usual factor of 2 between the surface error and the optical path difference. At the 60 deg angle the cosine is 0.5 so any error in the surface will appear to be one-half the actual size; however the beam hits the surface twice, so the error is compensated.

A description of the operation is as follows: The laser light source is collimated to a beam diameter of 10 cm (4 in.) by lens one and two. Mirror No. 1 is used to fold the beam for convenient layout on the table. The beam splitter diverts part of the beam to reference mirror one which returns the beam by reflection from the beam splitter to the camera/eyepiece optics. The other part of the collimated beam is reflected off the AXAF sample to the reference mirror No. 2 which returns the beam along the same path to the beam splitter. There the beam is rejoined with the part from the first reference mirror. The resulting interference is observed with the camera/eyepiece optics.

The operator adjusts reference mirror No. 2 until he has the desired fringe pattern. Because there is more information along the fringe, two shear directions are photographed. In one the fringes run parallel to the long axis and in the other they run perpendicular. A microscope slide with a code number is positioned over reference mirror No. 2 so that each photograph can be tracked and related to the sample number. The photographs are made on Polaroid positive/negative film type 55.

The negatives are analyzed on a Grant microdensitometer. The process is manual and requires an operator to position the X-Y stage to each fringe center and record a sample point. At each sample point the operator hits a record button and the position data is recorded on punch cards. The operator records sample points in a pattern of scan lines perpendicular to the fringes. The scans are repeated at regular intervals corresponding roughly to the fringe spacing resulting in a grid of data points. The number of total data points varies from sample mirror to sample mirror due to the difficulty of setting the same number of fringes on each sample.

The punch card data is processed by a fringe data reduction program on a Honeywell Sigma V computer. The computer program, using least squares fitting routines, removes alignment errors of piston, tilt, and defocus. The remaining errors are analyzed and printed out by the program for permanent record. The summary table (Table 13) includes the Root Mean Square (rms) of the surface figure errors. The light source used in the interferometer is a Perkin Elmer Model 5200 He-Ne laser so that the rms surface figure is in terms of fractions of a wavelength at 632.8 nm. The accuracy achieved is about $\lambda/50$ rms.

7.3 The Polarization Profilometer

7.3.1 Introduction

This section describes a non-contact method of measuring surface profile, without the need for a reference surface, that is capable of height sensitivities on the order of 1 Å. It does not require any surface preparation and can be used with highly reflecting surfaces as well as bare glass surfaces. Because the surface profile is measured directly, the autocovariance function, spectral density function, and statistical properties of the surface can be determined analytically. The following paragraphs will describe the principles of this method and their incorporation into an instrument, data acquisition and analysis, graphical outputs, sources of errors, limits on sensitivity, and repeatability. This technique was developed and the measurements were carried out at the Lawrence Livermore National Laboratory.

7.3.2 Principle of Operation

The basic principle involved in this surface profile measuring method is heterodyne interferometry. When a surface is illuminated by two focused beams of light of slightly different frequency and the reflected beams interfere, the phase of the sinusoidal intensity modulation is related to the height difference between the illuminated points on the surface. If one of the beams remains focused on a fixed point while the other beam is moved along the surface, then height variations along the scanned line are measured. The following subsections describe the details of this method.

7.3.2.1 Optical System

The optical system used to implement the principle outlined above is shown in Figure 34. The light source, shown in Figure 35, is a single mode helium neon laser with its center frequency Zeeman split by an axial magnetic field on the laser tube. The laser is stabilized in two respects: a phase lock loop is used to control the strength of the magnetic field so as to lock the Zeeman frequency to a reference crystal; the relative intensities of the two frequencies are used to control the length of the laser cavity so as to keep them centered on the gain curve, thus stabilizing their absolute frequencies. The laser output consists of two colinear orthogonally, linearly polarized beams with a frequency difference of 2 MHz. These beams pass through a telescope/spatial filter to remove spatial noise and reduce their diameter. A polarization insensitive beam splitter reflects a small fraction of each beam through a pair of waveplates, that serves as an adjustable phase bias, and a polarizer oriented at 45 deg to each polarization, permitting them to interfere at the reference photodetector.

The transmitted beams are directed vertically by a pair of adjustable mirrors to an interferometer comprised of a Wollaston prism, microscope objective, and the surface being measured. The Wollaston prism introduces an angular divergence between the orthogonally polarized beams so that the objective brings them to focus at two distinct points on the surface, one on either side of the optic axis with one on the axis of rotation of the rotary table as shown in Figure 36. The points are separated by approximately 100 μm. The reflected beams are recombined by the Wollaston prism and leave on a path parallel to the incident beams but are displaced to eliminate overlap. This physical separation is required to prevent light from returning directly to the laser and causing cavity de-tuning. The beams pass through an adjustable neutral density filter, to compensate for surface reflectivity, and a polarizer to the measurement photodetector as shown in Figure 37.

7.3.2.2 Phase/Height Detection

The amplitude of the field at either photodetector can be expressed by

$$V = V_+ + V_-$$

$$= e^{i(k_+ z_+ - \omega_+ t)} + e^{i(k_- z_- - \omega_- t)} , \qquad (21)$$

where ω is the angular frequency, k is the wavenumber, z is the distance travelled, and the subscripts + and - correspond to the up-shifted and down-shifted beams. The signal, S, from each photodetector is proportional to the irradiance, $I = |V|^2$. The signal from the reference photodetector is given by

$$S_r = \left| e^{i(k_+ z_r - \omega_+ t - 2\theta)} + e^{i(k_- z_r - \omega_- t + 2\theta)} \right|^2$$

$$= 2\,(1 + \cos\,[(k_+ - k_-)\, z_r - \omega' t - 4\theta]) \quad , \qquad (22)$$

where $z_+ - z_- = z_r$ is the common path length travelled by the reference beams, $\omega' = \omega_+ - \omega_-$ is the angular Zeeman frequency, and θ is the angular position of the half-wave plate. The signal from the measurement photodetector is given by

$$S_m = \left| e^{i(k_+ (z_m + z/2) - \omega_+ t)} + e^{i(k_- (z_m - z/2) - \omega_- t)} \right|^2$$

$$= 2\,(1 + \cos\,[(k_+ - k_-)\, z_m + \frac{(k_+ + k_-)}{2} z - \omega' t]) \quad , \qquad (23)$$

where $z_+ = z_m + z/2$ and $z_- = z_m - z/2$ are the path lengths travelled by the measurement beams, with z_m being the average path length and z being the difference in path lengths. The phase difference, ϕ, between these signals is

$$\phi = (k_+ - k_-)(z_m - z_r) + \frac{(k_+ - k_-)}{2} z + 4\theta \quad . \tag{24}$$

Using the relationships

$$k = \omega/c \quad \text{and} \quad \omega = 2\pi f \quad , \tag{25}$$

the wavenumbers can be expressed as

$$k_+ = \frac{2\pi}{c}(f + f'/2) \quad \text{and} \quad k_- = \frac{2\pi}{c}(f = f'/2) \quad , \tag{26}$$

where f is the center frequency of the laser and f' is the Zeeman frequency. It can be easily shown that

$$k_+ - k_- = \frac{2\pi}{c} f' \quad \text{and} \quad \frac{k_+ + k_-}{2} = \frac{2\pi}{c} f \quad . \tag{27}$$

Substituting into equation (24) gives

$$\begin{aligned} \phi &= \frac{2\pi}{c}[f'(z_m - z_r) + fz] + 4\theta \\ &= \frac{2\pi}{c}[f'z' + fz] + 4\theta \quad , \end{aligned} \tag{28}$$

where $z_m - z_r = z'$ is the path length difference between the measurement and reference beams. Equation (28) represents the phase between the two photodetector signals as a function of the system parameters. As one of the measurement beams is scanned along the surface, changes in the surface height cause z to change producing a linearly related phase change. Note, however, that changes in the other parameters will also result in a phase change which is indistinguishable from the contribution due to the surface profile. In general the phase change, $\Delta\phi$, can be expressed as

$$\Delta\phi = \frac{2\pi}{c}(z'\,\Delta f' + f'\,\Delta z' + z\Delta f + f\Delta z) + 4\Delta\theta \quad . \tag{29}$$

The last term in parenthesis is the contribution from the surface. The other terms represent instabilities of the system. The first term corresponds to drift of the Zeeman frequency, the second and last terms to mechanical drift, and the third term to cavity de-tuning. Contributions to the phase change from instabilities in the system are orders of magnitude below the contribution of angstrom surface height variations. Therefore, all but the surface contribution can be dropped from equation (29) leaving

$$\Delta\phi = \frac{2\pi}{c} f \, \Delta z$$

$$= \frac{2\pi}{\lambda} \Delta z \quad , \tag{30}$$

where $\lambda = c/f$ is the center wavelength. The optical path change, Δz, can be expressed in terms of the surface height change, Δh, shown in Figure 38 as

$$\Delta z = 2\Delta h \cos \beta_{+} \quad . \tag{31}$$

The angles, $\beta_{\pm}$, are functions of the geometry and are given by

$$\beta_{\pm} = \tan^{-1} \frac{b_{\pm} (d - f) \tan \alpha_{\pm}}{f} \tag{32}$$

where f is the focal length of the microscope objective and b is the displacement of the central ray of the incident beam. When the apparent plane of splitting of the Wollaston prism is in the back focal plane of the objective, $d = f, \beta$ is independent of the prism angles $\alpha_{\pm}$ and there is complete symmetry between the incident and return beam. For this case, equations (30), (31), and (32) can be combined to express the surface height change in terms of the measured phase change as

$$\Delta h = \frac{\lambda \sqrt{b^2 + f^2}}{4\pi f} \Delta\phi \quad . \tag{33}$$

To maximize the lateral resolution of the system, the incident and return beams at the Wollaston prism are as close together as practically possible and their diameters are sufficient to fill the objective. Under this condition b is approximately one quarter of the objective diameter. Equation (33) can then be written in terms of the numerical aperture of the objective (NA = 2b/f) as

$$\Delta h = \frac{\lambda}{8\pi} \sqrt{NA^2 + 4} \, \Delta\phi \quad . \tag{34}$$

It should be noted that the local slope of the surface at the point of measurement causes a small offset in the return beam, but it has no effect on the measured phase.

7.3.2.3 Rotary Table

The rotary table is a hollow core air bearing type. Although surface profile measurements with angstrom level sensitivities are the goal, the mechanical specifications on the table are not extraordinary. As the table rotates it will undergo some degree of translation and tilt with respect to the fixed frame. Axial motion does not affect the phase measurement beams. It is only required that the axial motion be less than the depth of field of the microscope objective. Radial motion must be a small fraction of the focused beam size so that the axial beam remains at one point on the surface.

Tilt, which occurs when the table normal is not parallel to the axis of rotation, does affect the phase measurement because it introduces a differential path length change between the measurement beams. A fixed tilt causes the normal to precess, which results in an additive sinusoidal term in the phase measurement. This effect is easily removed as described in the next subsection. Random tilting leads to non-recoverable surface errors on the order of 2 Å for each microradian of tilt. Therefore, maximum random table tilts should be a fraction of a microradian.

To eliminate the possibility of phase measurement error due to air turbulence from the bearing, the rotary table is placed outside the sealed optical enclosure. Beam tubes and oil bath seals are used to isolate the beams as they pass to and from the surface through the center of the air bearing.

The table is friction driven by a synchronous motor powered from a crystal oscillator. The period of rotation, used for data acquisition, is approximately 30 sec with less than a 0.07 percent deviation over 8 hours. Each morning the period is automatically timed using the LED/photodetector shown in Figure 1 to update its value, which may change in time due to friction drive wear.

Initial alignment of the axial point is performed by placing a ground glass surface on the rotating table. Using a polarizer to eliminate one of the transmitted beams, the speckle pattern from the other beam is observed on a screen above the table. This pattern moves across the screen when the focused beam is not on the axis of rotation. By translating the objective, a position can be found where the speckle pattern rotates with the table with little change in its overall structure. This corresponds to the axial position.

7.3.2.4 Data Acquisition and Analysis

A desk-top computer controls all functions, from timing the table rotation to the graphical display, including data acquisition and analysis. Data is taken at equal time intervals determined by the period of rotation and the 512 data points taken per table revolution. When a surface is being scanned, the computer reads the digital output of the phase detector at this rate for a total of 513 data points. The first and last data points correspond to the same surface position and serve as an indication of the system repeatability. Their difference typically corresponds to less than 2 Å.

During analysis the data is checked and corrected for 2π radian discontinuities which occur if the surface height variations are greater than $\lambda/2$. The phase data is converted to surface height data using equation (34). The data is then modified to remove two additive sinusoidal modulations that are always present. The first modulation has a period equal to the period of rotation. It is introduced when the surface normal is not parallel to the axis of rotation. The cause can be a tilted table top or, in most instances, dust particles between the table top and the surface. The second modulation has a period equal to one half the period of rotation and is associated with the small degree of astigmatism that all surfaces exhibit. These modulations, as well as the average value, are eliminated by a least squares fit. The peak-to-valley (p-v) and rms values are calculated for the entire scan and eight individual segments. The surface profile is plotted in a circular format with the height scale automatically set using the p-v value.

A number of functions that characterize the surface are calculated and plotted with the surface profile. The normalized autocovariance function for discrete equally spaced height data is given by

$$A(ms) = \sum_{n=1}^{N} h\,[(n+m)s]\; h\,(ns) \Big/ \sum_{n=1}^{N} h^2\,(ns) \quad , \tag{35}$$

where m is an integer such that $0 \leq m \leq N-1$ and s is the arc length between data points. Normally the autocovariance function is defined along a straight line rather than on a circle; however, the significant features of this function occur for small values of m where arc lengths are approximately equal to chord lengths.

The spectral density function describes the angular distribution of light scattered from the surface. For discrete equally spaced points the spectral density function is given by

$$S(u) = \left| \sum_{n=1}^{N} W(ns)\; e^{\frac{-2\pi i n s u}{\lambda}} \right|^2 \Big/ \sum_{n=1}^{N} |W(ns)|^2 \quad , \tag{36}$$

where $u = \sin\theta$, θ is the scatter angle, and W is the reflected wavefront at the surface as the result of plane wave illumination. The wavefront is related to the surface profile by

$$\begin{aligned} W(ns) &= Re^{-2ikh(ns)} \\ &= Re^{\frac{-4\pi i h(ns)}{\lambda}} \quad . \end{aligned} \tag{37}$$

where R is the reflection coefficient. For normalization its value is taken as unity so that S(O) is the fraction of light that is specularly reflected. The spectral density function is plotted on a log-log scale with the normalized specular reflectivity printed within the plot.

The height and slope distribution functions have been derived by accumulating the magnitudes of the heights, $|h(ns)|$, and slopes, $|h((n+1)s)-h(ns)/s|$, for $1 \leq n \leq N$ in increments of one-third their respective rms values. They are plotted with a least squares fitted normal distribution, which represents an ideal isotropic surface.

7.3.3 Measurements

This section describes the use of the instrument for typical surface measurements. The actual stability and repeatability of the instrument are discussed and shown by graphical plots. The measured rms surface roughness values for the AXAF flats are given in Tables 19 through 22.

7.3.3.1 Surface Profiles

In its normal mode of operation, the instrument is used to measure flat surfaces. No adjustments are necessary from surface to surface. When surfaces with non-planar figures are measured, careful placement of the sample and refocusing are required.

To measure the profile of a surface, the surface and the table top are first cleaned to remove any film or dust particles. The surface is then placed on the table. If the surface is not cleaned thoroughly, the digital surface height display will show a sinusoidal modulation as the table rotates, indicating that further cleaning is necessary.

7.3.3.2 Stability and Repeatability

In an earlier section, the stability was derived in terms of the optical parameters associated with the laser and optical system. Direct measurement of the stability is achieved by using the same measurement procedures outlined above except that the rotary table is stationary. Since all the data is taken at a single point on the surface, the plot of the surface profile should be a perfect circle. Figure 39 shows a typical stability test. The abrupt changes are level transitions in the analogue-to-digital converter which digitizes the analogue phase detector output.

Long-term stability has also been measured by recording the analogue phase detector output on a strip chart. Smooth periodic variations, with an amplitude of several angstroms and a period (depending on warm-up) from 15 min to several hours, are common. The source of this instability is not presently known, although preliminary tests of individual items (e.g., electronics, laser, air turbulence) indicate the laser may be the problem.

The repeatability of the instrument is determined by measuring a surface several times in succession. The p-v values typically differ by less than 4 Å and the rms values by less than 1 Å. A double scan of a surface is shown in Figure 40.

7.3.4 Limitations

Every technique used to measure surface profile, whether it is based on mechanical contact, visible light, X-rays, electron beams, capacitance, or magnetic fields, averages over some finite lateral area. In the technique described in this paper, diffraction limits the resolution to about a 2 μm diameter spot so that the measured height at a particular surface point is actually a weighted average over the spot size. Thus, the lateral extent of the averaged area is about 20,000 times the height sensitivity. At first this may appear to be a meaningless measurement; however, it must be realized that lateral surface structure has little or no effect on the performance of the surface when it is less than the wavelength used with the surface, whereas vertical surface variations on the order of angstroms will have a measurable effect. Therefore, for surfaces used in the visible and infrared parts of the spectrum, the pertinent information lost by averaging over a 2 μm diameter area is minimal.

7.4 The FECO Interferometer

7.4.1 Description of Method

Multiple-beam fringes of equal chromatic order (FECO) are formed when a collimated beam of white light undergoes reflections between two partially silvered surfaces, one of which is the surface whose profile is being measured and the other is a supersmooth reference surface. Upon dispersing the light via a prism or grating, the FECO fringes show up as dark wiggly lines in a bright continuum. These wiggles are contours in the wavelength regime of the microirregularities on the pair of surfaces. A block diagram of a FECO interferometer is shown in Figure 41.

The resolution limit of this instrument is typically such that the surface can be characterized in terms of squares of size 2 μm x 2 μm. Hence, in this method surface topography is calculated from the statistics of these square element averaged properties. Information which is obtained by this instrument includes the rms surface height, the rms slope, and the autocovariance function of the surface.

7.4.2 Spatial Frequency Range

Surface roughness is measured using a "direct contact" FECO interferometer. Flats are coated with silver for 95 percent reflectance and 5 percent transmittance. These samples are cleaned with a sonic cleaner and a methyl alcohol wash. Interference orders of approximately 10 are obtained. The resolution of the film provides an upper limit to the spatial frequencies that can be measured. This limit is estimated at 300 cycles/mm (or a period of about 3 μ).

Surface roughness is divided into two segments for measurement. High frequencies between 33 and 300 cycles/mm are estimated by measuring the width of the fringe and dividing by 6 to convert to rms. Spatial frequencies below 33 cycles/mm are measured by scanning the interferogram with a scanner aperture of 30 μ. This provides an rms value for the low spatial frequencies. The two computed rms values are root-sum-squared to provide an estimate of the surface roughness covering spatial frequencies of from 0.5 to 300 cycles/mm. The autocorrelation function is computed from the scanned data. This provides autocorrelation information only for surface roughness of spatial frequencies between 0.5 and 33 cycles/mm.

7.4.3 Results

The FECO measurements were made by the respective vendor of each particular flat. These vendors were Perkin Elmer, Itek, and Eastman Kodak. The results of the measured rms surface roughness heights are included in Table 17.

7.5 The Total Integrated Scatter Method

Total integrated scatter (TIS) values of the rms surface height structure were obtained experimentally by NWC in China Lake, California. This method is perhaps one of the simplest methods for obtaining information about the microirregularities of "almost smooth" surfaces. The theoretical relationship between the total integrated scattered light from a surface and the rms surface height is based on the assumption that the height distribution is Gaussian. In this case, the total integrated fraction of light which is scattered is given by the following relation:

$$\text{TIS} = \left(\frac{4\pi\sigma}{\lambda}\right)^2$$

where σ is the rms surface roughness, and λ is the wavelength of the incident light. The results of the TIS measurements of σ are given in Table 17.

7.6 Talystep Measurements

The Talystep instrument (Rank Precision Instrument Company) utilizes a stylus which actually contacts the surface to be measured. The smallest spatial wavelength that can be measured is determined by the contact area of the surface which, in turn, is determined by the radius of the stylus. See Figure 42 for a block diagram of the instrument and Reference 18 for a complete description of it.

Contact measurements of this type were made on some of the flats at NWC in China Lake, California, and at the National Bureau of Standards in Gaithersburg, Maryland. For the NWC measurements, the spatial wavelength range probed was from 0.1 μm to 1 mm. For the NBS measurements, two different ranges were probed: (1) short trace measurements corresponding to the range from 0.1 μm to 19 μm, and (2) long trace measurements extending from 4 μm to 600 μm. The results for the measured rms surface height via this method are given in Table 18. A more extensive discussion of the results can be found in Reference 17.

7.7 Fizeau Interferometer Measurements

The Fizeau interferometer works on the same principles as the Twyman-Green interferometer described in Section 7.2. The difference is that for the Fizeau interferometer, the reference flat, and the flat under study are in contact, whereas, for the Twyman-Green, they are not in contact.

Fizeau interferometric measurements were made on some of the AXAF test flats by Perkin Elmer. The deduced values of the rms surface waves (6328 Å) for these measurements are shown in Table 19 along with the corresponding values measured with the Twyman-Green interferometer.

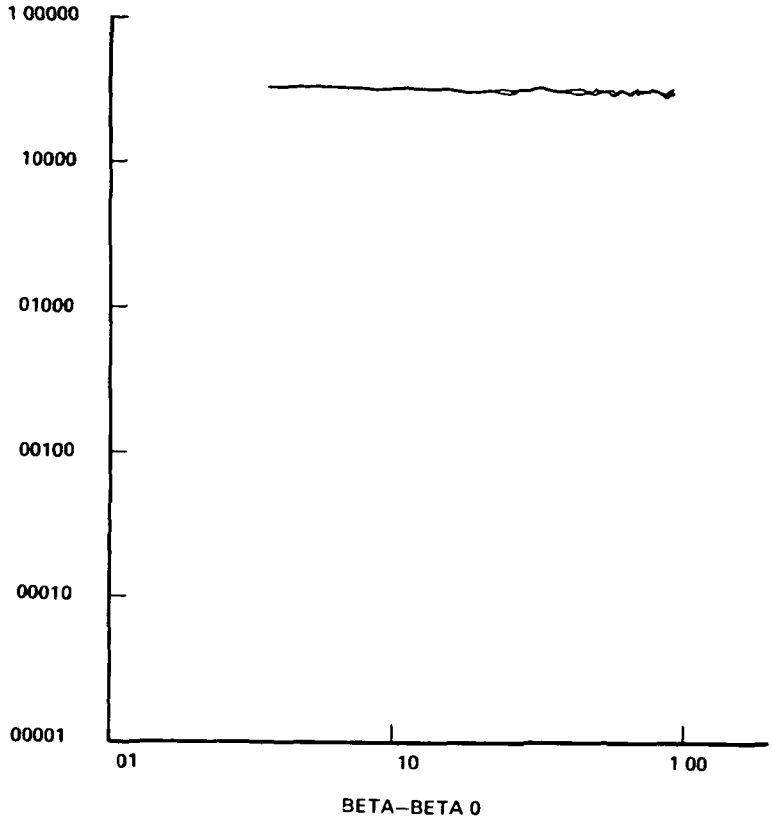

Figure 32. A 3-M white calibration run for the MSFC BRDF scatterometer.

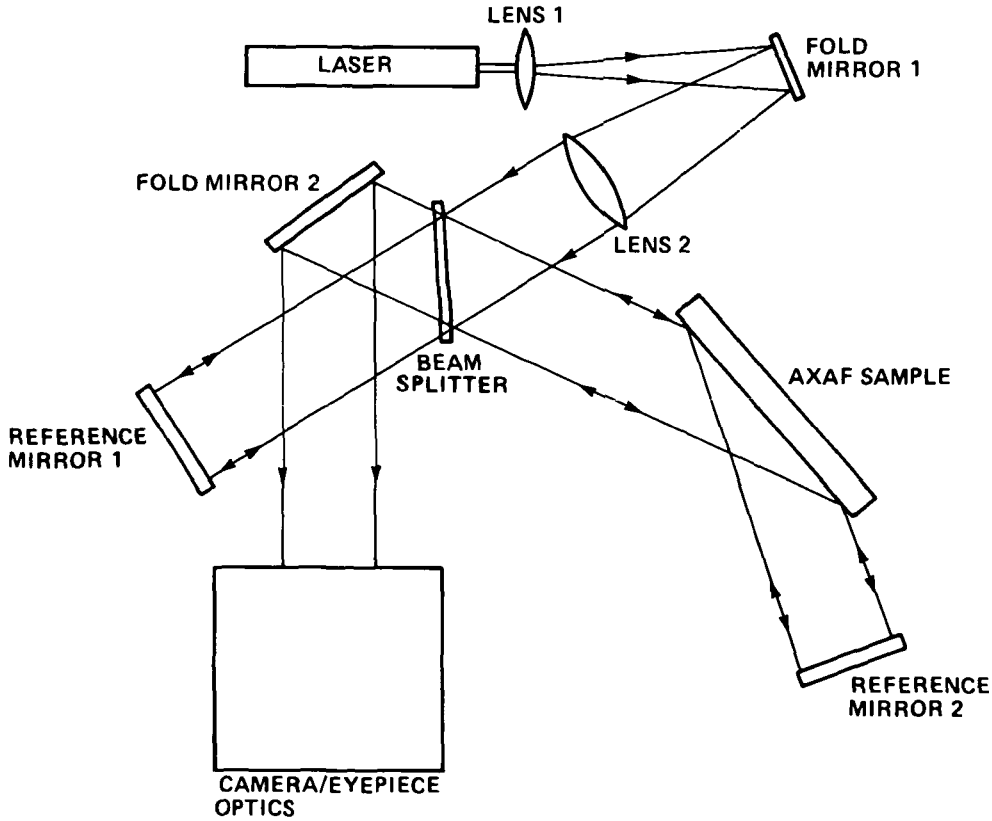

Figure 33. The optical layout of the Twyman-Green Interferometer used to measure the AXAF flats.

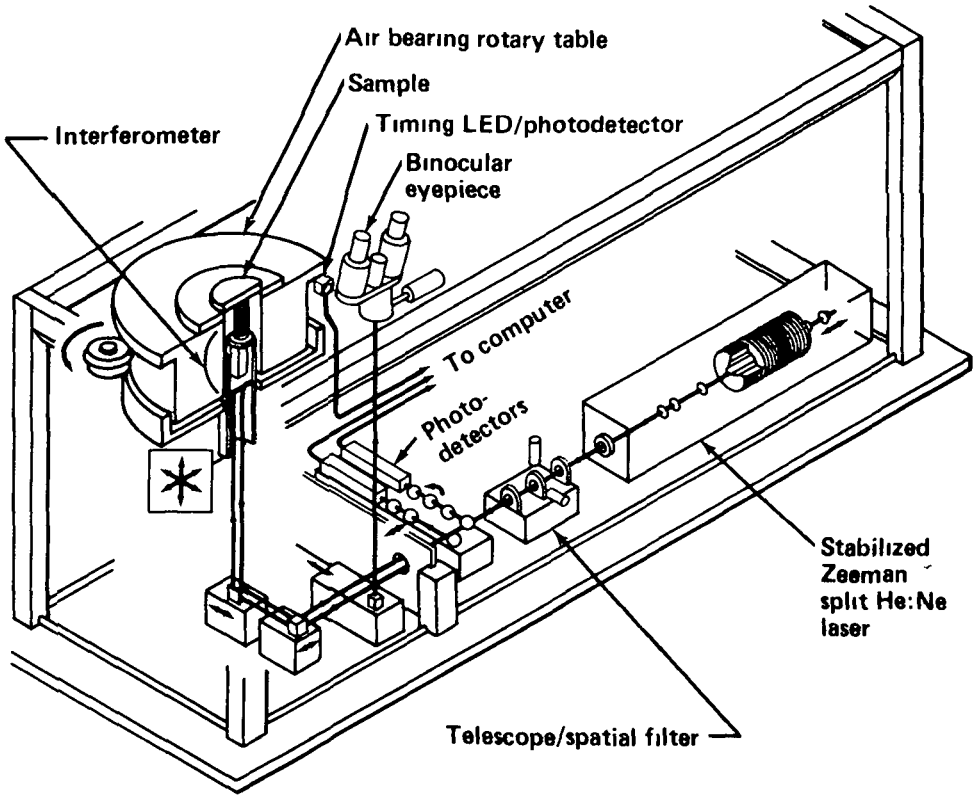

Figure 34. Schematic of the profilometer used to measure the AXAF flats.

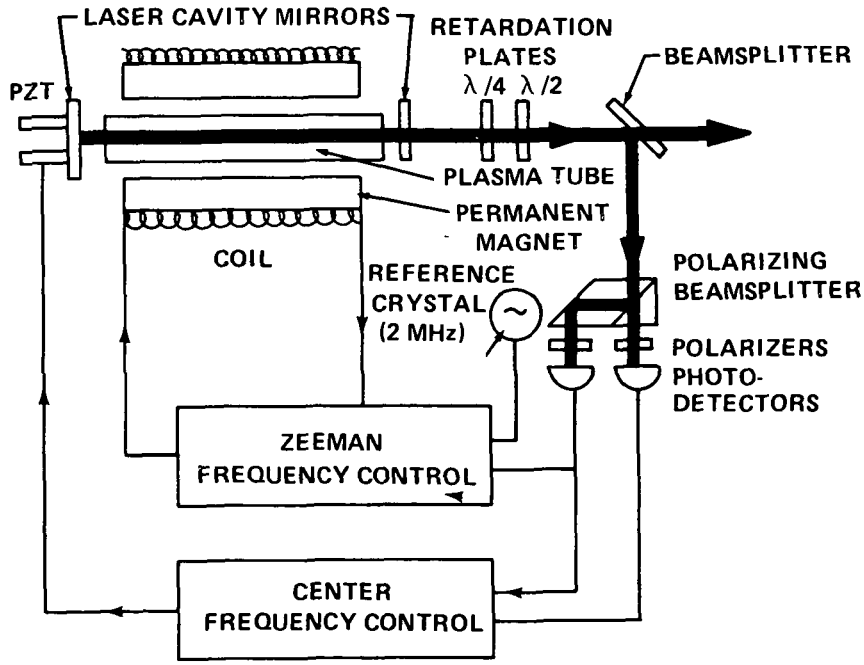

Figure 35. Schematic of light source for the profilometer.

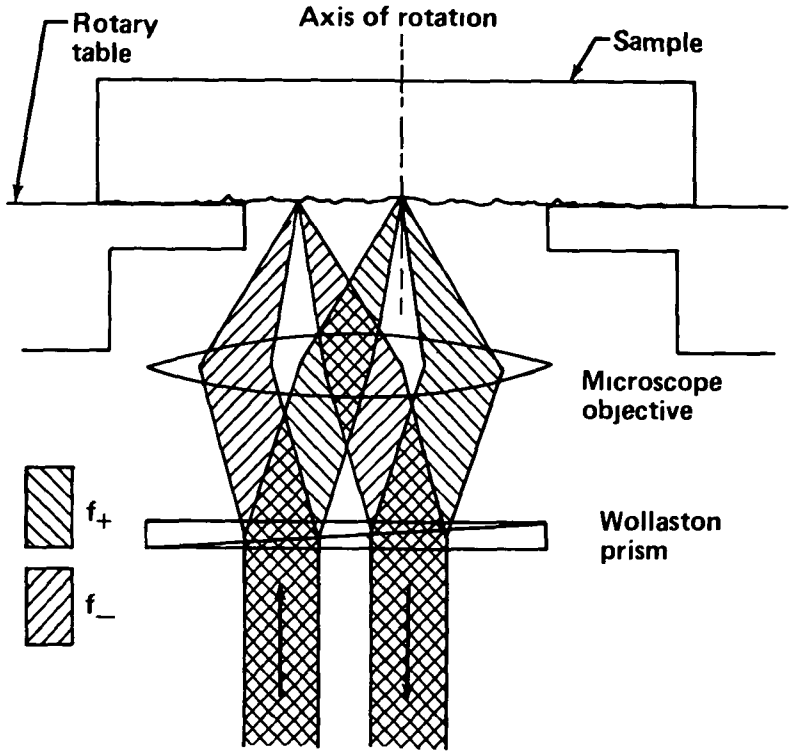

Figure 36. Details of the interferometer used in the profilometer.

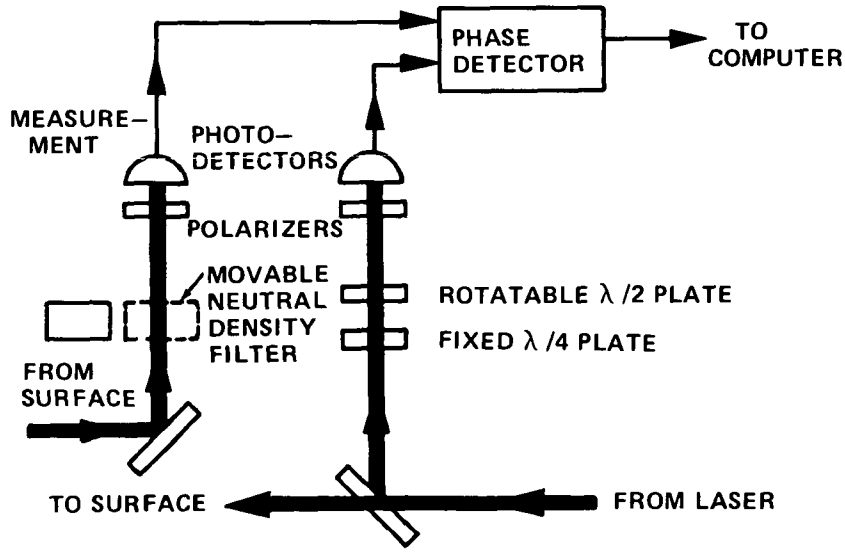

Figure 37. Details of the phase detector of the profilometer.

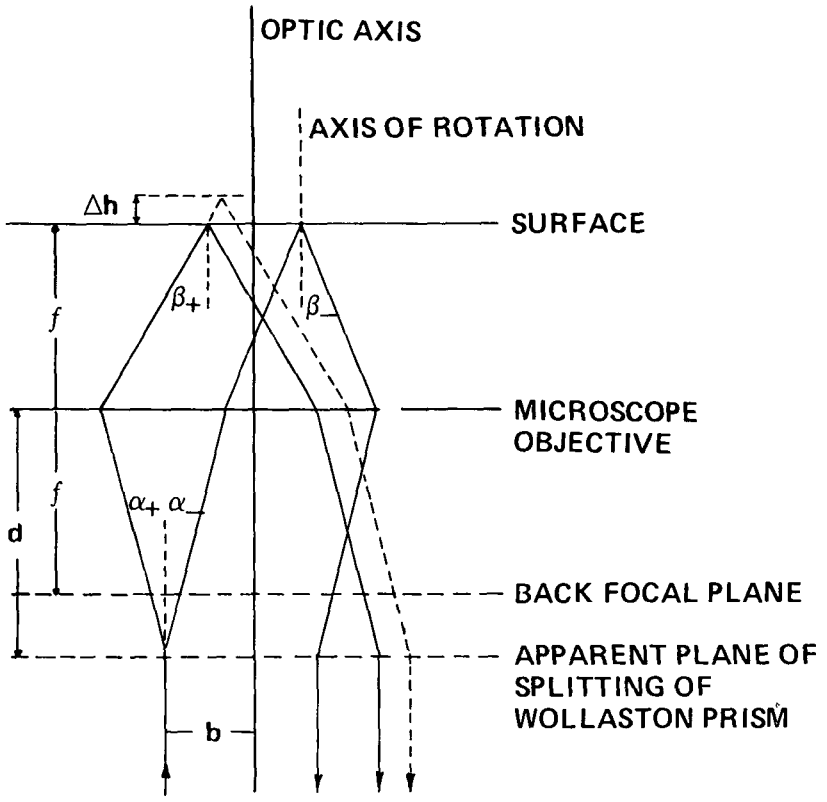

Figure 38. Beam path geometry in the interferometer.

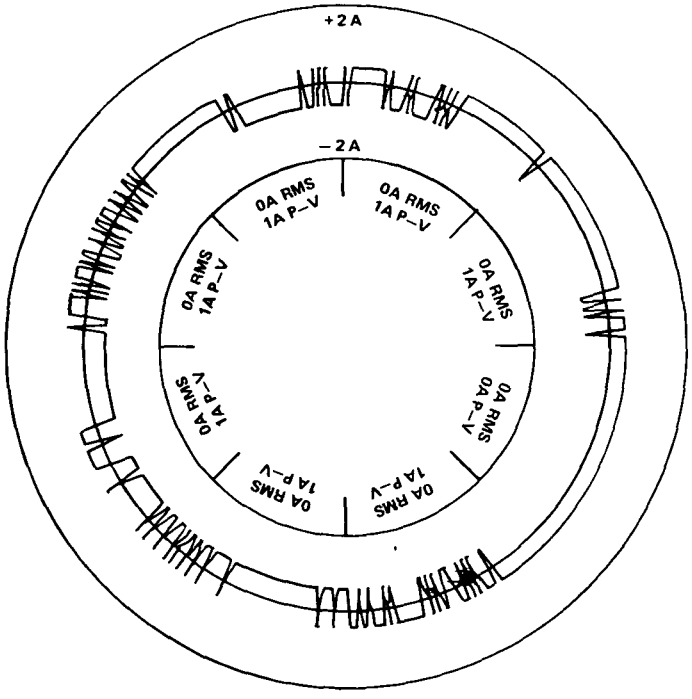

SURFACE PROFILE

0 5A RMS 1A P–V 0A ASTIG

Figure 39. Stability test of the profilometer.

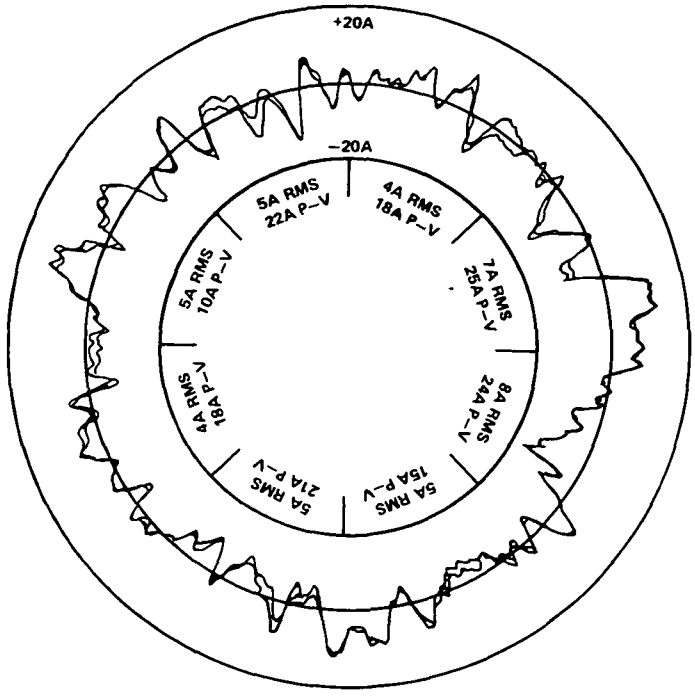

SURFACE PROFILE

5 8A RMS 30A P–V 4A ASTIG
5 3A RMS 28A P–V 4A ASTIG

Figure 40. Repeatability test of the profilometer.

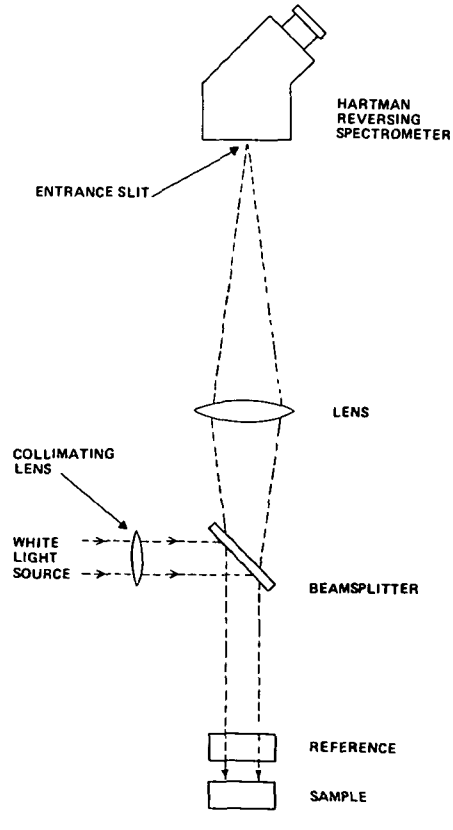

Figure 41. Schematic of the FECO interferometer.

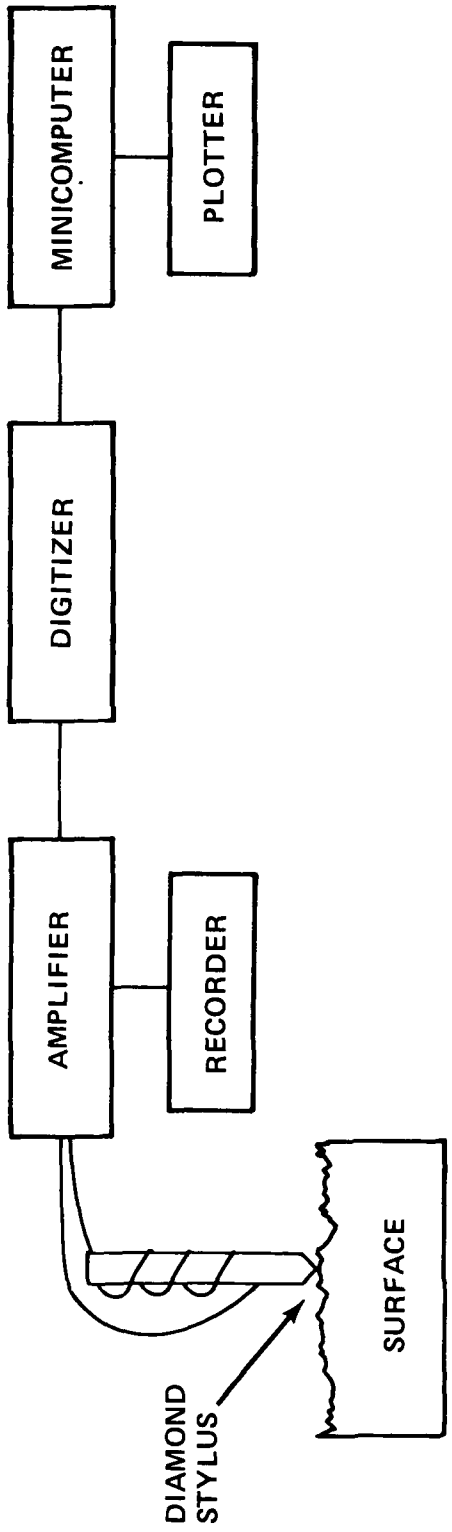

Figure 42. Block diagram of the Talystep surface profiling instrument.

TABLE 13. SUMMARY OF PROFILOMETER, BRDF SCATTEROMETER, AND THE TWYMAN-GREEN MEASUREMENTS ON ALL OF THE OPTICAL FLATS

COMPANY	SAMPLE I.D.	SUBS	COAT	LAWRENCE LIVERMORE LAB PROFILOMETER				BRDF SCATTEROMETER				TWYMAN GREEN V/H	
EK	I-1L	FS	Ni	3.4	4.8	5.3	4.3	2.9	5.6	14.8	5.2	.0467	.0562
				3.1	3.6	3.4		7.3					
EK	I-1S	FS	Ni	3.3	2.6	2.2	4.6	4.3	4.2	9.5	3.4	.0227	.0148
								3.2					
EK	I-2L	FS	Pt	4.9	5.6	5.4	7.5	4.4	6.0	9.3	4.4	.0388	.0427
								5.1	3.5				
EK	I-2S	FS	Pt	4.2	4.5	6.5	5.2	11.2	3.4	3.5	12.3	.0279	.0352
EK	I-3L	FS	Au	7.2	5.9	5.6	6.9	7.2	2.7	15.6	7.5	.0500	.0490
								2.4	3.4				
EK	I-3S	FS	Au	5.4	6.4	6.1	8.6	4.8	6.6	3.7	6.4	.0391	.0438
EK	II-1L	ULE	Au										
EK	II-1S	ULE	Au	5.5	5.4	5.3	7.3	3.1	4.9	3.8	2.6	.1000	.1064
EK	II-2L	ULE	Pt										
EK	II-2S	ULE	Pt	5.4	5.9	8.2	5.6						
EK	II-3L	ULE	Ni					23.2	11.6	15.9	10.8	.0658	.0595
								40.5	37.4				
EK	II-3S	ULE	Ni	5.6	3.0	4.1	4.8	2.7	3.1	4.9		.0862	.0794
EK	III-1L	Zed	Ni	12.2	9.9	9.6	14.3	2.1	2.0	1.9	2.2	.0595	.0694
								2.6	2.3				
EK	III-1S	Zed	Ni	4.6	6.8	6.5	6.5	2.0	1.8	2.1	1.7	.0406	.0291
EK	III-2L	Zed	Pt	11.5	12.4	9.2	12.1	8.9	15.7	20.9	18.7	.0667	.0490
								19.8	15.6				
EK	III-2S	Zed	Pt	30.4	26.7	20.9	30.7	12.9	10.7	7.6	28.9	.0439	.0368
EK	IV-1L	Cer	Ni	5.8	5.7	5.0	5.0	2.2	2.4	1.8	2.6	.0980	.1042
								1.7	1.7				
EK	IV-1S	Cer	Ni	9.9	5.0	7.7		4.8	3.6	3.1	4.3	.0658	.0562
EK	IV-2L	Cer	Pt					9.9	6.2	3.4	3.4	.0680	.0750
								4.9	2.7				
EK	IV-2S	Cer	Pt					8.0	3.6	7.1	7.7	.0430	.0460
EK	V-1L	FQ	Ni					3.5	6.5	1.9	2.3	.0472	.0424
								9.2	9.0				
EK	V-1S	FQ	Ni	4.0	2.7	2.6	2.7	2.5	2.0	2.2	2.0	.0446	.0403
EK	V-2L	FQ	Pt					6.1	7.4	10.0	4.4	.0360	.0310
								7.2	16.4				
EK	V-2S	FQ	Pt					4.8	5.6	6.3	4.3	.0410	.0400
EK	VI-3L	FS	Ni	7.4	8.9			5.8	6.3	7.5	6.6	.0481	.0420
								7.8					
EK	VI-3S	FS	Ni	9.7	7.4	10.3	6.8	7.6	7.2	7.5	7.4	.0382	.0236
MP	1a/R1L	Zed	Ni	2.9	17.6	3.9		14.0	10.0	6.3	11.0	.0214	.0144
								9.6	12.4				
MP	1b/R1S	Zed	Ni	3.6	2.7	5.6	3.9	17.0	13.5	7.8	9.4	.0159	.0148
MP	2a/R2L	Zed	Pt	12.5	137.2			9.9				.0325	.0217
MP	2b/R2S	Zed	Pt					19.0				.0160	.0272
MP	3a/R1L	Zed	Au	50.0	22.2			20.0	16.8	15.3	16.7	.0310	.0155
								20.6	24.4				
MP	3b/R1S	Zed	Au	11.1	86.8			32.5	32.5	33.3	35.0	.0129	.0168
PE	1-001L	FS	Pt					11.3	38.0	37.3	14.0	.0320	.0280
								11.7	17.6				
PE	1-004S	FS	Ni					11.5	8.3	7.9	8.5	.0220	.0330
PE	1-002L	FS	Ni	3.6	2.9	2.3	2.4	2.6	2.1	1.9	2.9	.0362	.0515
								2.1	2.1				
PE	1-002S	FS	Ni	4.7	3.0	2.2	3.7	1.6	1.8	1.8	1.6	.0273	.0237
				2.7									
PE	1-004L	FS	Au					7.9	5.6	5.7	7.3	.0310	.0310
								10.7	7.9				
PE	1-003S	FS	Au					12.2	14.4	9.8	10.5	.0230	.0320
PE	2-001L	ULE	Au										
PE	2-001S	ULE	Au										

TABLE 13. (Concluded)

PE	2-003L	ULE	Ni	3.0	4.0	3.5		3.7	2.5	1.6	1.6	.0338	.0398
								2.3	2.2				
PE	2-003S	ULE	Ni	4.1	4.0	4.1		1.9	2.2	2.0	3.2	.0223	.0244
PE	2-004L	ULE	Pt	3.4	3.5	3.9	4.2	2.2	3.2	3.3	3.3	.0282	.0314
				3.2				3.6	2.9				
PE	2-004S	ULE	Pt	3.9	3.8	3.1	4.9	5.4	8.6	8.0	3.4	.0276	.0189
				4.4									
PE	3-001L	Zed	Pt	4.2	3.4	2.9	3.5	4.1	5.0	3.8	2.8	.0388	.0331
				3.1				3.8	28.9				
PE	3-001S	Zed	Pt	3.3	3.3	3.6	3.2	3.8	6.3	3.7	4.3	.0165	.0239
				3.4									
PE	3-003L	Zed	Au	11.7	7.9	5.4		5.3	5.8	15.2	12.2	.0376	.0413
								4.9	3.4				
PE	3-003S	Zed	Au	2.5	5.4	3.1		4.7	4.1	4.7	5.1	.0128	.0112
PE	3-004L	Zed	Ni					5.6	5.5	6.7	4.1	.0330	.0380
								9.6	6.4				
PE	3-004S	Zed	Ni					5.3	5.7	5.5	6.6	.0150	.0180
PE	IR&D1L	NiBE	Ni	10.9	16.7	8.5	17.3	3.8	3.7	4.4	2.3	.0694	.0781
				7.8				5.1	3.6				
PE	IR&D1S	NiBE	Ni	23.7	17.5	27.3	19.3	7.3	2.5	1.8	2.1	.0667	.0562
				24.6	20.4	23.2							
PE	IR&D2L	NiBE	Pt	5.7	7.6	8.5		2.3	2.5	2.3	3.4	.0526	.0588
								2.9	2.3				
PE	IR&D2S	NiBE	Pt	11.8	7.4	11.2		4.6	4.0	2.8	2.7	.0549	.0385
PE	SAO-1L	NiBE	Ni					3.0	3.4	3.0	2.6	.0909	.1064
								3.5	3.4				
PE	SAO-1S	NiBE	Ni					1.8	2.0	2.4	2.1	.0641	.0757
PE	SAO-2L	NiBE	Pt	11.6	12.1	10.9		1.7	2.4	2.3	2.8	.0526	.0641
								1.8	2.5				
PE	SAO-2S	NiBE	Pt	10.5	8.0	11.1		1.7	2.0	2.0	2.1	.0476	.0354
MP	RC2a/R2L	Zed	Au	5.4	2.7	3.1	3.2	3.7	5.9	4.4	5.5	.0284	.0305
				3.6				5.2	5.4				
MP	RC2b/R2S	Zed	Au	4.2	5.7	4.3	4.7	5.4	6.8	4.6	7.0	.0195	.0195
EK	RCII-1L	ULE	Au	12.3	15.0	10.1	10.3	6.1	5.2	27.8	15.6	.0735	.0877
				11.9				13.0	13.1				
EK	RCII-1S	ULE	Au					1.7	2.0	3.6	2.3	.0961	.1020
EK	RCII-2L	ULE	Au	4.8	4.9	4.2	4.2	1.8	2.7	3.9	5.7	.0658	.0752
				4.5									
EK	RCII-2S	ULE	Au					2.3	2.4				
ITEK	1L	FS	Ni					2.0	4.8	2.9	2.8	.0694	.0649
								4.0	4.7	5.0	4.3	.0510	.0540
ITEK	1S	FS	Ni					4.8	4.3				
ITEK	2L	FS	Pt					4.0	4.4	3.8	4.3	.0480	.0510
								2.4	3.3	2.6	2.7	.0420	.0450
ITEK	2S	FS	Pt					2.7	2.9				
ITEK	3L	Zed	Ni					4.6	3.6	4.6	3.4	.0400	.0440
								5.2	4.8	3.8	3.8	.0510	.0590
ITEK	3S	Zed	Ni					3.7	3.9				
								3.8	3.9	4.7	4.2	.0260	.0280

TABLE 14. SAME AS TABLE 13, BUT THE FLATS ARE SORTED BY THE MANUFACTURER

COMPANY	SAMPLE I.D.	SUBS	COAT	LLL PROFILOMETER ANGSTROMS RMS	LLL PROFILOMETER ANGSTROMS STAN DEV.	MSFC BRDF ANGSTROMS RMS	MSFC BRDF ANGSTROMS STAN DEV.	TUYMAN GREEN WAVES RMS
EK	I-1L	FS	Ni	4.0	.83	7.2	4.55	.0514
EK	I-1S	FS	Ni	3.2	1.05	4.9	2.61	.0187
EK	I-2L	FS	Pt	5.8	1.14	5.4	2.06	.0407
EK	I-2S	FS	Pt	5.1	1.02	7.6	4.81	.0315
EK	I-3L	FS	Au	6.4	.77	6.5	5.00	.0495
EK	I-3S	FS	Au	6.6	1.38	5.4	1.38	.0414
EK	II-1L	ULE	Au					
EK	II-1S	ULE	Au	5.9	.95	3.6	1.00	.1032
EK	II-2L	ULE	Pt					
EK	II-2S	ULE	Pt	6.3	1.30			
EK	II-3L	ULE	Ni			23.2	12.98	.0626
EK	II-3S	ULE	Ni	4.4	1.10	3.6	1.17	.0828
EK	III-1L	Zed	Ni	11.5	2.20	2.2	.25	.0644
EK	III-1S	Zed	Ni	6.1	1.01	1.9	.18	.0348
EK	III-2L	Zed	Pt	11.3	1.45	16.6	4.34	.0578
EK	III-2S	Zed	Pt	27.2	4.56	15.0	9.50	.0403
EK	IV-1L	Cer	Ni	5.4	.43	2.1	.39	.1011
EK	IV-1S	Cer	Ni	7.5	2.45	3.9	.75	.0610
EK	IV-2L	Cer	Pt			5.1	2.68	.0715
EK	IV-2S	Cer	Pt			6.6	2.03	.0445
EK	V-1L	FQ	Ni			5.4	3.29	.0448
EK	V-1S	FQ	Ni	3.0	.67	2.2	.24	.0424
EK	V-2L	FQ	Pt			8.6	4.24	.0335
EK	V-2S	FQ	Pt			5.2	.88	.0405
EK	VI-3L	FS	Ni	8.1	1.06	6.8	.83	.0450
EK	VI-3S	FS	Ni	8.5	1.71	7.4	.17	.0309
EK	RCII-1L	ULE	Au	11.9	1.97	13.5	8.16	.0806
EK	RCII-1S	ULE	Au			2.4	.84	.0990
EK	RCII-2L	ULE	Au	4.5	.33	3.1	1.44	.0705
EK	RCII-2S	ULE	Au			3.1	1.19	.0671
MP	1a/R1L	Zed	Ni	8.1	8.21	10.5	2.64	.0179
MP	1b/R1S	Zed	Ni	3.9	1.21	11.9	4.15	.0153
MP	2a/R2L	Zed	Pt	74.8	88.18	9.9	.00	.0271
MP	2b/R2S	Zed	Pt			19.0	.00	.0216
MP	3a/R1L	Zed	Au	36.1	19.66	19.0	3.36	.0232
MP	3b/R1S	Zed	Au	48.9	53.53	33.3	1.18	.0148
MP	RC2a/R2L	Zed	Au	3.6	1.06	5.0	.81	.0294
MP	RC2b/R2S	Zed	Au	4.7	.68	5.9	1.15	.0195
PE	1-001L	FS	Pt			21.6	12.60	.0300
PE	1-004S	FS	Ni			9.0	1.65	.0275
PE	1-002L	FS	Ni	2.8	.59	2.3	.38	.0438
PE	1-002S	FS	Ni	3.3	.97	1.7	.12	.0255
PE	1-004L	FS	Au			7.5	1.87	.0310
PE	1-003S	FS	Au			11.7	2.05	.0275
PE	2-001L	ULE	Au					
PE	2-001S	ULE	Au					
PE	2-003L	ULE	Ni	3.5	50	2.3	.77	.0368
PE	2-003S	ULE	Ni	4.1	.06	2.3	.60	.0233
PE	2-004L	ULE	Pt	3.6	.40	3.1	.49	.0298
PE	2-004S	ULE	Pt	4.0	.68	6.3	2.41	.0232
PE	3-001L	Zed	Pt	3.4	.50	8.1	10.23	.0359
PE	3-001S	Zed	Pt	3.4	.15	4.5	1.21	.0202
PE	3-003L	Zed	Au	8.3	3.17	7.8	4.74	.0394
PE	3-003S	Zed	Au	3.7	1.53	4.6	.41	.0120
PE	3-004L	Zed	Ni			6.3	1.85	.0355
PE	3-004S	Zed	Ni			5.8	.57	.0165
PE	IR&D1L	NiBE	Ni	12.2	4.50	3.8	.93	.0737
PE	IR&D1S	NiBE	Ni	22.3	3.38	3.4	2.60	.0614
PE	IR&D2L	NiBE	Pt	7.3	1.43	2.6	.45	.0557
PE	IR&D2S	NiBE	Pt	10.1	2.39	3.5	.93	.0467
PE	SAO-1L	NiBE	Ni			3.1	.34	.0986
PE	SAO-1S	NiBE	Ni			2.1	.25	.0699
PE	SAO-2L	NiBE	Pt	11.5	.60	2.2	.42	.0583
PE	SAO-2S	NiBE	Pt	9.9	1.64	1.9	.17	.0415
ITEK	1L	FS	Ni			4.5	.38	.0525
ITEK	1S	FS	Ni			4.1	.28	.0495
ITEK	2L	FS	Pt			2.8	.31	.0435
ITEK	2S	FS	Pt			4.0	.64	.0420
ITEK	3L	Zed	Ni			4.2	.64	.0550
ITEK	3S	Zed	Ni			4.1	.40	.0270

TABLE 15. SAME AS TABLE 14, BUT THE FLATS ARE SORTED BY THE SUBSTRATE MATERIAL

COMPANY	SAMPLE I.D.	SUBS	COAT	LLL PROFILOMETER ANGSTROMS		MSFC BRDF ANGSTROMS		TWYMAN GREEN WAVES
				RMS	STAN DEV.	RMS	STAN DEV.	RMS
EK	I-1L	FS	Ni	4.0	.83	7.2	4.55	.0514
EK	I-1S	FS	Ni	3.2	1.05	4.9	2.61	.0187
EK	I-2L	FS	Pt	5.8	1.14	5.4	2.06	.0407
EK	I-2S	FS	Pt	5.1	1.02	7.6	4.81	.0315
EK	I-3L	FS	Au	6.4	.77	6.5	5.00	.0495
EK	I-3S	FS	Au	6.6	1.38	5.4	1.38	.0414
EK	VI-3L	FS	Ni	8.1	1.06	6.8	.83	.0450
EK	VI-3S	FS	Ni	8.5	1.71	7.4	.17	.0309
PE	1-001L	FS	Pt			21.6	12.60	.0300
PE	1-004S	FS	Ni			9.0	1.65	.0275
PE	1-002L	FS	Ni	2.8	.59	2.3	.38	.0438
PE	1-002S	FS	Ni	3.3	.97	1.7	.12	.0255
PE	1-004L	FS	Au			7.5	1.87	.0310
PE	1-003S	FS	Au			11.7	2.05	.0275
ITEK	1L	FS	Ni			4.5	.38	.0525
ITEK	1S	FS	Ni			4.1	.28	.0495
ITEK	2L	FS	Pt			2.8	.31	.0435
ITEK	2S	FS	Pt			4.0	.64	.0420
EK	II-1L	ULE	Au					
EK	II-1S	ULE	Au	5.9	.95	3.6	1.00	.1032
EK	II-2L	ULE	Pt					
EK	II-2S	ULE	Pt	6.3	1.30			
EK	II-3L	ULE	Ni			23.2	12.98	.0626
EK	II-3S	ULE	Ni	4.4	1.10	3.6	1.17	.0828
PE	2-001L	ULE	Au					
PE	2-001S	ULE	Au					
PE	2-003L	ULE	Ni	3.5	.50	2.3	.77	.0368
PE	2-003S	ULE	Ni	4.1	.06	2.3	.60	.0233
PE	2-004L	ULE	Pt	3.6	.40	3.1	.49	.0298
PE	2-004S	ULE	Pt	4.0	.68	6.3	2.41	.0232
EK	RCII-1L	ULE	Au	11.9	1.97	13.5	8.16	.0806
EK	RCII-1S	ULE	Au			2.4	.84	.0990
EK	RCII-2L	ULE	Au	4.5	.33	3.1	1.44	.0705
EK	RCII-2S	ULE	Au			3.1	1.19	.0671
EK	III-1L	Zed	Ni	11.5	2.20	2.2	.25	.0644
EK	III-1S	Zed	Ni	6.1	1.01	1.9	.18	.0348
EK	III-2L	Zed	Pt	11.3	1.45	16.6	4.34	.0578
EK	III-2S	Zed	Pt	27.2	4.56	15.0	9.50	.0403
MP	1a/R1L	Zed	Ni	8.1	8.21	10.5	2.64	.0179
MP	1b/R1S	Zed	Ni	3.9	1.21	11.9	4.15	.0153
MP	2a/R2L	Zed	Pt	74.8	88.18	9.9	.00	.0271
MP	2b/R2S	Zed	Pt			19.0	.00	.0216
MP	3a/R1L	Zed	Au	36.1	19.66	19.0	3.36	.0232
MP	3b/R1S	Zed	Au	48.9	53.53	33.3	1.18	.0148
PE	3-001L	Zed	Pt	3.4	.50	8.1	10.23	.0359
PE	3-001S	Zed	Pt	3.4	.15	4.5	1.21	.0202
PE	3-003L	Zed	Au	8.3	3.17	7.8	4.74	.0394
PE	3-003S	Zed	Au	3.7	1.53	4.6	.41	.0120
PE	3-004L	Zed	Ni			6.3	1.85	.0355
PE	3-004S	Zed	Ni			5.8	.57	.0165
MP	RC2a/R2L	Zed	Au	3.6	1.06	5.0	.81	.0294
MP	RC2b/R2S	Zed	Au	4.7	.68	5.9	1.15	.0195
ITEK	3L	Zed	Ni			4.2	.64	.0550
ITEK	3S	Zed	Ni			4.1	.40	.0270
EK	IV-1L	Cer	Ni	5.4	.43	2.1	.39	.1011
EK	IV-1S	Cer	Ni	7.5	2.45	3.9	.75	.0610
EK	IV-2L	Cer	Pt			5.1	2.68	.0715
EK	IV-2S	Cer	Pt			6.6	2.03	.0445
EK	V-1L	FQ	Ni			5.4	3.29	.0448
EK	V-1S	FQ	Ni	3.0	.67	2.2	.24	.0424
EK	V-2L	FQ	Pt			8.6	4.24	.0335
EK	V-2S	FQ	Pt			5.2	.88	.0405
PE	IR&D1L	NiBE	Ni	12.2	4.50	3.8	.93	.0737
PE	IR&D1S	NiBE	Ni	22.3	3.38	3.4	2.60	.0614
PE	IR&D2L	NiBE	Pt	7.3	1.43	2.6	.45	.0557
PE	IR&D2S	NiBE	Pt	10.1	2.39	3.5	.93	.0467
PE	SAO-1L	NiBE	Ni			3.1	.34	.0986
PE	SAO-1S	NiBE	Ni			2.1	.25	.0699
PE	SAO-2L	NiBE	Pt	11.5	.60	2.2	.42	.0583
PE	SAO-2S	NiBE	Pt	9.9	1.64	1.9	.17	.0415

TABLE 16. SAME AS TABLE 14, BUT THE FLATS ARE SORTED BY THE COATING MATERIAL

COMPANY	SAMPLE I.D.	SUBS	COAT	LLL PROFILOMETER ANGSTROMS RMS	LLL PROFILOMETER ANGSTROMS STAN DEV.	MSFC BRDF ANGSTROMS RMS	MSFC BRDF ANGSTROMS STAN DEV.	TWYMAN GREEN WAVES RMS
EK	I-1L	FS	Ni	4.0	.83	7.2	4.55	.0514
EK	I-1S	FS	Ni	3.2	1.05	4.9	2.61	.0187
EK	II-3L	ULE	Ni			23.2	12.98	.0626
EK	II-3S	ULE	Ni	4.4	1.10	3.6	1.17	.0828
EK	III-1L	Zed	Ni	11.5	2.20	2.2	.25	.0644
EK	III-1S	Zed	Ni	6.1	1.01	1.9	.18	.0348
EK	IV-1L	Cer	Ni	5.4	.43	2.1	.39	.1011
EK	IV-1S	Cer	Ni	7.5	2.45	3.9	.75	.0610
EK	V-1L	FQ	Ni			5.4	3.29	.0448
EK	V-1S	FQ	Ni	3.0	.67	2.2	.24	.0424
EK	VI-3L	FS	Ni	8.1	1.06	6.8	.83	.0450
EK	VI-3S	FS	Ni	8.5	1.71	7.4	.17	.0309
MP	1a/R1L	Zed	Ni	8.1	8.21	10.5	2.64	.0179
MP	1b/R1S	Zed	Ni	3.9	1.21	11.9	4.15	.0153
PE	1-004S	FS	Ni			9.0	1.65	.0275
PE	1-002L	FS	Ni	2.8	.59	2.3	.38	.0438
PE	1-002S	FS	Ni	3.3	.97	1.7	.12	.0255
PE	2-003L	ULE	Ni	3.5	.50	2.3	.77	.0368
PE	2-003S	ULE	Ni	4.1	.06	2.3	.60	.0233
PE	3-004L	Zed	Ni			6.3	1.85	.0355
PE	3-004S	Zed	Ni			5.8	.57	.0165
PE	IR&D1L	NiBE	Ni	12.2	4.50	3.8	.93	.0737
PE	IR&D1S	NiBE	Ni	22.3	3.38	3.4	2.60	.0614
PE	SAO-1L	NiBE	Ni			3.1	.34	.0986
PE	SAO-1S	NiBE	Ni			2.1	.25	.0699
ITEK	1L	FS	Ni			4.5	.38	.0525
ITEK	1S	FS	Ni			4.1	.28	.0495
ITEK	3L	Zed	Ni			4.2	.64	.0550
ITEK	3S	Zed	Ni			4.1	.40	.0270
EK	I-2L	FS	Pt	5.8	1.14	5.4	2.06	.0407
EK	I-2S	FS	Pt	5.1	1.02	7.6	4.81	.0315
EK	II-2L	ULE	Pt					
EK	II-2S	ULE	Pt	6.3	1.30			
EK	III-2L	Zed	Pt	11.3	1.45	16.6	4.34	.0578
EK	III-2S	Zed	Pt	27.2	4.56	15.0	9.50	.0403
EK	IV-2L	Cer	Pt			5.1	2.68	.0715
EK	IV-2S	Cer	Pt			6.6	2.03	.0445
EK	V-2L	FQ	Pt			8.6	4.24	.0335
EK	V-2S	FQ	Pt			5.2	.88	.0405
MP	2a/R2L	Zed	Pt	74.8	88.18	9.9	.00	.0271
MP	2b/R2S	Zed	Pt			19.0	.00	.0216
PE	1-001L	FS	Pt			21.6	12.60	.0300
PE	2-004L	ULE	Pt	3.6	.40	3.1	.49	.0298
PE	2-004S	ULE	Pt	4.0	.68	6.3	2.41	.0232
PE	3-001L	Zed	Pt	3.4	.50	8.1	10.23	.0359
PE	3-001S	Zed	Pt	3.4	.15	4.5	1.21	.0202
PE	IR&D2L	NiBE	Pt	7.3	1.43	2.6	.45	.0557
PE	IR&D2S	NiBE	Pt	10.1	2.39	3.5	.93	.0467
PE	SAO-2L	NiBE	Pt	11.5	.60	2.2	.42	.0583
PE	SAO-2S	NiBE	Pt	9.9	1.64	1.9	.17	.0415
ITEK	2L	FS	Pt			2.8	.31	.0435
ITEK	2S	FS	Pt			4.0	.64	.0420
EK	I-3L	FS	Au	6.4	.77	6.5	5.00	.0495
EK	I-3S	FS	Au	6.6	1.38	5.4	1.38	.0414
EK	II-1L	ULE	Au					
EK	II-1S	ULE	Au	5.9	.95	3.6	1.00	.1032
MP	3a/R1L	Zed	Au	36.1	19.66	19.0	3.36	.0232
MP	3b/R1S	Zed	Au	48.9	53.53	33.3	1.18	.0148
PE	1-004L	FS	Au			7.5	1.87	.0310
PE	1-003S	FS	Au			11.7	2.05	.0275
PE	2-001L	ULE	Au					
PE	2-001S	ULE	Au					
PE	3-003L	Zed	Au	8.3	3.17	7.8	4.74	.0394
PE	3-003S	Zed	Au	3.7	1.53	4.6	.41	.0120
MP	RC2a/R2L	Zed	Au	3.6	1.06	5.0	.81	.0294
MP	RC2b/R2S	Zed	Au	4.7	.68	5.9	1.15	.0195
EK	RCII-1L	ULE	Au	11.9	1.97	13.5	8.16	.0806
EK	RCII-1S	ULE	Au			2.4	.84	.0990
EK	RCII-2L	ULE	Au	4.5	.33	3.1	1.44	.0705
EK	RCII-2S	ULE	Au			3.1	1.19	.0671

TABLE 17. RESULTS OF FECO[a] AND TIS[b] MEASUREMENTS OF THE RMS SURFACE ROUGHNESS (Å)

Manufacturer	Substrate	Coating	FECO		TIS	
			Long Mirror	Short Mirror	Long	Short
Eastman Kodak	Fused Silica	Ni	8.2	7.9	7.2	4.9[c]
Eastman Kodak	Fused Silica	Pt			5.5	7.6[c]
Eastman Kodak	Fused Silica	Au			6.5	5.4[c]
Eastman Kodak	ULE	Au				3.6[c]
Eastman Kodak	ULE	Ni	6.4	15.2	23.2	3.5[c]
Eastman Kodak	Zerodur	Ni	9.3	10.0	2.2	1.9[c]
Eastman Kodak	Zerodur	Pt			16.6	15.0[c]
Eastman Kodak	Cervit	Ni	9.4	12.3	2.1	4.0[c]
Eastman Kodak	Fused Quartz	Ni	8.0	10.1	5.4	2.1[c]
Perkin Elmer	Fused Silica	Pt			3.9	5.8
Perkin Elmer	Fused Silica	Ni			4.3	5.8
Perkin Elmer	Fused Silica	Au			7.7	9.7
Perkin Elmer	ULE	Au			11.2	21.5
Perkin Elmer	ULE	Ni			2.7	4.2
Perkin Elmer	ULE	Pt			3.3	4.6
Perkin Elmer	Zerodur	Pt			4.7	4.4
Perkin Elmer	Zerodur	Au			8.7	6.2
Perkin Elmer	Zerodur	Ni			3.9	5.9
Perkin Elmer	Ni-Be	Ni			4.4	5.4
Perkin Elmer	Ni-Be	Pt			4.0	4.7
Perkin Elmer (SAO)	Ni-Be	Ni	3.2	2.1	3.9	3.6
Perkin Elmer (SAO)	Ni-Be	Pt	2.3	2.0	4.3	3.9

a. FECO measurements were made by the vendors.
b. Recorded values are those measured at NWC of China Lake, California.
c. Recorded TIS values are from the MSFC scatterometer measurements.

TABLE 18. RMS SURFACE ROUGHNESS (Å) VIA TALYSTEP

Manufacturer	Substrate	Coating	NBS		NWC
			Short Trace	Long Trace	
Eastman Kodak (Short)	Zerodur	Pt	4.3 ± 0.6	18.0 ± 4.0	
Eastman Kodak (Long)	Zerodur	Pt	4.9 ± 0.9	9.5 ± 2.0	
Eastman Kodak (Short)	Fused Silica	Au	8.0 ± 4.0	9.9 ± 1.5	
Eastman Kodak (Long)	Fused Silica	Au	11.5 ± 2.9	7.0 ± 3.0	
Eastman Kodak (Short)	ULE	Pt	6.0 ± 3.0	7.8 ± 1.5	
Eastman Kodak (Long)	ULE	Pt	4.6 ± 0.7	8.0 ± 4.0	
Perkin Elmer (Long)	Zerodur	Ni	3.1	2.9	3.6
Perkin Elmer (Short)	Ni-Be	Ni			11.6
Perkin Elmer (Long)	Ni-Be	Pt			8.2
Perkin Elmer (Short) (SAO)	Ni-Be	Ni			12.7
Perkin Elmer (Short) (SAO)	Ni-Be	Pt			9.3
Perkin Elmer (Long)	Fused Silica	Pt	10.9	29.9	3.7
Perkin Elmer (Long)	Fused Silica	Ni			4.0
Perkin Elmer (Long)	Fused Silica	Au	1.6	2.3	3.7
Perkin Elmer (Long)	ULE	Ni			3.4
Perkin Elmer (Long)	ULE	Pt			3.8
Perkin Elmer (Short)	Zerodur	Pt			3.3
Perkin Elmer (Short)	Zerodur	Au			4.2

TABLE 19. COMPARISON OF THE MEASURED FLATNESS VALUES USING THE FIZEAU AND THE TWYMAN-GREEN INTERFEROMETERS (RMS VALUES, 6328 Å)

Manufacturer	Substrate	Coating	Twyman Green	Fizeau
Perkin Elmer (Long)	Fused Silica	Pt	0.030	0.045
Perkin Elmer (Short)	Fused Silica	Pt	0.028	0.041
Perkin Elmer (Long)	Fused Silica	Ni	0.044	0.062
Perkin Elmer (Short)	Fused Silica	Ni	0.026	0.024
Perkin Elmer (Long)	Fused Silica	Au	0.031	0.043
Perkin Elmer (Short)	Fused Silica	Au	0.028	0.035

TABLE 20. POLISHING TECHNIQUES FOR THE AXAF FLATS

Manufacturer	Flat Description	Polishing Techniques
Eastman Kodak	All	98-in. precision plano polisher, Tambrite "C" (cerium oxide)
Perkin Elmer	All except Be-Ni Substrates	Bowl-feed polishing (ZOX-CE89)
	Be-Ni Substrates	Chemical/mechanical polishing (Spectralite 2-400)
Itek	All	Bowl-feed polishing

VIII. SUMMARY AND CONCLUSIONS

This document was meant to describe the experimental techniques and measurement results of the optical and X-ray performance of various "state-of-the-art" polished mirror flats. No attempt was made in this report to correlate the non-X-ray techniques measurements to the X-ray scattering performance because the X-ray scattering data showed that the mirrors were "too smooth" to exhibit enough scattering effects to analyze. However, the large scatter in the values of a particular non-X-ray technique for the various flats indicate that there is no one optical technique available which will unambiguously indicate a high quality X-ray reflecting surface. It is hoped that the results reported here could be used to determine a particular combination of optical and/or mechanical techniques which will determine the X-ray performance. This is an ongoing study of our program.

Nevertheless, the basic conclusion that has been reached from this phase of the research program is that the present state-of-the-art of polishing techniques is more than adequate for the specifications of the AXAF mirrors.

REFERENCES

1. Church, E. L.: Proc. SPIE, Vol. 257, 1980, p. 254.

2. Silk, J. K.: Proc. SPIE, Vol. 257, 1980, p. 248.

3. Church, E. L., Jenkinson, H. A., and Zavoda, J. M.: Opt. Eng., Vol. 18 (2), 1979, p. 125.

4. Church, E. L.: Proc. SPIE, Vol. 184, 1979, p. 196.

5. Tolansky, S.: Multiple-Beam Interferometry of Surfaces and Films. Clarendon Press, Oxford, 1948.

6. Hodgkinson, I. J.: J. Phys. E., Vol. 3, 1970, p. 300.

7. Zombeck, M. V., Wyman, C. C., and Weisskopf, M. C.: Opt. Eng., Vol. 21 (1), 1982, p. 63.

8. Williams, A. C. and Reily, J. C.: To be published in Opt. Eng.

9. Zombeck, M. V., Braeuninger, H., Ondrusch, A., and Predehl, P.: Proc. SPIE, Vol. 316, 1982, p. 174.

10. Griner, D. B.: Proc. SPIE, Vol. 257, 1980, p. 217.

11. Sommargren, G. E.: Applied Optics, 1980.

12. Bennett, J. M.: Applied Optics, Vol. 15, 1976, p. 2705.

13. Elson, J. M. and Bennett, J. M.: J. Opt. Soc. Am., Vol. 69, 1979, p. 31.

14. Vorburger, T. V., Teague, E. C., and Scire, F. E.: Dimensions/NBS, November 1978.

15. AXAF Test Flat Measurements with the HRI. SOA-AXAF-82-012, September 1982.

16. AXAF X-Ray Scattering Measurements at the Max Planck Institute for Extra-terrestrial Physics. SAO-AXAF-82-010, September 1982.

17. Stylus Measurements of AXAF Test Flats. SAO-AXAF-82-011, September 1982.

18. Rehn, V., Jones, V. O., Elson, J. M., and Bennett, J. M.: Nucl. Instru. and Meth., Vol. 172, 1980, pp. 307-314.

APPROVAL

THE AXAF TECHNOLOGY PROGRAM: THE OPTICAL FLATS TESTS

By A. C. Williams, J. D. Harper, J. C. Reily, M. C. Weisskopf, C. L. Wyman, and M. Zombeck

The information in this report has been reviewed for technical content. Review of any information concerning Department of Defense or nuclear energy activities or programs has been made by the MSFC Security Classification Officer. This report, in its entirety, has been determined to be unclassified.

A. J. DESSLER
Director, Space Science Laboratory

☆U S GOVERNMENT PRINTING OFFICE 1984—746-070/151